Techno-economic Assessment and Optimisation of a Carnot Battery Application in a Concentrating Solar Power Plant

by

Louw Gysbert Redelinghuys

Thesis presented in partial fulfilment of the requirements for
the degree of Master of Engineering (Mechanical) in the
Faculty of Engineering at Stellenbosch University

Supervisor: Prof. C. McGregor

April 2022

Declaration

By submitting this thesis electronically, I declare that the entirety of the work contained therein is my own, original work, that I am the sole author thereof (save to the extent explicitly otherwise stated), that reproduction and publication thereof by Stellenbosch University will not infringe any third party rights and that I have not previously in its entirety or in part submitted it for obtaining any qualification.

Date: ....April 2022.......

Abstract

Techno-economic Assessment and Optimisation of a Carnot Battery Application in a Concentrating Solar Power Plant

Louw Gysbert Redelinghuys
Department of Mechanical and Mechatronic Engineering,
University of Stellenbosch,
Private Bag X1, Matieland 7602, South Africa.

Thesis: MEng (Mech)
April 2022

The techno-economic assessment as well as optimisation of a Carnot battery application in a parabolic trough concentrating solar power (CSP) plant is conducted. A computational techno-economic model of the Carnot battery is developed and verified with reasonable accuracy. The model entails electric resistive heating integrated with the thermal energy storage of the CSP plant. During solar thermal charge cycles, potentially abundant solar photovoltaic grid electricity is stored as thermal energy. Stored energy is discharged during periods of lower solar thermal supply to promote baseload power generation.

A fundamental techno-economic understanding of the CSP Carnot battery is developed. Charging costs, together with low round-trip efficiencies, can inhibit the system's economic viability. Nonetheless, the CSP plant displays increased potential for baseload power generation once retrofitted. This enhances its continuity of inertial support and reduces intermittent power generation. The standard solar-thermal charge-discharge cycles are inherently suited for ideal time-shifting of surplus electricity, more so during summer than winter.

Multi-objective optimisation determines the optimum thermal energy storage capacity for heater integration. The mathematical significance of optimisation results is explored via Pareto fronts and energy-cost curves. In general, the storage capacity is inversely related to the installed heater capacity at which the latter overcharges energy. At this point, electrical energy is stored at the expense of underutilised solar thermal energy. Plants with larger solar fields are more prone to overcharge, yielding less capacity for optimally allocated heaters. This could present a barrier to technical synergy.

Uittreksel

Tegno-ekonomiese Assessering en Optimisering van 'n Carnot-battery Toepassing in 'n Gekonsentreerde Sonkragaanleg

("Techno-economic Assessment and Optimisation of a Carnot Battery Application in a Concentrating Solar Power Plant")

Louw Gysbert Redelinghuys
Departement Meganiese en Megatroniese Ingenieurswese,
Universiteit van Stellenbosch,
Privaatsak X1, Matieland 7602, Suid Afrika.

Tesis: MIng (Meg)
April 2022

Die tegno-ekonomiese assessering sowel as optimisering van 'n Carnot-battery toepassing in 'n paraboliese trog gekonsentreerde sonkragaanleg (GSK) word uitgevoer. 'n Tegno-ekonomiese berekeningsmodel van die Carnot-battery word ontwikkel en as redelik akkuraat bevestig. Die model behels elektriese weerstandsverhitters wat met die aanleg se termiese energie-opbergingseenheid geïntegreer word. Vanuit die kragnetwerk word moontlike oortollige fotovoltaïese elektrisiteit tydens sontermiese laaisiklusse as termiese energie gestoor. Hierdie energie word tydens periodes van sontermiese onderverskaffing ontlaai, met die doel om basislading elektrisiteit op te wek.

'n Fundamentele tegno-ekonomiese begrip van die GSK Carnot-battery word ontwikkel. Laaikostes en lae omskakelingsdoeltreffendheid kan ekonomiese lewensvatbaarheid inhibeer. As 'n Carnot-battery toon die GSK-aanleg nietemin meer potensiaal vir basislading elektrisiteitsopwekking. Dit bevorder die kontinuïteit van traagheidsondersteuning en verminder afwisselende kragopwekking. Die standaard sontermiese laai-ontlaai siklusse is inherent gepas vir ideale tydverskuiwing van oortollige energie, veral meer tydens somer as winter.

Meerdoelige optimisering word benut om die optimale termiese energie stoorkapasiteit vir verhitter toevoeging te bepaal. Die wiskundige betekenis van optimiseringsresultate word deur middel van Pareto-fronte en energie-koste kurwes verken. In die algemeen is die stoorkapasiteit omgekeerd eweredig aan die verhitterkapasiteit waarby laasgenoemde energie oorlaai. Hier word elektriese energie ten koste van onderbenutte sontermiese energie gestoor. Aanlegte met groter sonvelde is meer vatbaar vir oorlading en bevat minder kapasiteit vir optimale verhitter integrasie. Hierdie eienskap kan tegniese sinergie bemoeilik.

Acknowledgements

I thank my supervisor, Prof McGregor, for accepting me as a Masters student of his. Prof, thank you for this interesting topic and guiding me in researching it. I am grateful for your support and the opportunities that came along my way as a result thereof. Reflecting on the past two years, I can truly say that I have progressed personally and professionally in more ways than one. I acknowledge you for having played a substantial role in that growth.

I am extremely fortunate to be a Skye Foundation scholarship holder.[†] Thank you to the Foundation for investing in postgraduate students based on merit; I am humbled to be a recipient. Many thanks to the Deputy Chairman, Dr Passmore, who oversaw my candidature. It has been a pleasure meeting you for coffee in Swellendam.

I am indebted to individuals at the Department of Mechanical and Mechatronic Engineering who nominated and supported me for the Skye Foundation scholarship. They are: Ms Liebenberg, Prof McGregor, Prof Van Niekerk and Prof Schreve.

I wish to thank Ms Liebenberg and Ms Barendse for their postgraduate administrative assistance which they provided.

Thank you to the Solar Thermal Energy Research Group (STERG) and its members for supporting me and my research. I am appreciative of the funds provided to attend the 2020 SolarPACES conference. I am also thankful for having served with the STERG Operations Committee.

Ms Rudolph and Mr Vacu at the Writing Lab have provided excellent consultation in the writing of this thesis. I thank them for honing my writing proficiency.

I acknowledge the assistance of Mr Magoro and Mr Buckley, at the Centre for Renewable and Sustainable Energy Studies, in obtaining meteorological data for this research.

The National Renewable Energy Laboratory (NREL) is acknowledged for utilising their System Advisor Model (SAM) in this research.

[†] Any views expressed, statements made, or conclusions drawn are those of the author and not of the Skye Foundation.

I thank Mr Vaidya from EXHEAT for assisting me in obtaining information on the electric heaters.

I thank Dr Clark who assisted me in obtaining the generation data from Eskom.

I appreciate the examiners of this thesis for taking the time to provide constructive and useful feedback towards a better thesis.

Thank you to friends and peers from Stellenbosch University for supporting me. I am truly thankful for the assistance I received with proofreading, literature, data acquisition and backup, Python, MS Excel, SAM and LaTeX, among other areas, from: John van Tonder, Danial Waters, Taskeen Ebrahim, Anri le Roux, Afroz Khan, Nick Tutt, Jessika Brtan, Kyran Davids, Kazia Luterek, Robin Roux, André de Klerk and Jacomien Pienaar. I also acknowledge the direct assistance received from family members: J.C., L.J.M and N.L. Redelinghuys, M.E. and S.J. van Blerk.

Lastly, I thank my parents for their love and unmatched support. You have made the past two years memorable. I am privileged to reach this milestone with both of you at my side.

Their cheers of encouragement
resonate
fervently beside the track
echo
long after the race is completed.

Dedications

Hierdie tesis word met liefde aan my ouers opgedra
Baie dankie vir alles

Contents

List of Figures

List of Tables

Nomenclature

Abbreviations

ACC	Air-cooled condenser
AEP	Annual electricity production
Ave.	Average
CAISO	California Independent System Operator
CF	Capacity factor
CFF	Construction financing factor
CRF	Capital recovery factor
CSP	Concentrating solar power
CV	Control volume
DCC	Direct capital cost
Diff.	Difference
DM	Diversity metric
DNI	Direct normal irradiation
EOL	End-of-life
EPC	Engineer-procure-construct
Err.	Error
FCR	Fixed charge rate
FOC	Fixed operating cost
G	Generator

GBP	British Pound
HP	High pressure
HSF	Heat storage fluid
HTF	Heat transfer fluid
HX	Heat exchanger
Incr.	Increase(d)
IP	Intermediate pressure
IRR	Internal rate of return
ITD	Initial temperature difference
LCOE	Levelised cost of electricity
LCOS	Levelised cost of storage
LP	Low pressure
LPOE	Levelised profit of electricity
MOO	Multi-objective optimisation
NREL	National Renewable Energy Laboratory
OFWH	Open feedwater heater
O&M	Operational and maintenance
PC	Power cycle
Perf.	Performance
PFF	Project financing factor
PPA	Power purchase agreement
PSO	Particle swarm optimisation
PT	Parabolic trough
PV	Photovoltaic
RE	Renewable energy
REIPPPP	Renewable Energy Independent Power Producer Procurement Programme

Rel.	Relative
RoCoF	Rate of change of frequency
SA	South Africa
SAM	System Advisor Model
SCA	Solar collector assembly
SCE	Solar collector element
SM	Solar multiple
TDCC	Total direct capital cost
TES	Thermal energy storage
TIC	Total installed cost
TICC	Total indirect capital cost
TOD	Time-of-delivery
TOU	Time-of-use
UF	Utilisation factor
UFLS	Under-frequency load shedding
USA	United States of America
USD	United States Dollar
VAT	Value added tax
VOC	Variable operating cost
ZAR	South African Rand

Superscripts

T	Transpose operator
$*$	Optimum
$\prime$	Adjusted

Subscripts

a	Actual, air

abs	Absorbed
amb	Ambient
app	Approach
avail	Available
backg	Background
bd	Blowdown
c	Cold
cap	Capacity
chg	Charge
cond	Condenser
db	Dry-bulb
dchg	Discharge
des	Design
disc	Discard(ed)
e	Electrical
esc	Escalation
f	Field, saturated liquid
fg	Vaporisation
g	Saturated vapor
H	High, heater
h	Hot
i	In(let)
infl	Inflation
L	Low
LB	Lower bound
l	Lifetime
loss	Loss(es)

m	Mean
max	Maximum
min	Minimum
N	Nadir
n	Heater counter
nom	Nominal
o	Out(let)
p	Pump
red	Reduced
recirc	Recirculate
refl	Reflective
rej	Reject
round	Round-trip
s	Isentropic
sat	Saturation
set	Set-point
su	Startup
t	Turbine
th	Thermal
tot	Total
U	Utopian
UB	Upper bound
W	Worst
w	Working fluid

Symbols

A	Area

a	Equality constraint counter $\in [1, m]$
b	Cognitive and social index $\in [1, 2]$
C	Cost
c	Specific heat
c_p	Specific heat at constant pressure
c_v	Specific heat at constant volume
c_1	Cognitive scaling factor
c_2	Social scaling factor
D	Diameter
$\mathbf{D}$	Unconstrained design space
$\mathbf{DM}$	Diversity metric vector in $\mathbf{Z}$
d	Discount rate
E	Energy
$\mathbf{F}$	Vector of objective functions
f	Frequency, function, fraction, objective function
$\boldsymbol{f}$	Coordinate in $\mathbf{F}$
g	Inequality constraint, gravitational acceleration
H	Height, heater
h	Enthalpy, equality constraint
i	Year number, particle counter
j	Inequality constraint counter $\in [1, p]$
k	Number of objective functions in $\mathbf{F}$
L	Length
$\mathbf{M}$	Payoff matrix
m	Mass, number of equality constraints
$\dot{m}$	Mass flow rate
n	Number of design variables in $\mathbf{x}$

N	Number, plant lifetime
P	Pressure, Pareto frontier
$\dot{P}$	Electrical power
p	Parasitic power parameter, number of inequality constraints
$\mathbf{p}^g$	Swarm best position vector
$\mathbf{p}^i$	Particle best position vector
$\dot{Q}$	Heat transfer rate
R	Revenue, gas constant
R^2	Coefficient of determination
r	Rate
$\mathbf{r}$	Random vector
r_p	Pressure ratio
$\mathbf{S}$	Feasible design space
s	Entropy
T	Temperature
t	Time
U	Internal energy
UA	Heat loss coefficient
u	Specific internal energy
V	Volume
v	Specific volume
$\mathbf{v}$	Velocity vector
$\dot{W}$	Mechanical power
w	Specific work
x	Steam quality, independent variable
$\mathbf{x}$	Vector of design variables

y	IP steam bleeding fraction, dependent variable
$\mathbf{Z}$	Objective space
z	LP steam bleeding fraction, elevation

Greek Symbols

α	Row $\in [1, k]$ in $\mathbf{M}$
β	Column $\in [1, k]$ in $\mathbf{M}$
γ	Pseudotime increment
δ	Oversize multiplier
Δ	Change
η	Efficiency
θ	Energy of a flowing fluid per unit mass
ι	Objective function counter $\in [1, k]$
κ	Wetted loss coefficient
λ	Non-dimensional distance
$\boldsymbol{\nu}$	Stochastic velocity vector
ρ	Density
τ	Number or parallel tank pairs
ϕ	Independent uniform random scalar
ψ	Swarm size
ω	Inertia factor

Overscores

$\overline{x}$	Average of x
$\hat{x}$	Tipping point of x

Chapter 1

Introduction and Background

Sustainable electricity systems require renewable and dispatchable sources of energy (Schöniger *et al.*, 2020). The increased deployment of renewable energy (RE) stems from multiple factors. Among them are the depletion of fossil fuel reserves, the overall increase in energy demands (Moriarty and Honnery, 2016), as well as solar photovoltaic (PV) and wind-derived electricity reaching grid-parity in numerous electric markets globally (Schöniger *et al.*, 2020).

However, the major RE sources (solar PV and wind) are susceptible to natural supply fluctuations and intermittency, yielding non-dispatchable renewable electricity generation (Pearre and Swan, 2015). If any grid aims to host significant portions of renewable electricity, it is faced with the ongoing challenge of storing adequate (bulk or grid-scale) quantities of energy for when sunlight is obscured and the wind ceases to blow (Antúnez, 2015). RE integration also complicates the power supply-demand balance necessary for grid stability (Carson and Novan, 2013). The natural RE supply profiles are not guaranteed to align with the power system's demand (Schöniger *et al.*, 2020).

Historically, most grid services have been provided by conventional generators at partload, increasing or decreasing output as required by the grid (Pearre and Swan, 2015). However, energy storage is increasingly regarded as the key technology to enable RE integration (Carson and Novan, 2013; Pearre and Swan, 2015; Hartner and Permoser, 2018). Variable sources and variable loads are balanced by energy storage, without which generation must still equate with consumption. Via storage, energy is displaced through time and utilised after it is generated (Akhil *et al.*, 2015). Storage provides a service to the grid that enhances its usability, stability and reliability (Pearre and Swan, 2015).

Energy storage systems come in many shapes and sizes, each with their own intended application and characteristics. The underlying physical principles are unique and energy can be stored in largely different quantities. This thesis focuses on a subset of energy storage systems specifically intended for grid-scale storage of energy, namely Concentrating Solar Power (CSP) plants applied as Carnot batteries.

Chapter 2

Literature Study

The large-scale integration of RE is not a straightforward undertaking. The literature study introduces grid-scale challenges of RE integration considered in the thesis. It highlights the need for electric energy storage systems, provides a technical overview thereof and delimits its grid-scale service capabilities of interest. Many storage technologies exist, of which the Carnot battery is emphasised. It stores electric energy as heat and converts it back to electricity during discharge. Among the Carnot battery variants, this thesis specifically considers its application in CSP plants. The literature study concludes with the applications and competitiveness of CSP Carnot batteries in relation to battery energy storage.

2.1 Grid-scale Challenges with RE Integration

The historic power system, traditionally governed by dispatchable generators such as fossil-fueled, nuclear and pumped hydro power plants, is transitioning towards a greater share of RE generation. This transition introduces grid-scale challenges, of which intermittency and the duck curve effect are considered.

2.1.1 Intermittent Power Supply

Solar and wind energy systems are experiencing significant capacity growth (IEA, 2018). These sources are inherently intermittent and stochastic. As such, reliable power generation can become an important forecasting hurdle (Brouwer *et al.*, 2014; Notton *et al.*, 2018). The variability in output power is naturally unrelated to changes in electricity demand (Leadbetter and Swan, 2012). This is not the case in conventional coal-fired and nuclear power plants where power supply can be controlled in response to demand, an attribute termed (inherent) dispatchable generation (NEA, 2012).[1]

---

[1] Geothermal and biomass-derived power are generally considered dispatchable sources of RE (Suberu *et al.*, 2014; Lovegrove *et al.*, 2018). However, this thesis only considers the

Solar energy supply can be unpredictable with varying degrees of intermittency (Figure 2.1a), which can be seasonal, diurnal or on the meteorological temporal scale (Notton *et al.*, 2018). Figure 2.1b demonstrates the capacity factor CF, a measure of how often each technology operates at its maximum installed capacity (elaborated in Section 4.2.4.10), for various power supply sources. It is noted that intermittent RE generators display considerably lower capacity factors (IEA, 2018) than dispatchable coal and nuclear plants.

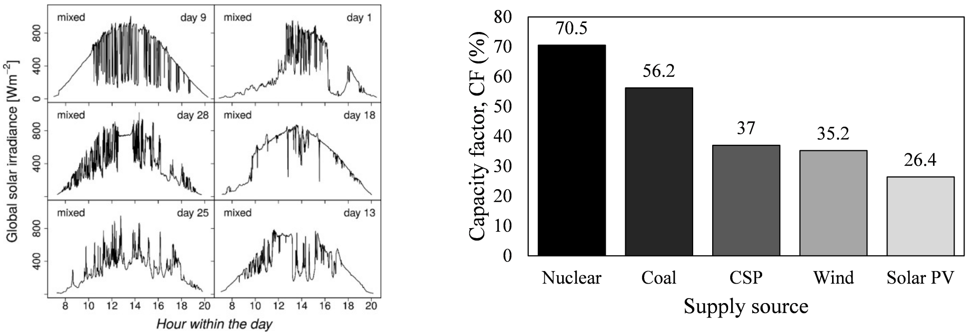

(a) (b)

Figure 2.1: (a) Time-series data capturing different degrees or “mixtures” of intermittent solar energy (Blaga and Paulescu, 2018). (b) Capacity factors per supply source for South Africa during 2020 (data obtained from Calitz and Wright, 2021).

Intermittency can introduce challenges restricting RE’s potential to dominate the energy market (Heal, 2009). This is especially relevant in South Africa where power generation is historically, and for the foreseeable future, dominated by the coal market (Department of Energy, 2019). According to Hirth (2014), variability will become a significant concern in electricity markets with high intermittent RE shares. Other authors echo similar concerns.

Research by Brouwer *et al.* (2014) refers to various studies indicating challenging “power system impacts” with increased shares of intermittent RE. Challenges include: higher reserve capacity, sub-efficient performance of thermal power plants and RE curtailment. Brouwer *et al.* (2014) concludes that intermittent RE at 20 % uptake exerts sizeable impact on present-day power systems. For the South African power system, ancillary services will also increase at 20 % uptake, in line with the aforementioned research. However, this should not be of concern at least up to 2030 (Department of Energy, 2019).

Furthermore, maintaining a short-term energy balance within the power system becomes costly (Kiviluoma, 2013) and inherently risky (Department of

---

dominant intermittent RE sources, solar PV and wind (Pearre and Swan, 2015; Department of Energy, 2019). Without energy storage, they are non-dispatchable (Lovegrove *et al.*, 2018).

Energy, 2019) with increased intermittent RE levels. It can be improved by reinforcing system flexibility (Denholm *et al.*, 2015), through, for example, adequate energy reserves and storage (Notton *et al.*, 2018). According to Notton (2015), a poor supply-demand balance can thwart reliability, quality and continuity of service from the electrical system. A network with increased intermittent RE uptake also complicates grid management (Gross *et al.*, 2006; Lara-Fanego *et al.*, 2012). Holistically, research recognises that intermittency escalates costs (Joskow, 2008; Milligan *et al.*, 2011; Hirth, 2014) and electricity sales prices (Kearns, 2017). As electric energy storage is capable of balancing supply with demand, it is imperative to intermittent energy systems (McLarnon and Cairns, 1989; IEC, 2011).

2.1.2 The Duck Curve

Intermittency aside, solar PV exhibits a characteristic diurnal supply profile with abundant daytime output (Schöniger *et al.*, 2020) and a temporal mismatch between peak output and peak network demand (Hou *et al.*, 2019). Especially as more cheap solar PV is harnessed (IEA, 2018; Hou *et al.*, 2019), the residual demand (total system load less renewable supply) met by real time dispatchable generation dips during central daylight hours, where the PV supply peaks. It also decreases annually with increased solar PV uptake. A resulting demand profile widely known to the electricity sector (Lazar, 2016) takes shape for certain times of the year (CAISO, 2013), as illustrated in Figure 2.2, with the industry moniker of "duck curve".

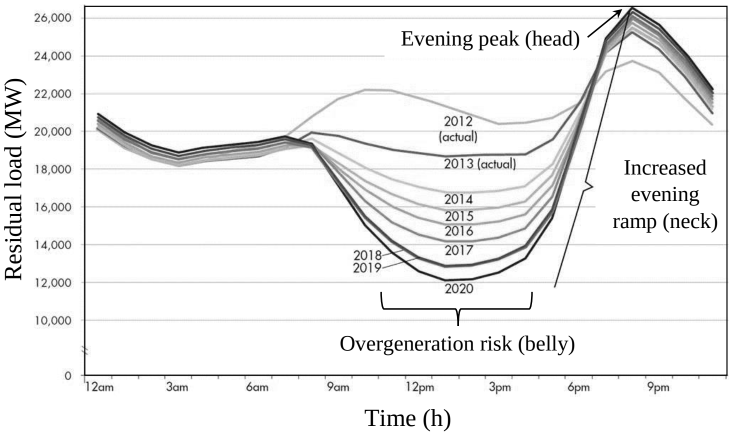

Figure 2.2: Illustrating the duck curve (adapted from CAISO, 2013).

The figure communicates the impact of increased PV uptake on the power system (Hou *et al.*, 2019). Illustrative in nature, the duck's belly represents the period of lowest residual load where solar PV generation peaks (Denholm *et al.*, 2015), the head the ever-growing evening peak, and the neck the steepening evening ramp (Lazar, 2016). The duck curve introduces several challenges for traditional power utilities. They can be identified as the following (CAISO, 2013):

1. Ramping flexibility: the residual load ramps faster than the total load (Notton *et al.*, 2018; IEA, 2018);
2. Quick response time and flexibility: frequent changes in dispatchable output is required to adapt to the residual load (Notton *et al.*, 2018);
3. Overgeneration mitigation: overgeneration (supply exceeding demand) impedes the real time electrical supply-demand balance (CAISO, 2013). Dispatchable generators operate at no or reduced output characterised by low efficiency (Gross *et al.*, 2006; Black and Strbac, 2006), elevated wear-and-tear of units and higher cost of generation (Notton *et al.*, 2018).

Even though Figure 2.2 originates from the CAISO (California Independent System Operator), flexibility challenges can apply to any country deeply invested in solar PV (IEA, 2018). The duck curve effect has attracted concern in the South African power system as well. Due to the significant uptake of solar-derived RE, the South African power utility (Eskom) anticipates excess midday capacity and recognises the need for load-shifting technologies during this period (Eskom, 2018). According to the 2019 Integrated Resource Plan, South Africa's installed solar PV capacity is expected to grow by 462 % (and wind by 796 %) from 2019 to 2030 (Department of Energy, 2019).

To align the residual load with the capabilities of dispatchable generators in a future system with high shares of solar PV generation, several strategies are proposed to alleviate (flatten) the duck curve. *Inter alia*, the minimum generation level can be lowered, if possible (Denholm *et al.*, 2015). Concerning load-flattening strategies (lowering peaks and lifting troughs), surplus RE can be curtailed, only to repress RE's economic and environmental benefits (Denholm *et al.*, 2015). It can also be exported depending on neighbouring entities' needs (CAISO, 2013).

Further research by Hou *et al.* (2019) illustrates that high solar PV uptake aggravates ramping requirements and uncertainty, indicating a need for flexible generators with adequate ramping capabilities. Load can also be shifted via responsive demand programmes, whereas supply via electric energy storage (Lazar, 2016). The latter strategy, reckoned imperative in maintaining grid stability (Argyrou *et al.*, 2018; Steinmann *et al.*, 2019), is considered in this thesis. Denholm *et al.* (2015); Lazar (2016); Hou *et al.* (2019) offer an overview on other strategies and related studies.

2.2 Electrical Energy Storage

In the future power system, electric energy storage can restore dispatchability in RE. This section considers its fundamentals and grid-scale service provision.

2.2.1 Electric Energy Storage Fundamentals

All electrical energy storage technologies fundamentally convert electricity (which cannot be stored) into a form of energy that can be stored, to be converted back to electricity when needed. As such, power conversion equipment and a storage medium are required (Denholm *et al.*, 2021). Sought-after storage characteristics for grid-scale RE integration include: a large power rating and capacity, high efficiency, low cost and geographic independence (Antonelli *et al.*, 2017).

Electric energy storage timescales mainly conform to bulk storage (long discharge periods: operation across hours to weeks), load shifting (medium discharge periods: minutes to hours) and power quality (short discharge periods: seconds to minutes) (IEC, 2011; Staffell and Rustomji, 2016). Utility-scale storage systems possess capacities ranging from several to hundreds of megawatt hours (IRENA, 2019). Energy can also be stored in various forms.

Existing electric energy storage forms belong to four main categories (Suberu *et al.*, 2014): mechanical (such as flywheels and pumped hydroelectricity storage), electrical (capacitors), chemical energy (electrochemical storage devices) and thermal (high and low temperature storage systems). Storage technologies are widespread and a complete review is beyond the scope of this thesis. Instead, thorough reviews and overviews of state-of-the-art technologies have already been conducted by Mahlia *et al.* (2014); Akinyele and Rayudu (2014); Luo *et al.* (2015); Koohi-Fayegh and Rosen (2020).

It is noted that pumped hydro storage possesses the greatest technological maturity (Pearre and Swan, 2015; Staffell and Rustomji, 2016; Dumont *et al.*, 2020) and accounts for up to 97 % (and growing) of the global energy storage capacity (IEA, 2018). Furthermore, three storage categories are primarily considered for solar thermal applications. These include sensible heat storage (facilitating a change in temperature), latent heat storage (facilitating a change of phase) and thermochemical energy storage (facilitating a reversible chemical reaction) (Stine and Geyer, 2001; Pelay *et al.*, 2017). Sensible heat storage technologies are most dominant and mature (Pelay *et al.*, 2017).

2.2.2 Grid-scale Services

EES's primary attribute constitutes the decoupling of energy supply from demand (McLarnon and Cairns, 1989). This can be exploited to provide tailored grid services, specifically RE time-shifting. Its role in providing inertial frequency support is also considered. An overview of additional electric energy storage grid services not within this thesis' scope (such as load-following, frequency response and voltage support) can be found in IEC (2011); Akhil *et al.* (2015); Pearre and Swan (2015); Mostafa *et al.* (2020).

2.2.2.1 Energy Time-shifting

Energy time-shifting entails the storage of surplus energy during periods of overproduction (lower demand or off-peak periods) with discharge at periods of underproduction (higher demand or peak periods). This can reduce RE curtailment in RE-rich power systems (Pearre and Swan, 2015) and initiate arbitrage if the low-demand (charging) electricity tariff is cheaper than during high-demand (discharging) periods (Akhil *et al.*, 2015).

This thesis considers time-shifting in the context of the duck curve (Figure 2.2). As proposed in Hou *et al.* (2019); Dumont *et al.* (2020), electric energy storage can charge surplus solar PV during the overgeneration window and discharge elsewhere, such as the evening ramp and peak. The requisite is grid-scale storage systems with capacities of 4 hours to 8 hours (Dumont *et al.*, 2020). Arbitrage aside, this strategy can potentially assist in flattening the duck.

2.2.2.2 Inertia as Frequency Support

Frequency is a key indicator of the power network's supply-demand balance (Soliman *et al.*, 2021). When unbalanced (due to an unforeseen event), the system's frequency deviates at a rate governed by the magnitude of initial mismatch and instantaneous aggregate system inertia (Akhil *et al.*, 2015; Soliman *et al.*, 2021). In any power grid, it is imperative that the frequency f be confined to f_{nom} (Farmer and Rix, 2020), the nominal frequency.

Inertia is a grid service (or attribute rather) that preserves system reliability. Systems with higher levels of inertia initially experience lower rates of change of frequency (RoCoF) decay with the onset of a disrupting event, such as a plant or transmission line outage. As a result, system operators gain longer recovery periods (Δt_{gain}) for restoring imbalance before resorting to under-frequency load shedding (UFLS) as $f \leqslant f_{\text{min}}$ (Denholm *et al.*, 2020). Therefore, inertia maintains the initially essential transient stability (Farmer and Rix, 2020). This dynamic is illustrated in Figure 2.3.

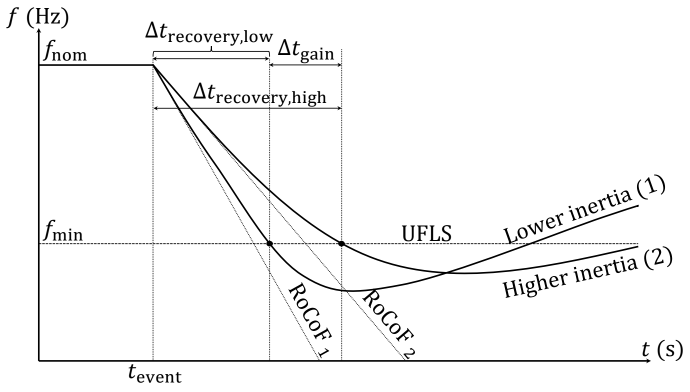

Figure 2.3: Dynamics of system inertia and frequency response.

Inertia of the power system frequency is a byproduct of a grid historically supported by synchronous generators with large rotating masses (Farmer and Rix, 2020). System inertia can be viewed as the aggregate rotational kinetic energy stored by all rotating masses electromagnetically coupled (synchronised) with the grid (National Grid, 2016).

However, as more RE (specifically "inertialess" inverter-based technologies) enters the power mix, the system inertia declines and the network becomes increasingly sensitive to imbalances (higher rates of change of frequency). The predicament (perhaps a third grid-scale challenge) unfolds where the integration of large-scale RE generation will exert more imbalance (intermittency and the duck curve) and deprive the system of its inherent inertia. This aggravates stability and reliability (Obaid *et al.*, 2019; Farmer and Rix, 2020).

As an expected 11 GW of the South African coal fleet will be decommissioned between 2019-2030, with a further 24.1 GW up to 2050 (Department of Energy, 2019), it is submitted that inertia (and capacity decline) can become a growing concern for the network. How can Carnot batteries aid this transition, *inter alia*? This thesis only considers frequency support in the context of inertia viewed as a passive, free and automatic support (Farmer and Rix, 2020). It does not consider other active frequency recovery, control or intervening techniques and services utilised by the system operator. For an overview on such techniques, the reader is referred to Tielens and Van Hertem (2012); Obaid *et al.* (2019); Farmer and Rix (2020).

2.3 The Carnot Battery

Carnot batteries are gaining recognition as an electric energy storage technology (Dumont *et al.*, 2020; Dumont and Lemort, 2020) that can resolve the residual load challenge (Trieb and Thess, 2020). It primarily stores electrical energy as thermal energy, can be augmented with additional thermal energy inputs for performance enhancement and contains at least an input and output for electricity. During charge cycles, electric energy is converted into thermal energy, which manifests a temperature difference, ΔT, between a high and low-temperature reservoir. The heat is stored in the high-temperature reservoir until discharge commences (Dumont *et al.*, 2020).

During discharge, the stored thermal energy is displaced from the high to the low-temperature reservoir. A portion of this heat drives a heat engine while the residual heat is stored in the low-temperature reservoir. Electricity is recovered by directing the heat engine's work through a generator. Electricity-to-heat conversion (charge mode) can be facilitated by resistive heating or a heat pump, whereas heat-to-electricity conversion (discharge mode) by a power cycle such as the Rankine or Brayton. In either mode, a larger ΔT increases both the specific work absorbed and extracted (Dumont *et al.*, 2020).

The Carnot battery provides several technical advantages over other storage technologies. It can be readily scaled up, is geographically independent (unlike pumped hydro storage) and the thermal reservoirs (tanks) require relatively low operating pressures (Dumont *et al.*, 2020). Due to little degradation, life expectancies spanning 20 years to 30 years are not uncommon. Abundant storage materials and state-of-the-art components can be utilised and ecological impacts are minimal (Steinmann *et al.*, 2019). What is more, the heat engine's inherent inertial support is recognised for its potential grid service provision (Section 2.2.2.2), an attribute absent in inverter-based storage alternatives.

Various Carnot battery sub-technologies and comparisons exist. As this thesis prioritises its promising application in CSP plants, these cannot be considered in full. The reader is directed to Steinmann *et al.* (2019); Dumont *et al.* (2020); Trieb and Thess (2020) for content in this regard. Continuing, Section 2.4 considers how CSP plants with thermal energy storage, especially once applied as Carnot batteries, could address the outlined grid-scale challenges.

2.4 CSP Plants as Carnot Batteries

CSP plants with molten salt thermal energy storage (TES) are uniquely positioned as dispatchable RE generators with inherent inertial support. This section provides a technical overview of the technology and considers its potential application as a Carnot battery.

2.4.1 Thermal Energy Storage in CSP Plants

To extend its electrical output, CSP plants are increasingly equipped with TES units (Pelay *et al.*, 2017). This stores surplus solar thermal energy produced during periods of excellent solar resource that would otherwise be curtailed. In doing so, energy can be time-shifted to periods of low or no solar resource (Stine and Geyer, 2001). This includes intermittent spans or nighttime, or across periods of high or low demand on the grid (Enescu *et al.*, 2020).

Unlike other RE plants, CSP with TES is distinguished by its: inherent dispatchability (Brun *et al.*, 2020; Zaversky *et al.*, 2020), operating flexibility (Brun *et al.*, 2020), stability of output (Pelay *et al.*, 2017), wide-scale deployment and proven capability (Feldman *et al.*, 2016). The cost-effective storage of thermal energy (Barnes, 2017; Zaversky *et al.*, 2020) differentiates CSP from other RE technologies (Barnes, 2017). Current solar PV electricity prices, however, are cheaper than CSP (Gedle *et al.*, 2020; Mahdi *et al.*, 2020). CSP prices have decreased at a slower rate (Gedle *et al.*, 2020).

Two-tank TES schemes with molten salt as sensible heat storage medium are commercially mature, widely used (Brun *et al.*, 2020) and economic (Riffelmann *et al.*, 2020). Two-tank schemes include: indirect systems for parabolic trough plants and direct storage systems for central receiver plants (Brun *et al.*, 2020). Parabolic trough plants are the most widespread CSP technology (Poole, 2017). Figure 2.4 describes the storage blocks of two-tank direct and indirect sensible heat storage systems. This thesis limits its scope to these technologies specifically. An overview of other CSP TES schemes is found in Kuravi *et al.* (2013); Liu *et al.* (2016); Pelay *et al.* (2017); Brun *et al.* (2020).

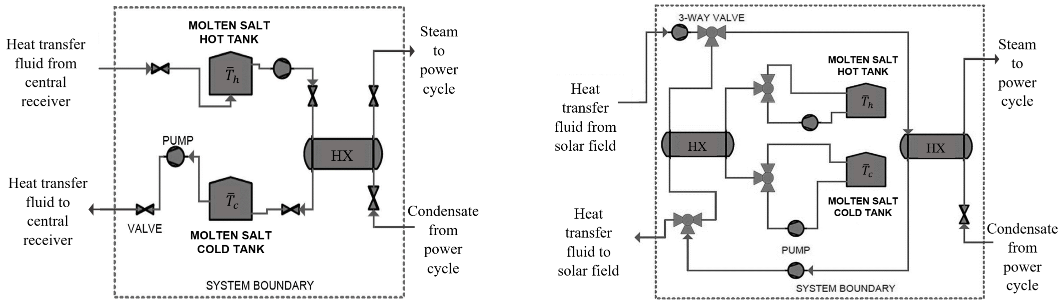

(a) (b)

Figure 2.4: (a) Direct TES scheme. (b) Indirect TES scheme. "HX" abbreviates heat exchanger (adapted from Thaker *et al.*, 2017).

In direct schemes, the heat transfer fluid (HTF) and heat storage fluid (HSF) are identical (Pelay *et al.*, 2017). Molten salt, housed in large storage tanks, stores excess heat collected at the receiver and undergoes temperature cycles typically between 280 °C to 565 °C (Steinmann *et al.*, 2019). For indirect schemes however, thermal or synthetic oil in the operating range of 293 °C to 393 °C (SolarPACES, 2018) is used as HTF, with molten salt as the HSF (Brun *et al.*, 2020).

Compared to molten salt, thermal oil's lower melting point eliminates its risk of freezing as a HTF in the solar field (Brun *et al.*, 2020). However, thermal oil is not used as HSF. Unlike molten salt, it is more costly (requires larger storage volumes) and volatile to store at elevated temperatures (such as 393 °C to 565 °C) for prolonged periods (Brun *et al.*, 2020). A distinguishing thermodynamic drawback of the indirect scheme, considering Carnot's efficiency law, is its underutilised hot molten salt storage temperature $\overline{T}_h$. It is limited by the HTF's narrower thermal operating range (Mahdi *et al.*, 2020; Gedle *et al.*, 2020). This could be overcome by a Carnot battery application (Section 2.4.2), allowing the system to store more heat than otherwise attainable.

2.4.2 CSP Carnot Battery Applications

Due to TES, commercial CSP plants are uniquely positioned as RE technologies for a Carnot battery application. By adding an upfront electric-to-thermal conversion process such as resistive heating, surplus renewable electricity can be converted into thermal energy. Together with the pre-existing solar thermal energy, this energy is stored within the CSP plant's TES system. As the power block facilitates the final thermal-to-electric conversion, the fundamental requirements for a Carnot battery, as per Section 2.3, are realised. As such, CSP Carnot batteries could fulfill many of the Carnot battery electric energy storage benefits outlined and attempt to resolve the grid-scale challenges of mass RE integration. This proposition forms the focus of numerous studies.

Riffelmann *et al.* (2020) analyse four frameworks for CSP-PV hybridisation, of which two constitute a Carnot battery with direct TES. The first involves CSP charging TES during the day with nighttime output only. An oversized PV plant delivers nominal daytime output and charges TES with surplus solar PV via electric heating. The second framework fully replaces the solar field with a PV plant for daytime output. TES is charged with surplus solar PV via electric heaters, while the CSP power cycle generates electricity during the night. Based on LCOE (levelised cost of electricity), it is concluded that the former framework is most economic for average direct normal irradiance (DNI) regions. Thus the solar field remains a valuable constituent. For higher DNI regions, co-locating (i.e. no physical integration) CSP with PV becomes more economic than the two Carnot battery configurations.

According to Mahdi *et al.* (2020), the temperature limits imposed by thermal oil on molten salt in a parabolic trough plant's TES can be overcome by PV-powered resistive heating. This can close a 385 °C to 565 °C divide in the hot molten salt. They conclude that high-temperature solar salt decomposition in resistive heaters for CSP-PV Carnot battery applications can be evaded.

Research by Gedle *et al.* (2020) considers parametric optimisation of a CSP-PV Carnot battery via four design parameters. Electric heaters (within 100 MW to 350 MW test range) located in series between the thermal oil/molten salt heat exchanger and hot tank, charge the TES (6 h to 14 h test range) with low cost surplus solar PV. This boosts the hot molten salt temperature to 565 °C. Based on the LCOE, each heater capacity corresponds to an optimum TES capacity. The optimum PV capacity increases with the allocated heater capacity. Furthermore, a Carnot battery application is found to be more economic than co-locating CSP with PV. Co-location requires a larger salt mass and more heat for an electricity production equivalent to the Carnot battery's.

In Schöniger *et al.* (2020) three system configurations for a nighttime solar power market are considered, namely: solar PV with Li-ion battery storage, solar PV with TES (with a power cycle, but no solar field) and CSP with TES. The second configuration comprises a Carnot battery, in which electric heating converts solar PV into thermal energy for TES. In accordance with Riffelmann *et al.* (2020), their results suggest that PV with TES is always more expensive than CSP with TES for all cost scenarios tested. The solar field is an essential component for the cost-competitiveness of CSP plants.

In Garcia *et al.* (2013) the temporal operation of a CSP with TES Carnot battery, facilitating electricity buy-back from the grid, is optimised based on revenue. Electric heaters charge the hot molten salt portion in a thermocline TES system. Among other scenarios, the authors consider the economic feasibility of purchasing off-peak electricity for charging TES. Despite a LCOE increase, results indicate a substantial revenue and profit growth with electric heaters included, when compared to the same case without electric heaters.

Research by Zhai *et al.* (2017) also assesses a CSP-PV Carnot battery. Excess and possibly variable solar PV is stored as thermal energy in a CSP plant's direct molten salt TES, as opposed to chemical batteries. Reaching sunset and after, CSP electricity is generated to meet a fixed load as the PV plant's output decays. Results indicate that such a system achieves increased stability and fluidity in power output for a constant-output dispatch scheme. The Carnot battery integration promotes the utilisation of solar energy.

The 800 MW solar hybrid project in Midelt is the first-of-its-kind for CSP Carnot batteries in industry. Excess PV electricity, usually stored in chemical batteries with limited capacity, is converted to thermal energy via electric heaters. These are situated in-line between the hot and cold storage tanks in the parabolic trough plant's TES system and allow solar PV to charge the TES. This can mitigate solar PV curtailment (Section 2.1) and overcome the thermal limit imposed by the plant's HTF on the HSF (Section 2.4.1). The hot molten salt can thereby attain temperatures up to 565 °C (Kraemer, 2020).

2.5 Competitiveness of CSP Carnot Batteries

The last section argues that the cost-effective bulk storage of surplus solar PV (or other RE generation) is realised in CSP plants with TES, rather than battery (chemical) energy storage systems. A recurring observation is the competitiveness of CSP with TES at larger storage capacities; whereas PV with battery energy storage is limited to smaller capacities.

Currently, Li-ion batteries are the most widespread, commercially mature (IRENA, 2019; Rahman *et al.*, 2020) and cost effective (Lovegrove *et al.*, 2018) energy storage technology in the market. However, it is not widely acknowledged as a cost effective and viable solution for utility-scale energy storage (Suberu *et al.*, 2014; Killer *et al.*, 2020; Fan *et al.*, 2020). The deployment of alternative batteries for utility-scale storage are therefore also limited.

Lovegrove *et al.* (2018) discover that the LCOE of Li-ion batteries combined with solar PV or wind, escalates with increased storage capacity. The lowest LCOE occurs at roughly 0.5 hours of storage, and remains competitive up to 3 hours. CSP with TES becomes competitive at 6 hours upwards. Thus, batteries are apt for short-duration grid-scale services such as smoothing intermittent generation and reducing sudden ramp rates. According to Biswas *et al.* (2020), high battery storage costs limit solar PV's potential for true dispatchability.

Similarly, in Feldman *et al.* (2016) it is concluded that CSP with TES allows larger storage capacities. This leads to lower cost energy production compared to PV with battery storage, which can only store a smaller fraction of the available solar energy. Operational constraints such as startup requirements, startup losses and minimum operating levels can influence the value of CSP energy however. PV with battery energy storage is exempt from those constraints, allowing for quick response to power system needs. Nonetheless, the provision of operating reserves for power system needs can reduce battery lifespan. According to Zhai *et al.* (2017), a synergy can exist between low-cost solar PV production and high capacity, low cost TES in CSP plants. The cost-effective TES serves as a substitute for expensive solar PV battery storage systems of which the uninterrupted use becomes costly.

Analyses from Schöniger *et al.* (2020) echo similar findings. A nighttime solar power market is best split between PV with batteries for short storage spans and CSP with TES for longer spans. When solar PV is stored in TES as opposed to batteries, it benefits from the lower specific storage costs associated with TES. This becomes evident when larger storage capacities are required.

Notwithstanding, Li-ion storage systems possess high round-trip efficiencies (Killer *et al.*, 2020) typically exceeding 85 % (Castillo and Gayme, 2014; Akinyele and Rayudu, 2014; Zakeri and Syri, 2015; Nikolaidis and Poullikkas, 2018). In CSP Carnot batteries however, the power cycle thermal efficiency limits the Carnot battery's overall maximum round-trip efficiency. CSP Rankine power cycle thermal efficiencies typically range below 50 % (Franchini *et al.*, 2015; Poole, 2017; Praveen *et al.*, 2018; Lubkoll and Claassen, 2019). In applications where high round-trip efficiencies are preferred, CSP Carnot batteries would fall short in comparison to Li-ion storage systems.

2.6 Conclusion

With increased RE uptake, the literature emphasises numerous grid-scale challenges centred around the "symptoms" of intermittent power supply, the duck curve (Section 2.1) and inertial decline (Section 2.2.2.2). Electric energy storage (Section 2.2.1) is considered important in restoring the element of dispatchability historically known to the grid, in an effort to mitigate the aforementioned challenges. This can be achieved through various grid-scale services, for instance energy time-shifting and inertia as frequency support (Section 2.2.2). This thesis echos the potential of Carnot batteries as an electric energy storage technology (Section 2.3). Alongside numerous studies, it recognises the aptitude and potential shortcomings of CSP plants with TES as Carnot batteries (Section 2.4) in lieu of competitive chemical battery alternatives (Section 2.5).

Chapter 3

Research Outline

3.1 Motivation and Contribution

The motivation for this research is to a great extent woven into the literature study. CSP Carnot batteries show potential to address a variety of challenges outlined, including grid-scale energy storage, dispatchable RE generation and temperature limits in parabolic trough plants. In addition, global direct normal irradiance maps (see the Global Solar Atlas) confirm South Africa's undeniable solar thermal energy potential - a country serving as the perfect location for CSP Carnot battery research and development. This thesis attempts to promote the former. Contributing thereto, it aims to address certain shortcomings identified in conducting the literature study.

Studies tend to focus on the end-result of the Carnot battery application, such as LCOE-level changes. Though LCOE is a useful parameter to rank economic competitiveness of different generation technologies or retrofits within a single technology, it fails to convey the technical value of the service provided by the technology. Therefore, the value of the technology's service behind the economic outcome should also be considered.

Studies research Carnot battery applications and measure performance at the single net output-level. Few consider how the CSP plant and its TES system would otherwise respond to the application. Often, operational trade-offs within the CSP plant in light of its application are not highlighted and the best utilisation of the CSP plant remains unknown.

Studies approach design problems from the grid or curtailing plant's perspective, that is: "design a Carnot battery to mitigate pre-determined surplus RE". Though relevant, it can be approached from the Carnot battery's perspective instead: "what is the best way to design a Carnot battery for a variable quantity of potentially abundant RE?

The sensitivity of techno-economic performance results to economic and technical parameters is often left unexplored. How does the former respond to changes in the latter? Which parameters exert the strongest influence on the techno-economic outcomes?

Studies successfully conduct single or multi-objective system optimisation. In some cases however, the mathematical significance of and insights behind optimum results could be explored in greater detail. What constitutes an optimum CSP Carnot battery design and why?

Lastly, the selection of optimisation objective functions is partly motivated. The trade-offs between objective functions, a prerequisite for multi-objective optimisation, is not fully revealed.

3.2 Research Objectives and Questions

A summary of the research objectives and questions follows:

1. Develop a techno-economic computational model of a Carnot battery application in a conventional parabolic trough CSP plant;
2. Establish the Carnot battery's economic response:
   a) What insights arise from changes in design and economic parameters?
   b) Do barriers to economic synergy exist?
3. Establish the CSP plant's technical response as a Carnot battery:
   a) How does the application alter the CSP plant's operation?
   b) Do barriers to technical synergy exist?
4. Examine the value and service potential of the CSP Carnot battery:
   a) Is CSP uniquely positioned to address the grid-scale challenges of mass RE integration; more so once applied as a Carnot battery? If so, how does it achieve this?
   b) Can around-the-clock power generation be promoted?
5. Assess the Carnot battery optimisation problem:
   a) State the optimisation problem and formulate a solution algorithm;
   b) Which Carnot battery metrics are appropriate objective functions, and why? What trade-offs can be revealed between them?
   c) What constitutes an optimum Carnot battery design and why?

3.3 Research Overview

The remaining chapters are structured as follows: Chapter 4 documents the research methodology, formulation of the techno-economic computational model and its validation. Chapter 5 states the optimisation problem and formulates an appropriate solution algorithm. Chapter 6 contains computational results that attempt to answer questions and objectives of Section 3.2. The thesis is concluded in Chapter 7.

Chapter 4

Computational Modelling

4.1 System Technical Overview

Section 2.4.1 emphasises thermodynamic drawbacks of indirect TES in parabolic trough plants, compared to direct TES in central receiver plants. In the Midelt project (Section 2.4.2), the temperature limit of thermal oil (the HTF) imposed on the hot molten salt (the HSF) is overcome by electrically heating the molten salt prior to storing it in the hot tank. The heater is powered by excess PV electricity. In this thesis, a system is configured that builds upon that. However, this system aims to exploit promising baseload and energy time-shifting capabilities of the parabolic trough plant. A conventional plant configuration, and not that of Midelt, is capable of sustaining both. This is where the system notably differs from the Midelt project, which generates power directly from TES (higher thermal efficiency) after sunset (Kraemer, 2017; Masdar, 2022).

The system configuration is proposed in Figure 4.1. It consists of a parabolic trough field, indirect TES and a Rankine power cycle. When the field delivers thermal energy, the power block has priority in consuming it (i.e. HTF: solar field→*9*→*10*→solar field, according to Figure 4.1's numbering scheme). Once the power block receives its design thermal power, excess thermal energy is sent to storage by diverting a fraction of the solar field HTF mass flow through the HTF/HSF HX (solar field→*1*→*2*→solar field). Heat is exchanged with cold molten salt (*8*→*3*→*4*→*5*) and removes thermal power in excess of the power cycle thermal demand from the HTF. Thereafter, the heated molten salt is stored in the hot tank (*5*). Cold HTF returns to the solar field inlet. This process is termed the solar thermal charge cycle. Once the TES system is fully charged, the excess thermal energy is discarded by defocusing the solar field.

In Figure 4.1 the heater block addition is highlighted in blue. One hour after solar thermal charging commences, hot molten salt is extracted and circulated through the heater block (*5*→*7*→*5*) to increase $\overline{T}_h$. The heaters consume $\dot{P}_{H,\text{tot}}(t)$ renewable electricity in doing so. This process is termed the RE charge cycle. The heater block does not initiate a charge cycle of its own, because its primary objective is to boost the solar thermal charge cycle. The time delay ensures sufficient accumulation of hot HSF prior to extraction.

When the power cycle requires energy from the TES, RE charging ceases and hot molten salt is discharged through the HSF/HTF HX ($5 \rightarrow 6 \rightarrow 4 \rightarrow 3 \rightarrow 8$). It exchanges heat with part or all of the cold HTF ($2 \rightarrow 1 \rightarrow 9 \rightarrow 10 \rightarrow 2$), depending on the field's power output. Consequently, cold molten salt is stored in the cold tank (8) until a subsequent solar thermal charge cycle commences. This process is termed the discharge cycle.

A technical advantage of the application proposed in Figure 4.1 is the heater block decoupled from TES (i.e. in parallel operation with TES). This is opposed to in-line (series) configurations utilised in previous studies (Section 2.4.2). Electric heaters are also simpler and cheaper compared to heat pump technologies (Dumont *et al.*, 2020).

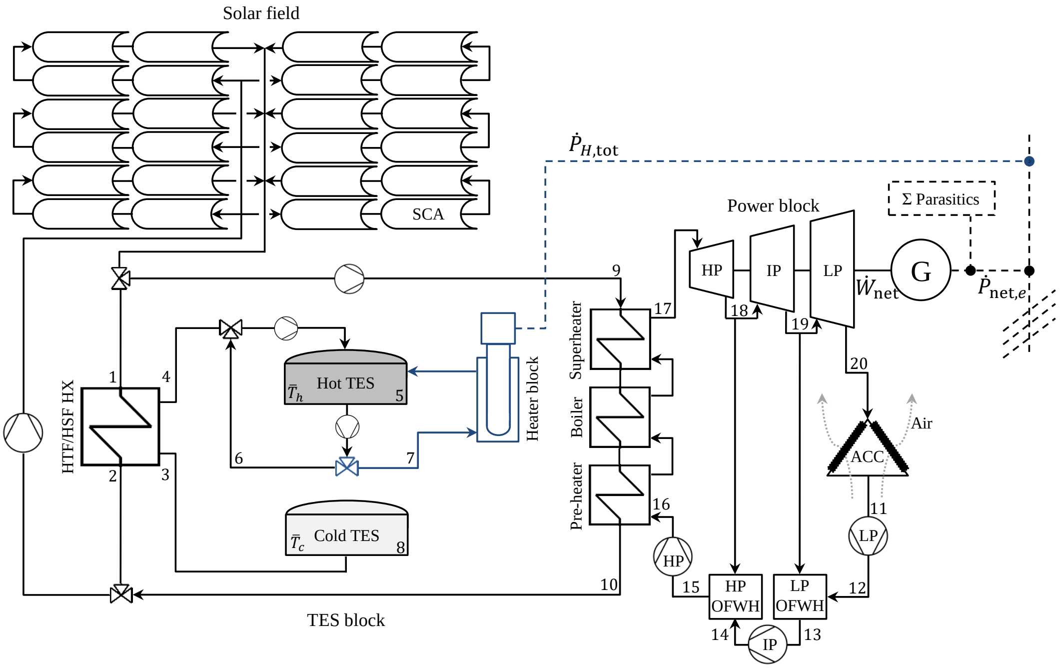

Figure 4.1: Proposed CSP Carnot battery system configuration.

It is emphasised that the Carnot battery application does not entail a retrofit to an existing or operational plant (for example, Kathu Solar Park). This would restrict many design variables to actual design specifications. This limits the potential for researching fundamental insights by freely varying such parameters. Furthermore, existing plants have hot storage tanks constructed from carbon steel, which limits the hot HSF temperature to $\leqslant 400$ °C (Kuravi *et al.*, 2013). This makes a Carnot battery retrofit infeasible without the addition of a third stainless steel hot tank and new molten salt steam generator. The research starts from a conventional parabolic trough plant configuration to propose a Carnot battery application in a greenfield or "future" plant. Kathu Solar Park only serves as a starting point for obtaining representative data.

4.2 Mathematical Modelling

This section details the mathematical modelling of the standard parabolic trough plant in Figure 4.1 and its Carnot battery application. Since SAM (elaborated in Section 4.2.1) cannot facilitate the required Carnot battery application, a computational model is formulated for this purpose. The modelling approach, simulation tools and control logics are also considered.

4.2.1 Modelling Philosophy

The modelling philosophy is based on the strategy outlined in Figure 4.2.

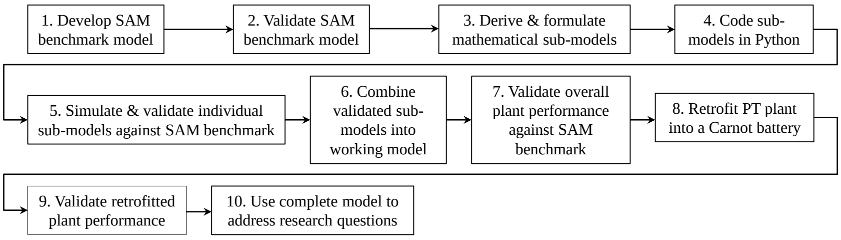

Figure 4.2: Modelling strategy.

Step one:

A parabolic trough plant is modelled in SAM (System Advisor Model) version 2020.2.29 r3 (Appendix A) and serves as a benchmark to assess the validity or accuracy of self-developed models. The 100 MW Kathu Solar Park plant was selected due to the availability of plant specifications. SAM is an open source RE modelling tool developed by the National Renewable Energy Laboratory (NREL) (NREL, 2020*b*). It is considered a benchmark software when validating newly developed models (Lubkoll and Claassen, 2019). The compliance of SAM with CSP modelling guidelines is presented in Kesseli *et al.* (2018).

Step two:

To validate the benchmark model, SAM output metrics are compared to values available from literature (Section 4.2.2).

Step three:

This entails the formulation of plant sub-models: solar field (Section 4.2.3), power cycle (Section 4.2.4), TES (Section 4.2.5) and a financial model (Section 4.2.6). Flexibility and a fundamental understanding of CSP are sought-after advantages in deriving these models, as opposed to utilising a simulation software package. As the research objectives are not centred around the derivation of a detailed CSP model, a high-level modelling approach is followed. To reduce model complexity and computational effort, a pseudo steady-state approximation is mostly adopted. Steady-state equations are solved at discrete time steps. Time steps are linearly interpolated. Iterations stop when an iteration cutoff limit or a convergence tolerance is reached. Variables are independent of space, but not time. Consequently, all models are lumped.

Step four:

Sub-models are coded in Python 3 (Rossum and Drake, 1995), an open source scientific computing programming language. This allows individual sub-models to be refined and validated separately against the SAM benchmark.

Step five:

Sub-models are individually simulated, internally validated (Appendix C.1) and compared to SAM benchmark outputs (Appendix C.2).

Step six:

Sub-models are combined into an overall working model by linking inputs and outputs and introducing appropriate control strategies.

Step seven:

The simulation calculates plant performance over a typical year with hourly time steps, which then establishes annual and lifetime technical and economic metrics (Wagner *et al.*, 2017). According to Kesseli *et al.* (2018), this is adequate for pre-feasibility studies. Overall plant performance is validated against the benchmark in a similar fashion (Section 4.2.7 and Appendix C.3).

Step eight:

The validated plant is applied as a Carnot battery by introducing the heater block shown in Figure 4.1 (Section 4.2.8).

Step nine:

The performance of the Carnot battery plant is validated internally by appropriate energy and mass balances (Appendix C.4).

Step ten:

This final working model (the “performance model” hereon) is used to address research objectives and questions of Chapter 3.

4.2.2 SAM Benchmark Model

A benchmark parabolic trough model is implemented in SAM (Appendix A). Benchmark outputs are compared to literature values in Table 4.1. Results are for uniform dispatch with no consideration towards time-of-delivery (TOD).

The results suggest the SAM model calculates metrics of Kathu Solar Park with reasonable accuracy, using the limited information made publicly available. Even though detailed performance data is lacking, the model predicts the listed output parameters with fair precision. Accordingly, the SAM model is accepted as a valid benchmark model.

Table 4.1: SAM benchmark model results.

Metric	**Unit**	**SAM value**	**Reported value**	**% Diff.**[2]
Annual energy	GWh/yr	380.983	390[3]	−2.31
Capacity factor	%	43.5	44.5[4]	−2.25
TES capacity	MWh	1469.12	1550[5]	−5.22
Total reflective area	m^2	1075000	1047000[5]	2.67
Total land area	km^2	4.601	4.5[6]	2.24

4.2.3 Solar Field

4.2.3.1 Energy and Mass Balance and Control

A technology non-specific analysis is performed on the solar field by placing a control volume (CV) as shown in Figure 4.3. Detailed field optical and thermal modelling is not within scope and therefore a high-level pseudo steady-state model is formulated. The applicability of a pseudo steady-state analysis for the solar field is considered in Appendix B.1.1.

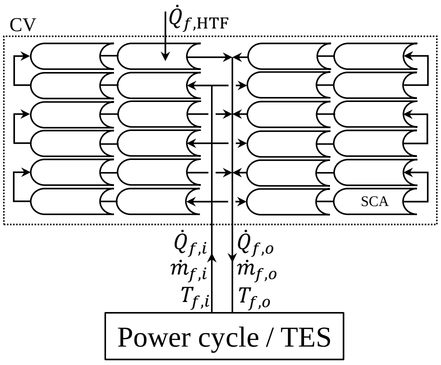

Figure 4.3: Solar field control volume, energy and mass flows. "SCA" denotes solar collector assembly.

---

[2] Relative difference as given by Equation C.2.1.

[3] Van Wyngaardt (2016).

[4] Gazman (2019).

[5] Sener (2021).

[6] Helios CSP (2020).

Under operating conditions, cold HTF from the power cycle/TES block is returned to the field inlet at a temperature $T_{f,i}$ and mass flow rate $\dot{m}_{f,i}$. Progressing though the field, the HTF absorbs $\dot{Q}_{f,\text{HTF}} = \dot{Q}_{f,o} - \dot{Q}_{f,i} = \dot{Q}_{f,\text{HTF,net,abs}}$ net solar thermal power and exits at a temperature $T_{f,o}$ and mass flow rate $\dot{m}_{f,o} = \dot{m}_{f,i}$. $\dot{Q}_{f,\text{HTF}} > 0$ is viewed as the net useful thermal power that other systems, such as the power cycle and TES, can extract from the delivered HTF. Receiver net thermal power to/from the HTF, $\dot{Q}_{f,\text{HTF}} \in \mathbb{R}$, is modelled externally in the SAM benchmark model. This provides an hourly input to the performance model. $\dot{Q}_{f,\text{HTF}} \in \mathbb{R}$ is defined such that:

$$\dot{Q}_{f,\text{HTF}} = \begin{cases} \dot{Q}_{f,\text{HTF,net,abs}} & \text{if} \quad \dot{Q}_{f,\text{HTF,net,abs}} > 0 \\ - \mid \dot{Q}_{f,\text{HTF,loss}} \mid & \text{if} \quad \dot{Q}_{f,\text{HTF,net,abs}} = 0 \end{cases} \tag{4.2.1}$$

where $\dot{Q}_{f,\text{HTF,net,abs}} = \{x \in \mathbb{R} | x \geqslant 0\}$ is the net thermal power absorbed by the field HTF and $\dot{Q}_{f,\text{HTF,loss}}$ is the hourly field HTF thermal losses in the absence of net absorption. The total field mass flow rate delivered, is balanced as:

$$\dot{m}_{f,o} = \mid \dot{Q}_{f,\text{HTF}} \mid / [\bar{c}_{p,\text{HTF}} \cdot (T_{f,o} - T_{f,i})] = \dot{m}_{f,i} \tag{4.2.2}$$

where:

$$\bar{c}_{p,\text{HTF}} = \frac{1}{T_{f,o} - T_{f,i}} \int_{T_{f,i}}^{T_{f,o}} c_{p,\text{HTF}}(T) dT \approx c_{p,\text{HTF}} \left(\frac{T_{f,i} + T_{f,o}}{2} \right) \tag{4.2.3}$$

with $c_{p,\text{HTF}}(T)$ a HTF specific heat polynomial relation given in Appendix D.1. The approximation is made on the basis of negligible higher-degree ($\geqslant 2$) terms in $c_{p,\text{HTF}}(T)$.[7] HTF is discharged such that $T_{f,o} = T_{f,o,\text{des}}$, with the exception:

$$T_{f,o} = T_{f,i} + \dot{Q}_{f,\text{HTF}} / \left(\bar{c}_{p,\text{HTF}} \cdot \dot{m}_{f,\text{HTF,min}} \cdot N_{\text{loops}} \right) \ \text{ if } \ \dot{m}_{f,o}/N_{\text{loops}} < \dot{m}_{f,\text{HTF,min}} \tag{4.2.4}$$

Furthermore, solar collector assemblies will defocus and discard thermal power when the HTF mass flow rate capacity per loop is exceeded:

$$\begin{aligned} \dot{Q}_{f,\text{disc}} = \dot{Q}_{f,\text{HTF}} - N_{\text{loops}} \cdot \dot{m}_{f,\text{HTF,max}} \cdot \bar{c}_{p,\text{HTF}} \cdot (T_{f,o,\text{des}} - T_{f,i}) \\ \text{if } \dot{m}_{f,o}/N_{\text{loops}} > \dot{m}_{f,\text{HTF,max}} \end{aligned} \tag{4.2.5}$$

Field HTF recirculation, as a means of freeze protection (Pan, 2020), is activated when there is insufficient thermal power for field delivery:

$$\begin{cases} T_{f,i}(t + \Delta t) = T_{f,o}(t) \ \text{(internally)} \\ \dot{m}_{f,o} = \dot{m}_{f,i} = \dot{Q}_{f,\text{HTF}} = 0 \\ \dot{m}_{f,\text{recirc}} = N_{\text{loops}} \cdot \dot{m}_{f,\text{HTF,min}} \end{cases} \quad \text{if} \quad \dot{Q}_{f,\text{HTF,net,abs}} = 0 \tag{4.2.6}$$

As summarised in Table B.1, $\dot{m}_{f,\text{HTF,min}}$ and $\dot{m}_{f,\text{HTF,max}}$ are the minimum and maximum design field HTF mass flow rates per loop, N_{loops} the number of loops in the field and $T_{f,i/o,\text{des}}$ the design field HTF inlet and outlet temperatures.

---

[7] With $T_{f,i} = T_{f,i,\text{des}}$ and $T_{f,o} = T_{f,o,\text{des}}$ as the maximum HTF temperature range, the approximation yields a -0.221 % error relative to the exact method, which is regarded negligible.

4.2.3.2 Sizing the Solar Field

The solar multiple (SM) is defined as (Montes *et al.*, 2009):

$$SM = \left. \frac{\dot{Q}_{f,\text{HTF}}}{\dot{Q}_{\text{PC,in}}} \right|_{\text{des}} \tag{4.2.7}$$

with $\dot{Q}_{f,\text{HTF,des}}$ the field thermal power output at design and $\dot{Q}_{\text{PC,in,des}}$ the power cycle (PC) design thermal power input. A parametric analysis in the SAM benchmark model establishes a relationship between SM and the ratios $N_{\text{loops}}/N_{\text{loops,des}}$, $A_{\text{aperture,refl}}/A_{\text{aperture,refl,des}}$ and $A_{\text{land,tot}}/A_{\text{land,tot,des}}$:

$$Ratio = 0.384 \cdot SM + 0.004 \quad (R^2 = 1) \tag{4.2.8}$$

All parameters scale equally with the SM. N_{loops}, $A_{\text{aperture,refl}}$ (total field aperture reflective area) and $A_{\text{land,tot}}$ (total land area) can be scaled by multiplying their design values with the given ratio at a specified value of the SM. The SAM benchmark model calculates $\dot{Q}_{f,\text{HTF}}(SM, t)$.

4.2.3.3 Parasitic Power Consumption

The HTF pumping power and collector tracing power are the main parasitics modelled in the solar field. They contribute to the overall plant parasitic power consumption. Appendix B.1.2 provides an overview on both.

4.2.4 Power Cycle

4.2.4.1 Cycle Description

A superheated regenerative Rankine power cycle is modelled in Figure 4.4. It consists of three turbine stages: high pressure (HP), intermediate pressure (IP) and low pressure (LP). Heat rejection is achieved through an air-cooled condenser (ACC) unit, which are ubiquitous as cooling units for CSP plants in arid climates (Kröger, 1998). Regeneration is facilitated by high and low pressure open feedwater heaters (OFWH's) and turbine steam bleeding fractions y and z. The steam generator consists of a pre-heater, boiler and super-heater. Hot HTF entering the steam generator transfers heat to the working fluid entering at *16*, which leaves as superheated steam at *17*. Cold HTF is returned to the solar field and/or TES.

According to Wagner and Gilman (2011), the configuration presented in Figure 4.4, together with the cycle specifications summarised in Table B.2, can be considered representative of parabolic trough plants. This basis Rankine cycle is modelled such that performance can simply be scaled at off-design conditions, allowing for fast and large simulations (Wagner and Gilman, 2011).

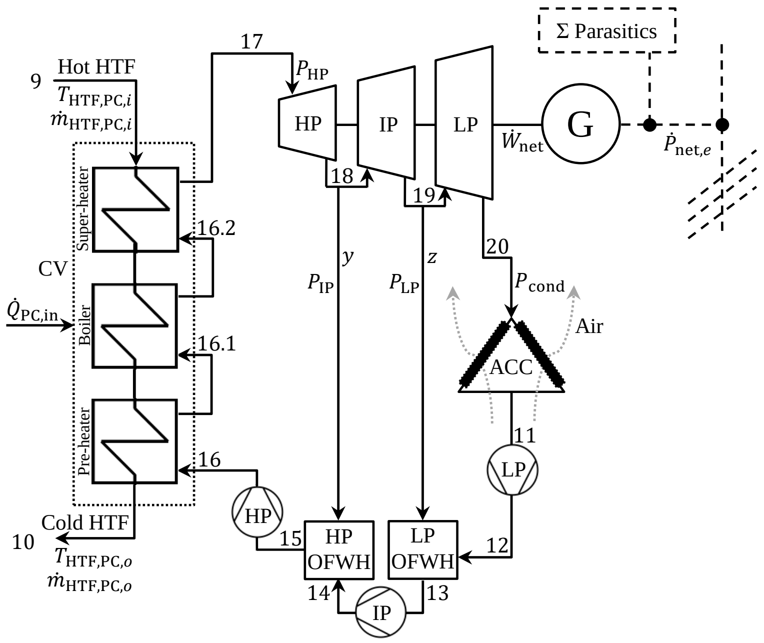

Figure 4.4: Schematic of the Rankine power cycle.

Figure 4.5 depicts the cycle on a T-s diagram. Isentropic states are indicated with s and actual states (accounting for isentropic inefficiencies) with a. Appendix B.2.1 provides additional notes on the principle of selecting a basis cycle. Appendix B.2.2 contains a detailed summary on assumptions governing the power cycle analysis. Table B.3 summarises relevant design parameters.

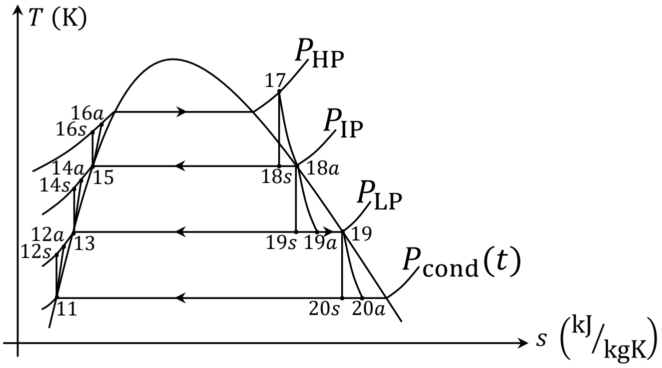

Figure 4.5: Calculated T-s diagram of the model's Rankine power cycle.

4.2.4.2 Regeneration Feedwater Components

The condenser pump is modelled in Appendix B.2.3, the LP OFWH in Appendix B.2.4, the IP pump in Appendix B.2.5, the HP OFWH in Appendix B.2.6 and the HP pump in Appendix B.2.7.

4.2.4.3 Steam Generator

The steam generator analysis is simplified with a macro CV across the pre-heater, boiler and super-heater, as shown in Figure 4.4. Its energy balance gives:

$$\dot{Q}_{\text{PC,in}} = \dot{m}_w \cdot (h_{17} - h_{16a}) = \dot{m}_{\text{PC}} \cdot \bar{c}_p \cdot (T_{\text{PC},i} - T_{\text{PC},o})\,|_{\text{HTF}} \tag{4.2.9}$$

with $\dot{Q}_{\text{PC,in}}$ the total power cycle thermal input to achieve the design enthalpy increase $h_{17}-h_{16a}$, where $h_{17} = h_{@(P_{\text{HP}},T_{17})}$ is the HP turbine superheated steam design inlet enthalpy. The working fluid mass flow rate is $\dot{m}_w$. Furthermore, $\dot{m}_{\text{HTF,PC}} = \dot{m}_{\text{HTF,PC},i} = \dot{m}_{\text{HTF,PC},o}$ is the HTF mass flow rate received from the solar field and/or TES, $T_{\text{HTF,PC},i}$ and $T_{\text{HTF,PC},o}$ the power cycle HTF inlet and outlet temperatures and $\bar{c}_{p,\text{HTF}}$ the average specific heat between those temperatures. The default design HTF mass flow rate to the steam generator is:

$$\dot{m}_{\text{HTF,PC,des}} = \dot{Q}_{\text{PC,in,des}} / [\bar{c}_{p,\text{HTF}} \cdot (T_{\text{HTF,PC},i,\text{des}} - T_{\text{HTF,PC},o,\text{des}})] \tag{4.2.10}$$

where $\dot{Q}_{\text{PC,in,des}} = \dot{W}_{\text{turb,gross,des}}/\eta_{\text{th,des}}$, with $\eta_{\text{th,des}}$ the power cycle design thermal efficiency and $\dot{W}_{\text{turb,gross,des}}$ the turbine design gross output power. The net available thermal power $\dot{Q}_{\text{PC,net,avail}}$ for conversion into mechanical power is the gross thermal power $\dot{Q}_{\text{PC,in}}$ less mandatory heat deductions (Appendix B.2.8).

4.2.4.4 Turbine

Turbine-specific assumptions and an account on the reduction in turbine isentropic efficiency with steam moisture are presented in Appendix B.2.9.1. The turbine specific stage work is:

$$w_{t\text{HP}} = \eta_{s,t} \cdot (h_{17} - h_{18s}) \tag{4.2.11}$$

$$w_{t\text{IP}} = \eta_{s,t} \cdot (h_{18a} - h_{19s}) \cdot (1 - y) \tag{4.2.12}$$

$$w_{t\text{LP}} = \eta_{s,t} \cdot (h_{19} - h_{20s}) \cdot (1 - y) \cdot (1 - z) \tag{4.2.13}$$

Design enthalpy drops across the HP and IP stages are fixed, but vary with the LP stage due to $P_{\text{cond}}(t)$, the time-dependent condenser pressure. Dynamic turbine state calculations of the working fluid are considered in Appendix B.2.9.2. The gross turbine power generated is:

$$\dot{W}_t = \dot{m}_w \cdot (w_{t\text{HP}} + w_{t\text{IP}} + w_{t\text{LP}}) \tag{4.2.14}$$

The net mechanical power generated is:

$$\dot{W}_{\text{net}} = \dot{W}_t - \dot{m}_w \cdot (w_{p\text{LP}} + w_{p\text{IP}} + w_{p\text{HP}}) \tag{4.2.15}$$

Because the generator and pump motor inefficiencies are neglected, the net mechanical power generated by the plant is the gross electrical power output (assuming ideal conversion). Hence, $\dot{P}_{\text{gross},e} = \dot{W}_{\text{net}}$. The plant's cumulative parasitics are deducted from the gross electrical output to give the net:

$$\dot{P}_{\text{net},e} = \dot{P}_{\text{gross},e} - \sum_{\text{plant}} \dot{P}_{\text{parasitics}} \tag{4.2.16}$$

Power cycle thermal efficiency is defined as:

$$\eta_{\text{th}} = \dot{W}_{\text{net}} / \dot{Q}_{\text{PC,net,avail}} \tag{4.2.17}$$

It is a direct measure of the cycle's ability to convert a given quantity of net available thermal power (thermal power after mandatory deductions are made) into net mechanical power (Figure B.4) and gross electric power thereafter.

4.2.4.5 Heat Rejection

Heat rejection incorporates a model by Wagner and Gilman (2011) for ACC's and allows $P_{\text{cond}}(t)$ to be determined. A complete description of the model, together with its operating strategy, is given in Appendix B.2.10.

4.2.4.6 Off-design Power Generation

Off-design operation of the power cycle occurs when it cannot generate power at its rated capacity. The performance model considers the following factors owing to off-design or part-load operation:

1. $\dot{Q}_{\text{PC,net,avail}} < \dot{Q}_{\text{PC,in,des}}$ due to weather transients;
2. $\dot{Q}_{\text{PC,net,avail}} < \dot{Q}_{\text{PC,in,des}}$ due to thermal energy discharged from storage;
3. $\dot{Q}_{\text{PC,net,avail}} < \dot{Q}_{\text{PC,in,des}}$ due to mandatory heat deductions.

A strategy accommodating off-design effects on power generation is presented in Appendix B.2.11.

4.2.4.7 Operating Modes

Three operating modes are considered: shutdown (zero output), startup (energy penalties) and normal operating mode ("business-as-usual"). The shutdown mode is simple in execution (Appendix B.2.12.1), but the startup mode is more involved (Appendix B.2.12.2). Normal operating mode includes any situation where power is generated by the cycle (Wagner and Gilman, 2011).

4.2.4.8 Parasitic Power Consumption

The three main power cycle parasitic consumers are: ACC fan power (see Appendix B.2.13.1), HTF pumping power (see Appendix B.2.13.2) and a fixed background parasitic (see Appendix B.2.13.3).

4.2.4.9 Control Strategy

The power cycle control strategy forms the central hub for decision-making and control execution in the plant. A summary of the control strategy can be found in Appendix B.2.14.

4.2.4.10 Performance Metrics

The plant capacity factor is:

$$CF = \sum_{t=1}^{8760} \left(\dot{P}^{t}_{\mathrm{net},e} \cdot \Delta t \right) \Bigg/ \left(Nameplate\ capacity \cdot \Delta t \cdot \sum_{t=1}^{8760} t \right) \tag{4.2.18}$$

This measures the actual net electrical energy generated as a fraction of the electrical energy generated at the nameplate capacity (maximum design generation) on an annual basis. There are 8760 hours in a typical year, t is an hourly increment and Δt an equally divided time step of 1 hour.

The gross-to-net conversion rate measures the fraction of gross electric energy not consumed by parasitics:

$$\eta_{\text{gross-to-net}} = \sum_{t=1}^{8760} \left(\dot{P}^{t}_{\mathrm{net},e} \cdot \Delta t \right) \Bigg/ \sum_{t=1}^{8760} \left(\dot{P}^{t}_{\mathrm{gross},e} \cdot \Delta t \right) \tag{4.2.19}$$

4.2.5 Thermal Energy Storage

4.2.5.1 Sizing and Initialisation

The TES model is based on the schematic in Figure 4.6, with H_{max} the maximum tank inventory height. H_{min} is a minimum required HSF pump head.

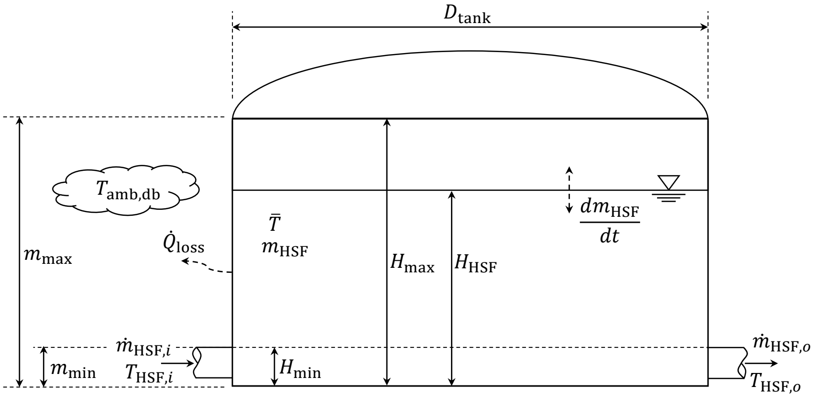

Figure 4.6: TES schematic (adapted from Wagner and Gilman, 2011).

The design TES charge capacity as a function of the storage hours at design (t_{TES}) is:

$$E_{\mathrm{TES,des}} = \dot{W}_{t,\mathrm{gross,des}} \cdot t_{\mathrm{TES}} / \eta_{\mathrm{th,des}} \tag{4.2.20}$$

The design heat storage fluid volume to attain $E_{\text{TES,des}}$ is:

$$V_{\text{TES}} = E_{\text{TES,des}}/[\overline{\rho}_{\text{HSF}} \cdot \overline{c}_{p,\text{HSF}} \cdot (T_{h,\text{des}} - T_{c,\text{des}})] \tag{4.2.21}$$

where $\overline{\rho}_{\text{HSF}}$ and $\overline{c}_{p,\text{HSF}}$ are the density and specific heat of the molten salt heat storage fluid at $0.5(T_{h,\text{des}} + T_{c,\text{des}})$, with $T_{h,\text{des}}$ and $T_{c,\text{des}}$ the design temperatures of the hot and cold tank HSF respectively. All TES design parameters are summarised in Table B.4. Sizing V_{TES} based on the average TES design temperature is deemed sufficient. The cold tank volume is equal to V_{TES}. The hot tank is slightly oversized from V_{TES} to accommodate volumetric thermal expansion of the heated HSF (Appendix B.3.2). Initially, the hot tank is assumed depleted at $H_{\min}$ and the cold tank full at $H_{\max}$ (Appendix B.3.3).

4.2.5.2 Overview of Solar Thermal Charge Cycles

Solar thermal energy sent to TES is the field thermal power output in excess of the power cycle design thermal power input, at a given time:

$$\dot{Q}_{f\rightarrow\text{TES}} = \max(\dot{Q}_{f,\text{HTF}} - \dot{Q}_{\text{PC,in,des}}, 0) \tag{4.2.22}$$

If $\dot{Q}_{f\rightarrow\text{TES}} > 0$, the power cycle receives the thermal power $\dot{Q}_{\text{PC,in}} = \dot{Q}_{\text{PC,in,des}}$. Similarly, the HTF mass flow rate sent to storage is balanced between the field HTF mass flow rate delivered and power cycle HTF mass flow rate consumed:

$$\dot{m}_{\text{HTF},f\rightarrow\text{TES}} = \dot{m}_{f,o} - \dot{m}_{\text{HTF,PC}} \tag{4.2.23}$$

Whenever $\dot{Q}_{f\rightarrow\text{TES}} > 0$, a solar thermal TES charge cycle is required. The inventory levels of the hot and cold tanks are a prerequisite for charging to take place. Since HSF is displaced from the cold to the hot tank, the following condition must always hold for a charge cycle to occur:

$$m_c > m_{\min} \;\;\&\;\; m_h < m_{\max} \tag{4.2.24}$$

where m_c and m_h are the time-varying cold and hot tank HSF inventory levels respectively. Whenever Equation 4.2.24 is violated, excess $\dot{Q}_{f\rightarrow\text{TES}} = \dot{Q}_{f,\text{disc}}$ is discarded by defocusing solar collector assemblies.

The relevant TES HTF/HSF HX inlet and outlet mass flow rates and temperatures are determined by applying conservation of mass and energy at pseudo steady-state. The TES HX, based on an approach temperature difference model, requires several iterations and control logics throughout the analysis. This ensures a temperature delta exists across the hot to cold HX sides to satisfy the second law of Thermodynamics. It adjusts the flow rates and heat transfer rate if the requirement is violated, and iterates the calculations to convergence. Its formulation is presented in Appendix B.3.4.1. After solving the HX model, the HSF inventories at the end of a time step are:

$$m_c^{t+\Delta t} = m_c^t - \dot{m}_{\text{HSF,chg}}^t \cdot \Delta t \tag{4.2.25}$$

$$m_h^{t+\Delta t} = m_h^t + \dot{m}_{\text{HSF,chg}}^t \cdot \Delta t \tag{4.2.26}$$

HSF charge and discharge mass flow rates are $\dot{m}_{\text{HSF,chg}}$ and $\dot{m}_{\text{HSF,dchg}}$.

4.2.5.3 Overview of Discharge Cycles

At a given time, a demand for TES arises whenever the power cycle input thermal power drops below its design value (usually due to weather transients or a setting sun). The thermal demand from storage is calculated as:

$$\dot{Q}_{\text{TES}\rightarrow\text{PC}} = \dot{Q}_{\text{PC,in,des}} - \dot{Q}_{f,\text{HTF}} \tag{4.2.27}$$

The default HTF mass flow rate from TES is balanced as:

$$\dot{m}_{\text{HTF,TES}\rightarrow\text{PC}} = \dot{m}_{\text{HTF,PC,des}} - \dot{m}_{f,o} \tag{4.2.28}$$

The HSF inventory requirements for discharge are:

$$m_c < m_{\max} \;\; \& \;\; m_h > m_{\min} \tag{4.2.29}$$

Whenever Equation 4.2.29 is breached, discharging ceases since the active HSF inventory is depleted. Then, $\dot{Q}_{\text{TES}\rightarrow\text{PC}} = \dot{m}_{\text{HTF,TES}\rightarrow\text{PC}} = 0$. Once again, the heat transfer rate, inlet and outlet mass flow rates and temperatures of the TES HSF/HTF HX are subject to the TES HX approach temperature difference model described in Appendix B.3.4.2. Once solved, the HSF inventories at the end of a time step are:

$$m_c^{t+\Delta t} = m_c^t + \dot{m}^t_{\text{HSF,dchg}} \cdot \Delta t \tag{4.2.30}$$

$$m_h^{t+\Delta t} = m_h^t - \dot{m}^t_{\text{HSF,dchg}} \cdot \Delta t \tag{4.2.31}$$

4.2.5.4 Average Tank Temperature

Each tank's inventory is assumed fully mixed with no thermal stratification, at a uniform average temperature $\overline{T}(t)$ (Poole, 2017). An unsteady-flow energy and mass analysis determines each tank's average HSF temperature at the end of a time step. Governing assumptions, together with the derivation in Appendix B.3.5, provide the following iterative relationship:

$$\begin{aligned}\overline{T}(t+\Delta t) = \frac{\Delta t}{mc} \cdot \Bigg\{ &\sum_{\text{in}} \dot{m} \cdot \left[h_0 + \int_{T_0}^{T_{\text{in}}} c(T)dT \right]_{\text{in}} - \sum_{\text{out}} \dot{m} \cdot \left[h_0 + \int_{T_0}^{\overline{T}(t+\Delta t)} c(T)dT \right]_{\text{out}} \\ &- \dot{Q}_{\text{loss}} + \left(\sum_{\text{out}} \dot{m} - \sum_{\text{in}} \dot{m} \right) \cdot \left[u_0 + \int_{T_0}^{\overline{T}(t+\Delta t)} c(T)dT \right] \Bigg\} + \overline{T}(t)\end{aligned} \tag{4.2.32}$$

4.2.5.5 Thermal Losses

Thermal losses are driven by each tank's surface area, average HSF temperature and the ambient dry-bulb temperature. Total losses from TES are the sum of hot and cold tank losses. A thermal loss model is formulated in Appendix B.3.6.

4.2.5.6 Charge State

The charge state is an indication of the total thermal energy stored within the hot tank at a given time:

$$E_{\text{chg}}^{t+\Delta t} = \max(E_{\text{chg}}^{t} + \dot{Q}_{f\rightarrow\text{TES}}^{t} \cdot \Delta t + \dot{P}_{H,\text{tot}}^{t} \cdot \Delta t - \dot{Q}_{\text{TES}\rightarrow\text{PC}}^{t} \cdot \Delta t - \dot{Q}_{\text{loss},h}^{t} \cdot \Delta t, 0) \tag{4.2.33}$$

where $\dot{P}_{H,\text{tot}}^{t} \cdot \Delta t$ is the heater block energy addition at time t (Section 4.2.8), being zero for a plant with no Carnot battery application. A negative charge state, brought on by continued thermal losses after storage is depleted, is not considered. Therefore, the minimum charge state is always zero. Once the hot tank HSF inventory reaches the minimum level, the charge state is set to zero since no more inventory can be withdrawn.

4.2.5.7 Parasitic Power Consumption

The main parasitics include the HTF and HSF pumps. Auxiliary heating is not considered, as neither the cold or hot tank temperatures drop below $T_{\text{HSF,min}}$ in the SAM benchmark simulation. Parasitics are modelled in Appendix B.3.7.

4.2.5.8 Performance Metrics

The thermal energy discharge-to-charge ratio measures the conversion efficiency of stored thermal energy into discharged thermal energy, on an annual basis. It is estimated as:

$$\eta_{\text{dchg-chg}} = \sum_{t=1}^{8760} \left(\dot{Q}_{\text{TES}\rightarrow\text{PC}}^{t} \cdot \Delta t\right) \Bigg/ \sum_{t=1}^{8760} \left(\dot{Q}_{f\rightarrow\text{TES}}^{t} \cdot \Delta t + \dot{P}_{H,\text{tot}}^{t} \cdot \Delta t\right) \tag{4.2.34}$$

The TES round-trip efficiency is estimated as:

$$\eta_{\text{round}} = \sum_{t=1}^{8760} \left(\dot{P}_{\text{TES,PC,net},e}^{t} \cdot \Delta t\right) \Bigg/ \sum_{t=1}^{8760} \left(\dot{Q}_{f\rightarrow\text{TES}}^{t} \cdot \Delta t + \dot{P}_{H,\text{tot}}^{t} \cdot \Delta t\right) \tag{4.2.35}$$

It estimates the conversion efficiency of stored thermal energy into net electrical energy on an annual basis. The numerator is the net electrical energy generated from TES (Equation 4.2.56) and the denominator is the total energy sent to TES (solar thermal and imported RE as a Carnot battery).

An important contribution of TES, especially for $SM > 1$, is its ability to maintain a solar thermal energy utilisation of ideally 100 %. The utilisation factor, UF, is expressed as (Stine and Geyer, 2001):

$$UF = 1 - \left[\left(\sum_{t=1}^{8760} \dot{Q}_{f,\text{disc}}^{t} \cdot \Delta t\right) \Bigg/ \left(\sum_{t=1}^{8760} \dot{Q}_{f,\text{HTF,net,abs}}^{t} \cdot \Delta t\right)\right] \tag{4.2.36}$$

A maximum UF of 100 % is achieved when the TES and solar field is sized such that the annual collected field thermal energy is properly utilised by the TES and the power cycle. This results in zero curtailed or discarded solar thermal energy. However, for a fixed nameplate capacity, the maximum attainable UF eventually decreases below 100 % as SM is increased beyond 1. This occurs regardless of larger TES capacities. The onset of this occurrence is termed the maximum displacement point in Stine and Geyer (2001).

4.2.6 Economic Model

4.2.6.1 Levelised Cost of Electricity

The LCOE represents the constant per-unit cost at which electricity must be generated by a plant in order to break even with upfront and lifetime project costs incurred (Lovegrove and Stein, 2012; Madaly, 2014; Fourie, 2018). As noted in Fourie (2018), it is a widely accepted metric to rank economic competitiveness of various power generation technologies. The fixed charge rate (FCR) method is a simplified model used to calculate the LCOE (Short *et al.*, 1995; Lovegrove and Stein, 2012; Gilman, 2020). It is appropriate for early stages in a project feasibility study, as in Riffelmann *et al.* (2020); Gedle *et al.* (2020), and provides an alternative to SAM's more detailed and time-dependent cash flow orientated single-owner financial models (NREL, 2020*b*). The fixed charge rate method gives the LCOE as:

$$LCOE_{\mathrm{FCR}} = (FCR \cdot TIC + FOC + VOC)/AEP \tag{4.2.37}$$

with AEP the net annual electrical energy production, FOC the fixed per-nameplate capacity O&M (operational and maintenance) cost:

$$FOC = C_{\mathrm{FOC}} \cdot Nameplate\ capacity \tag{4.2.38}$$

and VOC the variable O&M cost, also accounting for RE charging costs, C_{RE}, once applied as a Carnot battery (C_{RE} is zero otherwise):

$$VOC = C_{\mathrm{VOC}} \cdot AEP + \sum_{t=1}^{8760} C_{\mathrm{RE}}(t) \tag{4.2.39}$$

The O&M cost parameters are detailed in Appendix B.4.1.3. Equation 4.2.37 is only valid under the assumptions of fixed annual electrical energy production and annual O&M costs (Short *et al.*, 1995).

The fixed charge rate is the annual revenue per dollar of investment required to support the investment (Short *et al.*, 1995; NREL, 2020*b*). NREL (2020*b*) provides the following relation for the fixed charge rate:

$$FCR = CRF \cdot PFF \cdot CFF \tag{4.2.40}$$

where CRF is a capital recovery factor, PFF a project financing factor and CFF a construction financing factor.[8] Appendix B.4.2 summarises these parameters as given in the SAM benchmark model. The calculations are based on d_{real}, the real discount rate[9], assumed as 8.2 %/year (Fourie, 2018; Department of Energy, 2019). This corresponds to a nominal discount rate of $d_{\text{nom}} = 13.07$ %/year when accounting for inflation, r_{infl}, according to the formula:

$$d_{\text{real}} = (d_{\text{nom}} - r_{\text{infl}})/(1 + r_{\text{infl}}) \tag{4.2.41}$$

given by Correia *et al.* (2015); Pan (2020). An inflation rate of $r_{\text{infl}} = 4.5$ %/year is assumed.[10]

The total installed cost (TIC) is:

$$TIC = TDCC + TICC \tag{4.2.42}$$

The total direct capital cost (TDCC) is calculated as (also see Appendix B.4.1.1):

$$\begin{gathered} TDCC = [(C_{\text{Site improvements}} + C_{\text{Solar field}} + C_{\text{HTF system}}) \cdot A_{\text{aperture,refl}} + \\ C_{\text{TES}} \cdot E_{\text{TES,des}} + (C_{\text{Power plant}} + C_{\text{Balance of plant}}) \cdot \dot{W}_{t,\text{gross,des}} + TDCC_H] \cdot \\ (1 + Contingency) \end{gathered} \tag{4.2.43}$$

where $A_{\text{aperture,refl}}$ is the total solar field aperture reflective area at the SM and TDCC$_H$ the total direct capital cost of the heater installation (introduced in Section 4.2.8.2), which is zero for no Carnot battery application. The total indirect capital cost (TICC) is calculated as (also see Appendix B.4.1.2):

$$TICC = EPC\ \&\ Owner\ costs + Total\ land\ cost + Sales\ tax \tag{4.2.44}$$

where EPC denotes engineer-procure-construct.

Then, to readily produce a final and more representative LCOE, LCOE$_{\text{FCR}}$ is calibrated against SAM's real LCOE.[11] Two claims are stated regarding the resulting correlation and its applicability: it is linear (essentially through the origin) and independent of the plant technical parameter at change, as supported by Figure 4.7.

---

[8] Refer to NREL (2020*b*) for further background on the calculation of CRF, PFF and CFF.

[9] According to the Department of Energy: Republic of South Africa (2010), real discount rates for power sector planning should vary between 7 % to 10 %.

[10] South Africa's target inflation rate is 3 % to 6 % (Trading Economics, 2020), of which the average is used in this thesis.

[11] SAM's real LCOE accounts for after-tax costs, insurance rates, debt options, construction financing costs and reserve account funding, among other parameters (Gilman, 2020). The fixed charge rate LCOE is a swift model appropriate for simple investment structures (Short *et al.*, 1995). Real LCOE's, inherently based on more complex cash flow calculations, are typically preferred for long-term projections (Lovegrove and Stein, 2012).

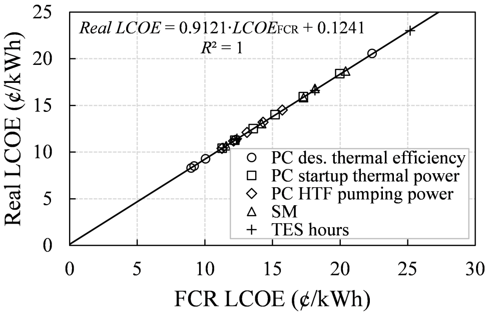

Figure 4.7: Real LCOE and FCR LCOE calibration.

The linear relationship stems from the respective LCOE$_{\text{FCR}}$ and real LCOE equations. SAM's real LCOE is given as (Gilman, 2020; NREL, 2020*b*):

$$LCOE_{\text{real}} = \left[-C_0 - \sum_{i=1}^{N} C_i/(1+d_{\text{real}})^i \right] \Big/ \left[\sum_{i=1}^{N} AEP_i/(1+d_{\text{real}})^i \right] \quad (4.2.45)$$

with $i \in [1, N]$ the i'th operational year in the plant's lifetime N and C_0 the initial investment amount. The numerator represents the net present value (NPV) of the project lifetime costs.[12] Since zero degradation in AEP is assumed, $AEP_i = AEP$. As such, AEP can be factorised out of the summation as a constant value. To find $LCOE_{\text{real}} = f(LCOE_{\text{FCR}})$, Equation 4.2.37 is solved for AEP, substituted into Equation 4.2.45 and simplified to give:

$$LCOE_{\text{real}} = LCOE_{\text{FCR}} \cdot \frac{\text{NPV}(Project\ lifetime\ costs)}{(FCR \cdot TIC + FOC + VOC) \cdot \sum_{i=1}^{N} (1+d_{\text{real}})^{-i}} \quad (4.2.46)$$

Equation 4.2.46's fraction should correspond to the gradient in Figure 4.7. To test this theory, each plant parameter in Figure 4.7 is perturbed to half, double and triple its design value in SAM, with the fraction in Equation 4.2.46 computed from corresponding outputs. From the samples an average gradient of 0.916 (standard deviation = 0.003) with an error of 0.43 % relative to Figure 4.7's gradient is found. This is deemed acceptable and the correlation in Figure 4.7 is recognised as a reliable conversion.

4.2.6.2 Power Purchase Agreement Price

The real PPA price (PPA price hereon) is the minimum price at which the power producer should agree to sell electricity in a power purchase agreement

---

[12] In NREL (2020*b*); Gilman (2020) the annual project cost C_i is discounted nominally as it is inflation-adjusted in SAM (NREL, 2020*b*). Shown here is the more general case where it is not inflation-adjusted, and thus discounted at the real discount rate to return a real price. Furthermore, negative signs are assumed to indicate cash outflows. However, only cash flow magnitude and not "direction" is considered in this derivation.

(PPA) in order to reach it's target internal rate of return (IRR) (Wagner, 2017*a*). The plant sells electricity at a rate determined from the PPA price and a set of TOD factors (NREL, 2020*b*), of which this thesis only considers uniform TOD. Similar to Section 4.2.6.1, the PPA price is determined from LCOE_{FCR} with the correlation in Figure 4.8.

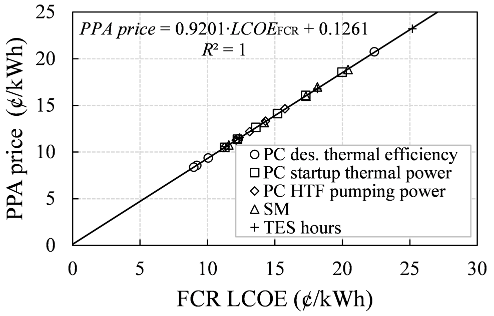

Figure 4.8: PPA price and FCR LCOE calibration.

The observation in Figure 4.8 should also be supported by theory. The PPA price is mathematically defined as (NREL, 2020*b*):

$$PPA\ price = \sum_{i=1}^{N} R_i/(1+d_{\text{real}})^i \Bigg/ \sum_{i=1}^{N} AEP_i/(1+d_{\text{real}})^i \qquad (4.2.47)$$

The numerator's summation reflects the net present value of the project lifetime PPA revenue.[13] Again, $AEP_i = AEP$. As a constant value, it is factorised out of the summation. $PPA\ price = f(LCOE_{\text{FCR}})$ is found by substituting Equation 4.2.37, solved for AEP, into Equation 4.2.47 and simplifying:

$$PPA\ price = LCOE_{\text{FCR}} \cdot \frac{\text{NPV}(Project\ lifetime\ PPA\ revenue)}{(FCR \cdot TIC + FOC + VOC) \cdot \sum_{i=1}^{N}(1+d_{\text{real}})^{-i}} \qquad (4.2.48)$$

It follows that the PPA price is also linear in LCOE_{FCR}. The fraction in Equation 4.2.48 should therefore represent the gradient in Figure 4.8. The experiment of Section 4.2.6.1 is repeated for this case, resulting in an average gradient of 0.925 (standard deviation = 0.004) with an error of 0.53 % relative to Figure 4.8's gradient. This error is deemed acceptable and the correlation in Figure 4.8 is recognised as a reliable conversion from LCOE_{FCR} to PPA price, subject to the governing assumptions. A linear relationship is consequently also observed between $\text{LCOE}_{\text{real}}$ and PPA price, regardless of the TOD remuneration structure. However, the TOD structure does influence the bid price

---

[13] In NREL (2020*b*) the annual PPA revenue R_i is discounted nominally as it is inflation-adjusted in SAM (NREL, 2020*b*). Here the general, non-adjusted form is shown, thus discounted at the real discount rate to return a real tariff.

in a nonlinear fashion (Section 4.2.6.4).

Concluding, the calibrations in Figures 4.7 and 4.8 are independent of the plant technical parameter at change, as it derives from Equation 4.2.37 that only recognises changes in costs and electricity generation. For this reason it is also appropriate to analyse the plant applied as a Carnot battery. It adequately converts Equation 4.2.37, a simple and swift computation, into the real LCOE and PPA price provided by SAM's more detailed and involved single-owner cash flow models. These attributes are computationally advantageous. The calibrations, supported by the underlying theory, are only valid for fixed financial inputs to the economic model. In this thesis, these are: a plant design life of 25 years, inflation rate of $r_{\text{infl}} = 4.5$ %/year, nominal discount rate of 13.07 %/year, IRR target of 11 %, IRR target year of 20 and a PPA price escalation of 4.5 %/year[14]. Furthermore, fixed AEP and annual variable costs are required.

4.2.6.3 Levelised Profit of Electricity

Figure 4.8's PPA price establishes the minimum cost at which electricity should sell in order to meet the investment target. This can define the (real) levelised profit of electricity (LPOE, ¢/kWh) as a measure of profitability (Poole, 2017):

$$LPOE = PPA\ price - LCOE \tag{4.2.49}$$

Note that the objective is not to maximise LPOE by, say, increasing the IRR. $LPOE > 0$ is regarded as the minimum requirement for a profitable and therefore feasible project.

4.2.6.4 Bid Price

The bid price is the price at which an entity is prepared to buy a commodity (Hayes, 2021). Here the entity represents the power utility and electricity the commodity. The year one PPA price is equivalent to the bid price in a PPA (NREL, 2020*b*). This simply equates to:

$$Bid\ price = (1 + r_{\text{PPA,esc}})^{i=1} \cdot PPA\ price \tag{4.2.50}$$

with $r_{\text{PPA,esc}}$ the PPA price escalation rate used to determine the starting tariff in year one (bid price). As observed in SAM, non-uniform TOD can yield instances requiring a smaller or larger bid price to meet the same investment target. The bid price is influenced by the external nonlinear TOD profile and as a result, the relationship and technical parameter independence between real LCOE and bid price is less predictable and nonlinear. This thesis does not consider non-uniform TOD and its practical applications in, for example, dispatch optimisation.

---

[14] PPA price escalation is assumed on par with the inflation rate (Pan, 2020).

4.2.6.5 Levelised Cost of Storage

The levelised cost of storage (LCOS) ranks the economic feasibility of various competing electricity storage technologies (Fourie, 2018; Schmidt *et al.*, 2019). Analogous to LCOE, it represents the discounted cost per unit of electricity generated from discharged stored energy, across the storage system's lifetime (Schmidt *et al.*, 2019). A simplified version of the more detailed LCOS relation given in Larsson and Börjesson (2018); Schmidt *et al.* (2019) is implemented:

$$LCOS = \left[C_{\text{investment}} + \sum_{i=1}^{N} \frac{Battery\ VOC}{(1+d_{\text{real}})^i} \right] \Big/ \sum_{i=1}^{N} \frac{\sum_{t=1}^{8760} \dot{P}_{\text{TES,PC,net},e}(t) \cdot \Delta t}{(1+d_{\text{real}})^i} \tag{4.2.51}$$

End-of-life (EOL) costs, annual degradation and residual value are unknown and neglected.[15] Furthermore:

$$\begin{aligned} C_{\text{investment}} &= (1 + Contingency) \cdot (1 + EPC\ \&\ Owner) \cdot [C_{\text{TES}} \cdot \\ E_{\text{TES,des}} &+ (C_{\text{Power plant}} + C_{\text{Balance of plant}}) \cdot Nameplate\ capacity + TDCC_H] \end{aligned} \tag{4.2.52}$$

is the investment cost incurred in year zero and:

$$Battery\ VOC = \sum_{t=1}^{8760} C_{\text{RE}}(t) + O\&M_{\text{TES}} + O\&M_{\text{PC}} \tag{4.2.53}$$

the Carnot battery-specific variable O&M cost, where:

$$\begin{aligned} O\&M_{\text{TES}} = f_{\text{O\&M,TES}} \cdot (1 + Contingency) \cdot (1 + EPC\ \&\ Owner) \cdot \\ (C_{\text{TES}} \cdot E_{\text{TES,des}} + TDCC_H) \end{aligned} \tag{4.2.54}$$

and:

$$O\&M_{\text{PC}} = C_{\text{VOC}} \cdot \sum_{t=1}^{8760} \dot{P}_{\text{TES,PC,net},e}(t) \cdot \Delta t + C_{\text{FOC}} \cdot Nameplate\ capacity \tag{4.2.55}$$

$C_{\text{RE}}(t)$ is the hourly variable cost of charging RE (Section 4.2.8.2), equal to zero for no Carnot battery application, and d_{real} is also assumed as 8.2 %/year. O&M$_{\text{TES}}$ represents O&M costs specific to the TES subsystem, and is estimated at $f_{\text{O\&M,TES}} = 2$ % of the TES investment cost per year (Fourie, 2018). Here, the TES investment cost is assumed to include TDCC$_H$, the heater block total direct capital cost (Section 4.2.8.2). O&M$_{\text{TES}}$ is exclusively used in estimating the LCOS and not the LCOE (the LCOE does account for O&M costs

---

[15] EOL costs are often neglected (Schmidt *et al.*, 2019). Residual value is difficult to assume in general (Larsson and Börjesson, 2018). TES experiences very little cycling-induced degradation, with superior lifetime and cycle life compared to battery energy storage technologies (Alva *et al.*, 2018).

based on the plant's generation and capacity-level and not on a subsystem level).

Any unknown costs are assumed to be accounted for by including contingency and EPC & Owner cost factors. It is emphasised that in Equation 4.2.55, C_{VOC} only considers the electricity generated from stored energy, whereas C_{FOC} considers the entire nameplate capacity of the power block. Annual battery O&M costs, in conjunction with Megaflex time-of-use (TOU) charges in Equation 4.2.53, are fixed and escalate annually with inflation (Fourie, 2018)[16]. They are therefore discounted via the real discount rate.

$\dot{P}_{\text{TES,PC,net},e}(t)$ is the stored thermal energy converted into net positive electrical energy within the power cycle, exempt from annual degradation. It is estimated as:

$$\dot{P}_{\text{TES,PC,net},e}(t) = \max\left\{ \left[\dot{Q}_{\text{TES}\rightarrow\text{PC}}(t) - \dot{Q}_{\text{PC,su}}(t) - \dot{Q}_{\text{PC,bd}}(t)\right] \cdot \eta_{\text{th}}(t) - \sum_{\text{plant}} \dot{P}_{\text{parasitics}}(t), 0 \right\} \tag{4.2.56}$$

with $\dot{Q}_{\text{PC,su}}$ and $\dot{Q}_{\text{PC,bd}}$ power cycle startup and blowdown heat deductions (Appendix B.2.8). Therefore, only parasitics active during the conversion of stored thermal energy into electricity are deducted in Equation 4.2.56.

4.2.7 Performance Model against SAM Benchmark

Main output metrics of the conventional parabolic trough plant performance model at design are presented and compared to the SAM benchmark model in Table 4.2.

Table 4.2: Performance model vs. SAM benchmark model metrics at design.

Metric	Unit	Perf. model	SAM	% Diff.
CF	%	43.54	43.5	0.09
TES discharge-to-charge ratio †	%	96.57	97.23	−0.68
UF †	%	84.36	84.07	0.34
Gross-to-net conversion	%	91.63	89.7	2.15
LCOE	¢/kWh	10.43	10.47	−0.38
PPA price, year 1 (bid price)	¢/kWh	11.00	11.04	−0.36
LCOS †	¢/kWh	35.75	38.36	−6.8

---

[16] Future Megaflex tariff escalation rates are inherently uncertain (Fourie, 2018). Historic Megaflex tariff increases include: 2017-2018 - 2.4 %, 2018-2019 - 6 %, 2020-2021 - 8.94 % and, more recently, 2021-2022 - 15.06 % (Eskom, 2021*b*,*c*). According to Fourie (2018), annual tariff escalation could drop to 5 %, eventually located within the national target inflation range, after a period of above-inflation escalation.

Refer to Appendix C.1-C.3 for an extended validation analysis. Metrics with superscript † are not directly reported outputs in SAM and are post-calculated from SAM simulation results instead. "% Diff." calculates the relative difference between results as per Equation C.2.1. A fair accordance can be observed between the main metrics of the performance model and the SAM benchmark model at design.

In addition to Table 4.2, an off-design validation is conducted (Appendix C.3) where each metric is validated at the combination of three different SM's and TES hours (i.e. nine unique data points per metric). The average of the absolute (to avoid error cancellation) relative differences per metric is: CF: 1.68 %, UF: 1.41 %, gross-to-net conversion: 2.43 %, TES discharge-to-charge ratio: 0.4 %, LCOE: 1.52 %, bid price: 1.52 % and LCOS: 4.76 %. Due to the relatively "expensive" numerator of the LCOS, it is quite sensitive to changes in electricity generated from TES.

The difference in modelling approaches between SAM and this thesis's performance model will likely yield somewhat different, yet comparable results. Unfortunately, SAM does not provide the LCOS as an output financial metric, nor does it provide all the detailed output parameters required to exactly match the LCOS calculation as described in Section 4.2.6.5. "SAM's LCOS" can therefore be estimated at best.

For example, in Appendix B.2.11 a deviation from power cycle design thermal input penalises the turbine isentropic efficiency. This adversely affects the electrical power generated, especially from TES only, which has a more pronounced effect on the LCOS than on other economic metrics. In SAM it is not evident whether a similar power cycle penalty is implemented, which introduces some uncertainty in comparing results. Nonetheless, the values are within range of one another. Similar magnitudes of validation differences are also encountered in other studies: Madaly (2014); Auret (2015); Barnes (2017); Scolan *et al.* (2020); Pan (2020). With the validation results deemed satisfactory, the parabolic trough CSP plant can be applied as a Carnot battery (Section 4.2.8).

4.2.8 Carnot Battery Application Model

The Carnot battery application entails a comparatively small addition to the parabolic trough plant's TES block, as seen in Figure 4.1. This section details technicalities of the application and concludes the techno-economic modelling of the preceding sections.

4.2.8.1 Technical Considerations

The TES block is equipped with a heater block, as outlined in Figure 4.1, of which the detailed CV is given in Figure 4.9.

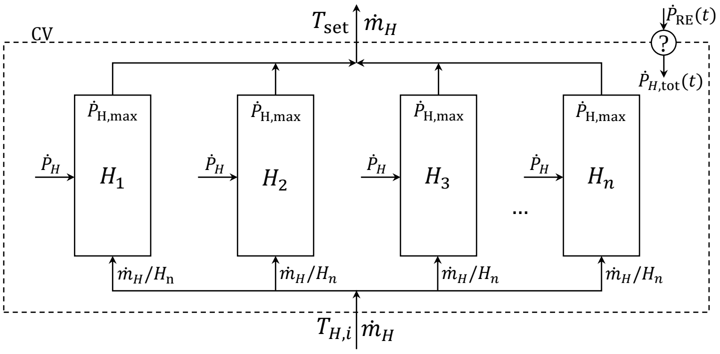

Figure 4.9: Heater block control volume.

HSF is drawn from hot storage and enters the heater block at a temperature $T_{H,i} = \overline{T}_h$ and mass flow rate $\dot{m}_H$. The block contains a maximum of $H_n = \{x \in \mathbb{Z} | x \geqslant 0\}$ heaters, each with a rated maximum capacity of $\dot{P}_{H,\max}$, where $\dot{P}_H \in [0, \dot{P}_{H,\max}]$ is the range of electric power drawn per heater. A total quantity of $\dot{P}_{\mathrm{RE}}(t)$ renewable electricity (Figure 4.10) is available to the heater block, whereas $\dot{P}_{H,\mathrm{tot}}(t)$ is the actual power drawn by the block.

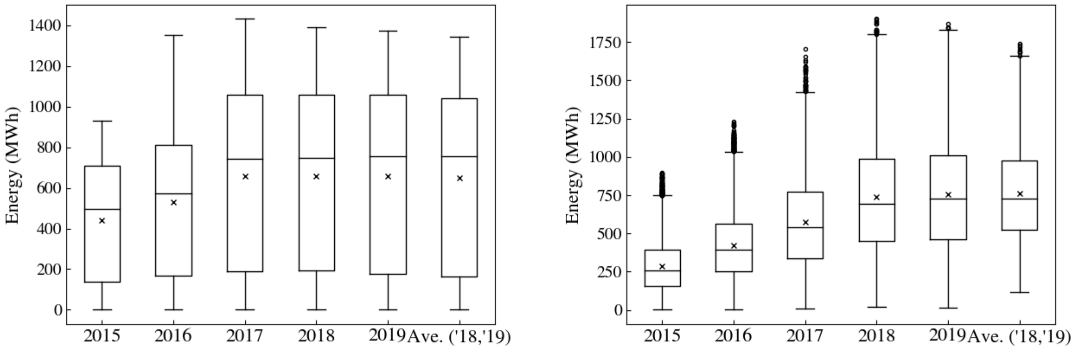

(a) Solar PV energy.

(b) Onshore wind energy.

Figure 4.10: National RE statistics for 2015-2019.

The national renewable electricity (this thesis only considers solar PV and onshore wind energy) can be obtained from Eskom (2021a) as hourly data. This data is from generators owned by Eskom, or that Eskom has contracts with. Embedded renewable generation is therefore not considered. It is important to average the hourly variability in annual supply, while staying true to the most up-to-date installed capacity of each source. For this reason, hourly datasets for 2018-2019 (where installed capacity remains largely constant for both) are averaged into a single set that is regarded representative of a typical "current" year for the South African grid. Descriptive statistics for years 2015-2019's national solar PV and wind energy is given in Figure 4.10. Hourly data from the rightmost average sets are used to define $\dot{P}_{\text{RE}}(t)$.

The maximum heater block power consumption is always restricted to $\dot{P}_{H,\text{tot}} = \min[\dot{P}_{H,\max} \cdot H_n, \dot{P}_{\text{RE}}]$, from which the default $\dot{m}_H$ is calculated as:

$$\dot{m}_H = \dot{P}_{H,\text{tot}}/[\bar{c}_{p,\text{HSF}} \cdot (T_{\text{set}} - T_{H,i})] \tag{4.2.57}$$

where $\dot{P}_{H,\text{tot}} = \dot{Q}$, $\dot{m}_H$ is evenly distributed per heater, T_{set} is a fixed set point temperature at the heater block outlet and $\bar{c}_{p,\text{HSF}}$ is the average[17] HSF specific heat between $T_{H,i}$ and T_{set}. All heaters actively consume power according to $\dot{P}_H = \dot{P}_{H,\text{tot}}/H_n$.

The system checks whether $\dot{m}_H$ can be drawn from TES without depleting the hot tank below its minimum inventory requirement during Δt:

$$\text{If } \dot{m}_H > (m_h - m_{\min})/\Delta t, \text{ then } \dot{m}_H = (m_h - m_{\min})/\Delta t \tag{4.2.58}$$

If Equation 4.2.58 executes, the heater block power consumption is lowered to:

$$\dot{P}_{H,\text{tot}} = \dot{m}_H \cdot \bar{c}_{p,\text{HSF}} \cdot (T_{\text{set}} - T_{H,i}) \tag{4.2.59}$$

at the restricted $\dot{m}_H$. The energy $\dot{P}_{H,\text{tot}} \cdot \Delta t$ increases the TES charge state in Equation 4.2.33.

The TES uses Hitec solar salt as HSF. According to Heller (2013); NREL (2020*b*), Hitec solar salt has an upper temperature limit of 593 °C. Similar to reducing long-term thermal degradation of the HTF, the practical maximum T_{set} is selected 7 °C below 593 °C, therefore limited to 586 °C. A HSF stream at $\dot{m}_H$ and T_{set} is returned to the hot tank. During this process, the hot tank's average HSF temperature is updated according to Equation 4.2.32.

In summary, there are three criteria that ceases (criteria 1-2) and restricts (criterion 3) RE charging:

1. The hot tank's average temperature reaches 565 °C, the upper limit for acceptable corrosion rates of stainless steel at that temperature (Heller, 2013);
2. The hot tank's average temperature reaches T_{set};
3. Equation 4.2.58 applies. A reduced $\dot{P}_{H,\text{tot}}$ is then calculated from Equation 4.2.59 at the restricted $\dot{m}_H$.

Similar to its implementation in Appendix B.3.7, a coefficient is used to calculate the pumping power parasitic for the HSF through the heater block:

$$\dot{P}_{H,\text{HSF}} = \dot{m}_H \cdot p_{H,\text{HSF}} \tag{4.2.60}$$

---

[17] Since $c_{p,\text{HSF}}(T)$ for the molten salt varies linearly with T, $\bar{c}_{p,\text{HSF}}$ is calculated at the arithmetic mean temperature.

where $p_{H,\mathrm{HSF}}$ is also chosen as 0.173 kJ/kg. The parasitic $\dot{P}_{H,\mathrm{HSF}}$ contributes to the cumulative parasitics of the plant.

For the heaters under consideration, $\dot{P}_{H,\max}$ is given as 5 MW and the maximum T_{set} is 800 °C (EXHEAT, 2021). The total installed heater capacity becomes:

$$H_{\mathrm{cap}} = P_{H,\max} \cdot H_n \tag{4.2.61}$$

The temperature distribution and flow inside the heater is not considered, but related research can be found in Mahdi *et al.* (2020). Lastly, since SAM cannot facilitate a CSP Carnot battery application for validation purposes, the Carnot battery model is validated internally in Appendix C.4.

4.2.8.2 Economic Considerations

Capital Costs

The cost breakdown for a single representative electric process heater for high temperature applications is given in Table B.6. The total cost of a single heater installation, C_H, is ≈ 0.18 % of the benchmark plant's total installed cost at design. The total direct capital cost of the heater block is:

$$TDCC_H = H_n \cdot C_H \tag{4.2.62}$$

TDCC_H is added to the right-hand sides of Equations 4.2.43, 4.2.52 and 4.2.54. This level of analysis does not identify additional, more detailed costs associated with the application. Such costs can, for example, be associated with inlet and outlet piping to the heater block, flow control valves and maintenance. As outlined in Appendices B.4.1.1 and B.4.1.2, all unknown costs at this stage are grouped together via contingency and EPC & Owner cost factors.

When boosting the hot HSF to temperatures $\geqslant 400$ °C, the hot storage tank should not be constructed from carbon steel, but stainless steel (Kuravi *et al.*, 2013). Thus, a TES capital cost amplification occurs whenever $T_{\mathrm{set}} \geqslant 400$ °C:

$$C_{\mathrm{TES}}|_{T_{\mathrm{set}} \geqslant 400\ ^{\circ}\mathrm{C}} = C_{\mathrm{TES}} + \Delta C_{\mathrm{TES}} \tag{4.2.63}$$

with C_{TES} the TES capital cost in a conventional ($\overline{T}_h < 400$ °C) plant (Table B.5) and ΔC_{TES} an indirect TES cost-delta between a carbon steel and stainless steel hot tank (estimated in Appendix B.4.1.1 as 12.09 \$/kWht).

Variable Costs

Importing electricity from the grid for storage comes at a certain charging cost. This cost is variable since it depends on both the electricity allocated to the heaters at a given time t, as well as the adopted tariff structure. Considering that electricity (albeit renewable) is drawn from the grid, an Eskom network asset, it is assumed that the Megaflex tariffs establish the cost of electricity purchased for storage.

The Megaflex tariffs apply to most industrial consumers supplied by Eskom (Mahony and Baartman, 2018; McKechnie, 2021). This tariff structure represents on and off-peak periods for high and low-demand seasons on the South African grid. It can be used to calculate a set of time-of-use factors for purchasing electricity during a certain period. In low-demand season, the morning and evening peaks occur from 7-10 AM and 6-8 PM respectively. In comparison, high-demand season morning and evening peaks occur from 6-9 AM and 5-7 PM. It is emphasised that TOD refers to periods during which the plant generates electricity from storage, whereas TOU refers to RE charge (import) periods. The sources Eskom (2019) and Eskom (2020) are used to define an hourly TOU tariff structure (Figure 4.11).

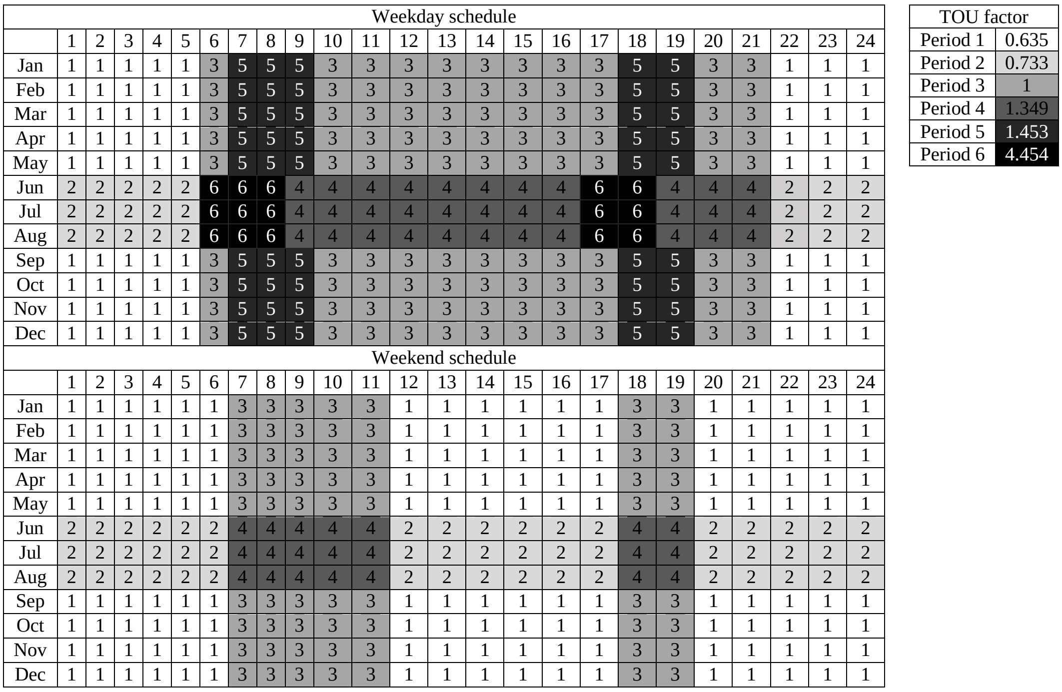

Weekday schedule

	1	2	3	4	5	6	7	8	9	10	11	12	13	14	15	16	17	18	19	20	21	22	23	24
Jan	1	1	1	1	1	3	5	5	5	3	3	3	3	3	3	3	3	5	5	3	3	1	1	1
Feb	1	1	1	1	1	3	5	5	5	3	3	3	3	3	3	3	3	5	5	3	3	1	1	1
Mar	1	1	1	1	1	3	5	5	5	3	3	3	3	3	3	3	3	5	5	3	3	1	1	1
Apr	1	1	1	1	1	3	5	5	5	3	3	3	3	3	3	3	3	5	5	3	3	1	1	1
May	1	1	1	1	1	3	5	5	5	3	3	3	3	3	3	3	3	5	5	3	3	1	1	1
Jun	2	2	2	2	2	6	6	6	4	4	4	4	4	4	4	4	6	6	4	4	4	2	2	2
Jul	2	2	2	2	2	6	6	6	4	4	4	4	4	4	4	4	6	6	4	4	4	2	2	2
Aug	2	2	2	2	2	6	6	6	4	4	4	4	4	4	4	4	6	6	4	4	4	2	2	2
Sep	1	1	1	1	1	3	5	5	5	3	3	3	3	3	3	3	3	5	5	3	3	1	1	1
Oct	1	1	1	1	1	3	5	5	5	3	3	3	3	3	3	3	3	5	5	3	3	1	1	1
Nov	1	1	1	1	1	3	5	5	5	3	3	3	3	3	3	3	3	5	5	3	3	1	1	1
Dec	1	1	1	1	1	3	5	5	5	3	3	3	3	3	3	3	3	5	5	3	3	1	1	1

Weekend schedule

	1	2	3	4	5	6	7	8	9	10	11	12	13	14	15	16	17	18	19	20	21	22	23	24
Jan	1	1	1	1	1	1	3	3	3	3	3	1	1	1	1	1	1	3	3	1	1	1	1	1
Feb	1	1	1	1	1	1	3	3	3	3	3	1	1	1	1	1	1	3	3	1	1	1	1	1
Mar	1	1	1	1	1	1	3	3	3	3	3	1	1	1	1	1	1	3	3	1	1	1	1	1
Apr	1	1	1	1	1	1	3	3	3	3	3	1	1	1	1	1	1	3	3	1	1	1	1	1
May	1	1	1	1	1	1	3	3	3	3	3	1	1	1	1	1	1	3	3	1	1	1	1	1
Jun	2	2	2	2	2	2	4	4	4	4	4	2	2	2	2	2	2	4	4	2	2	2	2	2
Jul	2	2	2	2	2	2	4	4	4	4	4	2	2	2	2	2	2	4	4	2	2	2	2	2
Aug	2	2	2	2	2	2	4	4	4	4	4	2	2	2	2	2	2	4	4	2	2	2	2	2
Sep	1	1	1	1	1	1	3	3	3	3	3	1	1	1	1	1	1	3	3	1	1	1	1	1
Oct	1	1	1	1	1	1	3	3	3	3	3	1	1	1	1	1	1	3	3	1	1	1	1	1
Nov	1	1	1	1	1	1	3	3	3	3	3	1	1	1	1	1	1	3	3	1	1	1	1	1
Dec	1	1	1	1	1	1	3	3	3	3	3	1	1	1	1	1	1	3	3	1	1	1	1	1

TOU factor	
Period 1	0.635
Period 2	0.733
Period 3	1
Period 4	1.349
Period 5	1.453
Period 6	4.454

Figure 4.11: Hourly time-of-use tariff structure.

The schedule is based on a 600 km to 900 km transmission connected zone to encompass most RE plants across South Africa. The weekend schedule is based on a Saturday. All charges are normalised around the low-demand season standard tariff of 58.39 c/kWh (VAT inclusive). Downstream distribution and transmission network charges for generators (Eskom, 2020) are not considered.

The hourly cost (¢/kWh) of purchasing RE[18] from the grid is calculated as:

$$C_{\mathrm{RE}}(t) = (1 + Contingency) \cdot 58.39 \cdot ZAR \rightarrow USD\ rate \cdot TOU(t) \cdot E_{\mathrm{RE}}(t) \tag{4.2.64}$$

---

[18] Referred to as charging costs in Larsson and Börjesson (2018); Schmidt *et al.* (2019).

where $E_{\mathrm{RE}}(t) = \dot{P}_{H,\mathrm{tot}}(t) \cdot \Delta t$ (kWh) is the hourly energy purchased. $\sum_{t=1}^{8760} C_{\mathrm{RE}}(t)$ is the annual variable charging cost added to the right-hand sides of Equations 4.2.39 and 4.2.53. The contingency factor is also included in Equation 4.2.64 to acknowledge potential upstream charging costs in addition to the TOU energy charge. The economic model is developed with ZAR conditions (Pan, 2020), but computations involving monetary variables are consistently done in the units of USD ($, 15 December 2020 ZAR-to-USD exchange rate). The exchange rate unfortunately introduces uncertainty in future projections.

4.2.8.3 Governing Assumptions

The following additional assumptions conclude the Carnot battery plant:

1. Thermal losses in the heater block are negligible;
2. The costs outlined in Table B.6 are for budgetary purposes only. They are not exact;
3. Sufficient land area is available for the installation of the heater block. Any additional land area required is negligible when compared to the existing land area already occupied by the plant;[19]
4. No startup or shutdown requirements are considered for a heater. A heater can be activated or deactivated instantaneously;
5. $\dot{P}_{H,\mathrm{tot}} = \dot{Q}$: the heater's electrical-to-thermal conversion efficiency is 100 % (Zhai *et al.*, 2017; Schöniger *et al.*, 2020; Trieb and Thess, 2020);
6. The heater block's design lifetime is equal to the plant's;
7. No transient effects are considered for the heater block. The steady-state energy equation is solved at discrete steps in time;
8. The AEP and annual imported $\dot{P}_{H,\mathrm{tot}}$ remain constant for all $i \in [1, N]$;
9. The economic parameters remain constant over the plant's lifetime;
10. Annual degradation of plant components is not considered;
11. Net electrical power generated by the CSP plant at any instant can be utilised by the grid (Lovegrove *et al.*, 2018).

4.3 Conclusion

Chapter 4 documents the formulation of a techno-economic computational model of the CSP Carnot battery. Initially, the parabolic trough CSP plant is formulated and validated against a SAM benchmark model. With validation deemed sufficient, the parabolic trough plant is applied as a Carnot battery by integrating the heater block. The Carnot battery plant is validated internally through energy and mass balances.

---

[19] The approximate floor space occupied by one heater is 4.2 m^2 (EXHEAT, 2020). 100 heaters will occupy ≈ 0.009 % of the benchmark plant's total land area at design.

Chapter 5

Multi-objective Optimisation

The technical and economic elements of the Carnot battery performance model are defined. Although fundamental insight is provided by analysing system performance, an additional optimisation exercise unlocks key insights into what constitutes an optimally designed system and why. Potential trade-offs are also revealed during the exercise. The challenge of optimising the Carnot battery CSP plant, in terms of multiple desired performance metrics (objective functions), design variables and constraints, emerges. This chapter provides an overview of the optimisation problem, formulates a solution algorithm and introduces the reader to the main concepts and definitions.

5.0.1 Formulating the Optimisation Problem

Multi-objective optimisation (MOO) considers the optimisation of several objective functions simultaneously. The formal definition of the MOO problem is stated:

$$\min_{\mathbf{x}\in\mathbf{S}} \mathbf{F}(\mathbf{x}) = [f_1(\mathbf{x}), f_2(\mathbf{x}), f_3(\mathbf{x}), ..., f_k(\mathbf{x})]^T, \;\; \mathbf{x} = [x_1, x_2, x_3, ..., x_n]^T \in \mathbb{R}^n \tag{5.0.1}$$

Here, f_k is the k'th objective function, n the number of design variables and $\mathbf{x}$ the vector of design variables. $\mathbf{S} \subseteq \mathbf{D}$ is the set of all feasible points that satisfy the equality and inequality constraints (if any) in the unconstrained design space $\mathbf{D}$:

$$h_a(\mathbf{x}) = 0, \;\; a = 1, 2, 3, ..., m \tag{5.0.2}$$

$$g_j(\mathbf{x}) \leqslant 0, \;\; j = 1, 2, 3, ..., p \tag{5.0.3}$$

as well as boxed constraints. These simply define the lower (LB) and upper (UB) bounds on design variables in $\mathbf{D}$:

$$\mathbf{x}_{\mathrm{LB}} \leqslant \mathbf{x} \leqslant \mathbf{x}_{\mathrm{UB}} \tag{5.0.4}$$

Therefore, a design $\mathbf{x}$ is infeasible and $\notin \mathbf{S}$ if it violates Equation 5.0.2, 5.0.3 or 5.0.4, and is feasible ($\in \mathbf{S}$) if none of the constraints are violated.

The objective space **Z** contains all objective functions corresponding to designs in **D**, with the components of **F** forming the basis of **Z**. Each point in **D** maps to a single corresponding point in **Z**. On the other hand, $f_k \in \mathbf{Z}$ can map to multiple points in **D**. However, a point in **Z** is not always guaranteed to map to a point in **S** (Arora, 2012). Points in **Z** are attainable only if they map to corresponding points in **S**.

A unique solution $\mathbf{F}(\mathbf{x}^*)$ to Equation 5.0.1 would imply:

$$\mathbf{F}^* = \mathbf{F}(\mathbf{x}^*) \leqslant \mathbf{F}(\mathbf{x}), \quad \forall \mathbf{x} \in \mathbf{S} \tag{5.0.5}$$

In MOO however, Equation 5.0.1 rarely possesses a unique optimal solution (Arora, 2012). This leads to the concept of Pareto optimality (Section 5.0.2).

5.0.2 Pareto Optimality

Engineering optimisation frequently involves the optimisation of two or more objective functions. This is the crux of MOO. For example, it would seem obvious to maximise the CF, minimise the LCOE, minimise the LCOS and so forth. However, attempting to optimise all objective functions at once, provides a challenge for the following main reasons:

1. Individual objective functions $f_k(\mathbf{x})$ can have different global optima at different $\mathbf{x}^*$'s. Therefore, it cannot be guaranteed that a unique $\mathbf{x}^*$ will optimise all of $f_1(\mathbf{x}), ..., f_k(\mathbf{x})$ simultaneously;
2. Objective functions can be conflicting, that is optimising $f_1(\mathbf{x})$ will compromise $f_2(\mathbf{x})$, resulting in a “tug of war” for the same $\mathbf{x}^*$;
3. How does one best select a single promising solution that provides a trade-off between multiple optimal solutions?

A vast sum of literature is dedicated towards optimisation problems of this nature: Linder and Lindkvist (2011); Chiandussi *et al.* (2012); Wang and Rangaiah (2017); Limleamthong and Guillén-Gosálbez (2017); Starke *et al.* (2018), problems from which a set of Pareto optimal solutions can be constructed.

According to Arora (2012), a solution $\mathbf{x}^* \in \mathbf{D}$ is Pareto optimal if there exists no other $\mathbf{x} \in \mathbf{D}$ that improves at least one objective without worsening another. Pareto optimal points lie on a boundary, or Pareto frontier $P \subseteq \mathbf{Z}$, constructed by the mapping $\mathbf{F} : \mathbf{D} \rightarrow \mathbf{Z}$. On the frontier, one objective cannot be improved without deteriorating another. Any point on the Pareto front, $\mathbf{F}_{\text{front}}(\mathbf{x})$, is said to be non-dominated by all other $\mathbf{F}(\mathbf{x})$ not on the front (Arora, 2012). There are infinitely many Pareto optimal points on the frontier to choose from. Without a selection criterion imposed on the frontier, this complicates the process. Therefore, to convert the MOO into a single-objective optimisation problem, the selection of a compromise solution to $\mathbf{F}(\mathbf{x}^*)$ from the frontier is considered next.

5.0.3 The Utopian Point Selection Method

The utopian point compromise formulation is employed for its intuitiveness and simplicity. Consider a MOO problem in $\mathbb{R}^{k=2}$ as given in Figure 5.1.

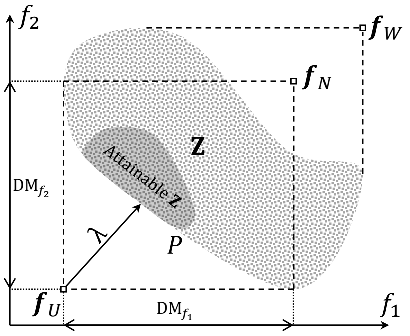

Figure 5.1: Graphical depiction of a MOO problem with utopian point selection.

The set P contains all Pareto optimal solutions on the frontier. The utopian point is the coordinate $\boldsymbol{f}_U$, generally expressed as:

$$\boldsymbol{f}_U = [\min f_1(\mathbf{x}), \min f_2(\mathbf{x}), ..., \min f_k(\mathbf{x})] \tag{5.0.6}$$

It represents the ideal (hence "utopian"), yet unattainable point where all objective functions are minimised simultaneously. Similarly, the nadir point $\boldsymbol{f}_N$ captures the upper bounds of the Pareto frontier (Grodzevich and Romanko, 2006). Its components are given by:

$$f_{N,\beta} = \max_{1 \leqslant \alpha \leqslant k} [f_\beta(\mathbf{x}^*_\alpha)], \ \ \forall \beta = 1, 2, 3, ..., k \tag{5.0.7}$$

where there are $\alpha \in [1, k]$ objectives. Practically, a total of k objective functions are minimised individually to obtain $\mathbf{x}^*_\alpha$ - the point that minimises the α'th objective. This process determines the utopian point. Each β'th objective is then evaluated at $\mathbf{x}^*_\alpha$, with the maximum of the $f_\beta(\mathbf{x}^*_{\alpha=1,2,3,...,k})$ providing $f_{N,\beta}$ (Arora, 2012). Utopian-nadir results are neatly packaged in a $\mathbf{M} \in \mathbb{R}^{\alpha \times \beta}$ payoff matrix (Linder and Lindkvist, 2011):

$$\mathbf{M} = \begin{bmatrix} f_{\beta=1}(\mathbf{x}^*_{\alpha=1}) & f_{\beta=2}(\mathbf{x}^*_{\alpha=1}) & \cdots & f_{\beta=k}(\mathbf{x}^*_{\alpha=1}) \\ f_{\beta=1}(\mathbf{x}^*_{\alpha=2}) & f_{\beta=2}(\mathbf{x}^*_{\alpha=2}) & \cdots & f_{\beta=k}(\mathbf{x}^*_{\alpha=2}) \\ \vdots & \vdots & \ddots & \vdots \\ f_{\beta=1}(\mathbf{x}^*_{\alpha=k}) & f_{\beta=2}(\mathbf{x}^*_{\alpha=k}) & \cdots & f_{\beta=k}(\mathbf{x}^*_{\alpha=k}) \end{bmatrix} \tag{5.0.8}$$

such that $\mathrm{diag}(\mathbf{M}) = \boldsymbol{f}_U$ and $\max_{1 \leqslant \beta \leqslant k} \mathrm{column}_\beta(\mathbf{M}) = \boldsymbol{f}_N$. Note that the nadir point should not be confused with $\boldsymbol{f}_W$, the "worst" (maximum) of each objective in $\mathbf{Z}$:

$$\boldsymbol{f}_W = [\max f_1(\mathbf{x}), \max f_2(\mathbf{x}), ..., \max f_k(\mathbf{x})] \tag{5.0.9}$$

Since $\boldsymbol{f}_U$ is unattainable, the second best solution to $\boldsymbol{f}_U$ is a compromise one as close as possible to it (Arora, 2012). Thus, let λ denote the dimensionless Euclidean distance in k-dimensional space from $\boldsymbol{f}_U$ to a solution in $\mathbf{Z}$:

$$\lambda = \left[\sum_{\iota=1}^{k} \left| \frac{f_\iota(\mathbf{x}) - f_{U,\iota}}{f_{N,\iota} - f_{U,\iota}} \right|^2 \right]^{1/2} \tag{5.0.10}$$

where $\lambda^* = \min \lambda$ for $\mathbf{x} \in \mathbf{S}$ corresponds to the selection of the compromise $\mathbf{F}^*$ in Equation 5.0.5. Equation 5.0.10 presents the distinct advantage of collapsing all objective functions into a single dimensionless objective variable, λ. The general minimisation of λ for $\mathbf{x} \in \mathbf{D}$ finds the shortest dimensionless distance from $\boldsymbol{f}_U$ to P. Therefore its solution is Pareto optimal and as close as possible to $\boldsymbol{f}_U$ (Arora, 2012), insofar as scaling influences the outcome. Other selection methods exist: the weighted sum method, weighted min-max method, lexicographic method, bounded objective function method and goal programming, each with unique advantages and disadvantages. Generally, the choice of method depends on user preference (Arora, 2012).

$\mathbf{F}$ likely contains function values linked to different performance metrics. Therefore, their relative orders of magnitude could differ significantly (Wang and Rangaiah, 2017). This risks skewing the minimisation of λ, given that a higher order of magnitude objective function will carry more "weight" or "importance" than its counterparts. To improve on this scaling problem, each objective function's distance from $\boldsymbol{f}_U$ is normalised about $f_{N,\iota} - f_{U,\iota}$, with the implication:

$$0 \leqslant \frac{f_\iota(\mathbf{x}) - f_{U,\iota}}{f_{N,\iota} - f_{U,\iota}} \leqslant 1 \tag{5.0.11}$$

which should assign the same relative magnitude to each normalised objective (Grodzevich and Romanko, 2006). Various normalisation schemes exist, but the utopian-nadir normalisation is most robust (Arora, 2012). It better reflects function behaviour at optimality with less distorted scaling, since the scaling is directly related to the geometry of the Pareto frontier (Grodzevich and Romanko, 2006). For example, if λ is normalised about $f_{W,\iota}$ instead, monotonic objective functions risk unnecessarily skewing the minimisation of λ.

A diversity metric, $\mathbf{DM}$, measuring the spread of P is defined as:

$$\mathbf{DM} = |\boldsymbol{f}_N - \boldsymbol{f}_U| \tag{5.0.12}$$

$\mathbf{DM} = \mathbf{0}$ indicates the complete absence of P in $\mathbf{Z} \in \mathbb{R}^k$, whereas $\mathbf{DM} > \mathbf{0}$ indicates a P in each of the mutually perpendicular coordinate planes of $\mathbf{Z}$. A comparison of the functional components of $\mathbf{DM}$ indicates the trade-off between objectives on the frontier. The $\mathbf{DM}$ especially provides valuable insight for problems in $\mathbb{R}^{k \geqslant 3}$, where engineering judgment becomes challenging.

The accuracy in locating λ^* improves with increased continuity of points in P.

Continuity rests largely on the density of designs (or "particles") in $\mathbf{Z}$. In other words, simulating more random design combinations allows λ^* (and hence the compromise $\mathbf{F}^*$) to converge and be identified with increased accuracy from P. However, this routine can be time consuming and inefficient. Section 5.0.4 demonstrates how the optimisation problem can be solved with more intelligent and significantly less particles in $\mathbf{Z}$.

5.0.4 Particle Swarm Optimisation

Particle Swarm Optimisation (PSO) was first introduced by Kennedy and Eberhart (1995). According to Wilke *et al.* (2006), PSO provides evolutionary advantages by sharing information between particles in a swarm, a routine often termed "collaborative searching". Due to its gradient-independence and simplicity, the basic structure of PSO as presented in Wilke *et al.* (2006) is formulated and shaped to solve the compromise optimisation with λ.

A swarm of ψ particles is allowed to search in the n-dimensional search (design) space. Each i'th particle is located and its position updated according to its current position vector $\mathbf{x}^i_\gamma$:

$$\mathbf{x}^i_{\gamma+1} = \mathbf{x}^i_\gamma + \mathbf{v}^i_{\gamma+1} \tag{5.0.13}$$

with γ the pseudotime increment (simply the iteration number) and $\mathbf{v}^i_{\gamma+1}$ a velocity vector given by:

$$\mathbf{v}^i_{\gamma+1} = \omega \mathbf{v}^i_\gamma + \boldsymbol{\nu}^i_\gamma \tag{5.0.14}$$

Here, ω is a real number inertia factor[20] and $\boldsymbol{\nu}^i_\gamma$ a stochastic velocity vector. This thesis considers the classical velocity update rule for the stochastic component of Equation 5.0.14. This rule introduces more randomness and allows directional diversity to be preserved within the search space. The classical velocity update rule is given by (Wilke *et al.*, 2006):

$$\boldsymbol{\nu}^i_\gamma = c_1 \mathbf{r}^i_{1\gamma} \bullet (\mathbf{p}^i_\gamma - \mathbf{x}^i_\gamma) + c_2 \mathbf{r}^i_{2\gamma} \bullet (\mathbf{p}^g_\gamma - \mathbf{x}^i_\gamma) \tag{5.0.15}$$

where c_1 and c_2 are real-valued cognitive and social scaling factors.[21] These enhance the magnitude diversity of searches. Furthermore, each entry of the random vectors $\mathbf{r}^i_{1\gamma}$ and $\mathbf{r}^i_{2\gamma}$ is an independent uniform random scalar $0 \leqslant \phi^i_{n\gamma} \leqslant 1$:

$$\mathbf{r}^i_{b\gamma} = [\phi^i_{1\gamma}, \phi^i_{2\gamma}, \phi^i_{3\gamma}, ..., \phi^i_{n\gamma}], \;\; b = 1, 2 \tag{5.0.16}$$

In particular, $\mathbf{p}^i_\gamma$ is the particle best position vector and $\mathbf{p}^g_\gamma$ is the swarm best position vector up to iteration γ. Each component of the cognitive $(\mathbf{p}^i_\gamma - \mathbf{x}^i_\gamma)$ and social $(\mathbf{p}^g_\gamma - \mathbf{x}^i_\gamma)$ vectors are scaled independently.

The first term in Equation 5.0.15 allocates cognitive memory to each particle.

---

[20] The classical PSO performs well for $0.4 \leqslant \omega \leqslant 0.6$ (Wilke *et al.*, 2006).

[21] Popular values have since become $c_1 = c_2 = 1.49445$ (Wilke *et al.*, 2006).

This enables each particle to remember its personal best λ_{γ}^{*} and associated $\mathbf{x}_{\gamma}^{*}$ with time. The second term in Equation 5.0.15 allocates social memory to the swarm. This enables the swarm to identify and remember its best λ_{γ}^{*} and associated $\mathbf{x}_{\gamma}^{*}$ located over time (Wilke *et al.*, 2006). The compromise objective function λ is evaluated at each $\mathbf{x}_{\gamma}^{i}$. As λ eventually converges to λ^{*} for $\mathbf{x} \in \mathbf{S}$, the compromise $\mathbf{F}^{*}(\mathbf{x})$ is pinpointed by λ^{*}.

At $\gamma = 0$ at the beginning of a run, particle positions are randomly launched:

$$\mathbf{x}_{0}^{i} = \mathbf{x}_{\mathrm{LB}} + \mathbf{r}_{0}^{i} \bullet (\mathbf{x}_{\mathrm{UB}} - \mathbf{x}_{\mathrm{LB}}) \tag{5.0.17}$$

Design variables are always constrained to $\mathbf{x}_{\mathrm{LB}} \leqslant \mathbf{x}^{i} \leqslant \mathbf{x}_{\mathrm{UB}}$ over time. Particles assume zero initial velocities.[22] A run denotes an independent set of PSO iterations. Compromise optimum results at the end of an iterative run are extracted and averaged across runs. This average determines the end result.

Disadvantages of PSO include a low iteration convergence rate and a susceptibility to get stuck in local minima for higher dimensional problems (Li *et al.*, 2014). Nonetheless, key attractive features of PSO for this thesis are (Wilke *et al.*, 2006):

1. Cognitive and social intelligence enable a significantly smaller swarm (number of particles) to locate λ^{*} with fewer iterations;[23]
2. The swarm can search over a continuous, discrete or mixed discrete-continuous domain.

In this thesis, the entries of $\mathbf{M}$ are determined according to Section 5.0.3 via PSO pre-applied to each individual objective function. During the MOO, $\boldsymbol{f}_{U}$ and $\boldsymbol{f}_{N}$ remain fixed in $\mathbf{Z}$ for all γ.

5.1 Conclusion

This chapter introduces MOO as it pertains to the CSP Carnot battery system. The optimisation problem is stated in Section 5.0.1. The solution framework for this problem is formulated. It rests on the concept of Pareto optimality (Section 5.0.2) combined with utopian point compromise selection (Section 5.0.3). This framework is coupled with PSO (Section 5.0.4). It is introduced as a means to "search" for the utopian point compromise solution to Equation 5.0.5 with significantly fewer points (particles) in the objective space and no prior knowledge of P. Attainable objectives in $\mathbf{Z}$ map to a design $\mathbf{x} \in \mathbf{S}$. In this case, P is not necessarily $\in$ attainable $\mathbf{Z}$. When $\mathbf{x} \in \mathbf{D}$ instead, solutions in $\mathbf{Z}$ are unconstrained and can be located freely on P.

---

[22] Enhanced search diversity via non-zero initial velocities introduces no distinct benefit in the classical PSO (Wilke *et al.*, 2006).

[23] In Wilke *et al.* (2006) a swarm of $\psi = 20$ particles is utilised to solve famous test functions, all of dimension $n = 30$. In solving Ackley's function, fast convergence is demonstrated with < 1000 iterations for $0.4 \leqslant \omega \leqslant 0.6$.

Chapter 6

Computational Results

This chapter contains a systematic investigation of and computational results for the parabolic trough CSP Carnot battery. The findings attempt to address the research objectives and questions of Section 3.2. The methodology follows.

6.1 Methodology

The Carnot battery stores potentially abundant RE from the grid. Via electric heaters, RE is converted into thermal energy which raises the charge state and average temperature of the hot tank during a solar thermal charge cycle. $\dot{P}_{\mathrm{RE}}$ is drawn entirely from solar PV electricity - the main contributor to a future duck curve (Dumont *et al.*, 2020). The plant prioritises a fixed 100 MW of baseload power generation. It aims to provide low-cost and around-the-clock electricity when possible. Analyses are conducted for the fixed design solar field size (non-optimised or benchmark Kathu Solar Park field). In Section 6.12, the effect of an increased solar field size is considered in essence.

Design variables of interest are those specifically linked to the TES and heater blocks. As such, the following design variables and their boxed constraints are considered: $1 \leqslant t_{\mathrm{TES}} \leqslant 20$ h, $0 \leqslant H_n \leqslant 100$ heaters and $389 \leqslant T_{\mathrm{set}} \leqslant 586$ °C. The objectives selected are the following: the LCOE is a high-level measure of the techno-economic performance of the plant as a whole. Similarly, the LCOS is a high-level measure of the techno-economic performance of the Carnot battery sub-system specifically (TES, heater and power blocks). The CF assesses to which extent the Carnot battery equips the CSP plant for around-the-clock power production. Furthermore, if CF is an indication of the continuity of power generation, then it is argued that CF is negatively correlated to the plant's intermittency. CF is also assumed to be directly proportional to the plant's continuity of inertial frequency support. Hence, the MOO includes these objectives such that $\mathbf{F} = [LCOS, LCOE, -CF]^T$.[24]

---

[24] Maximising CF is equivalent to minimising $-CF$. This would also mirror the minimisation of unused capacity, $100 - CF$ (%).

This Chapter is structured as follows: it contains parametric (Section 6.2) and techno-economic sensitivity (Section 6.3) analyses, considers the Carnot battery's technical benefits to the power cycle (Section 6.4), the value of its grid-scale service provision (Section 6.5) and the interplay between the stored energies (Section 6.6). The optimisation problem is addressed (Sections 6.7-6.10), followed by other techno-economic considerations (Sections 6.11). It is concluded with an optimised solar field study (Section 6.12).

6.2 Parametric Studies

A parametric study determines the variation in LCOS, LCOE and CF with the selected design variables, from which fundamental design and operational insights are deduced.

6.2.1 Installed Heater Capacity against Set-point Temperature

In Figure 6.1 the installed heater capacity is varied against the set-point temperature for a fixed 4.5 TES hours. The response surfaces of the LCOS (Figure 6.1a), LCOE (Figure 6.1b) and CF (Figure 6.1c) are shown. In LCOS and LCOE throughout, a discontinuity at $T_{\text{set}} = 400$ °C occurs. This indicates the added cost by switching the hot tank from carbon steel to stainless steel.

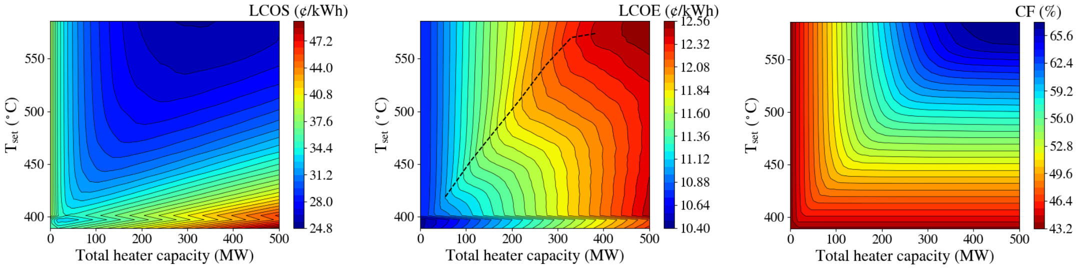

(a) $LCOS(H_{\text{cap}}, T_{\text{set}})$. (b) $LCOE(H_{\text{cap}}, T_{\text{set}})$. (c) $CF(H_{\text{cap}}, T_{\text{set}})$.

Figure 6.1: Parametric analysis: H_{cap} vs. T_{set}.

Figure 6.1a: LCOS

From the LCOS, it is seen that a large H_{cap} at a low T_{set} is an expensive design. For heater capacities > 0, the Carnot battery is better utilised at higher T_{set}'s. For any T_{set}, a heater capacity can be located that minimises the LCOS. This traces a diagonal valley of local minima across the surface, which allows the combination of lowest T_{set} and H_{cap} to yield the lowest LCOS.

Figure 6.1b: LCOE

The LCOE surface considers the entire plant power output and costs. The effect of increasing H_{cap} at a fixed T_{set} is considered first. The LCOE is observed to increase with H_{cap}. There exists no minimum LCOE except at the trivial solution of zero H_{cap}. Thus, the cost increase from storing more RE at larger H_{cap}'s continuously outgrows the gain in power generated. Hence, the LCOE increases with H_{cap}. Secondly, the effect of increasing T_{set} at a fixed heater capacity is considered. A more counterintuitive observation is the initial increase in LCOE with T_{set} at a fixed H_{cap}. A diagonal locus of maximum LCOE (dashed black line) is apparent, after which the LCOE decreases slightly as T_{set} is raised further. The origin of this trend is considered in more depth.

As T_{set} is increased up to the locus, more heaters of the installed capacity become utilised (illustrated in Figure 6.2a), hence the cost of charging with more RE increases. As noted previously, this cost increase continuously outgrows any improvements in the annual electricity production. Therefore, the LCOE initially increases with T_{set} at a given H_{cap}.

However, once T_{set} reaches the locus of maximum LCOE, nearly all of the installed heater capacity is utilised during a RE charge cycle (also illustrated in Figure 6.2a). For T_{set}'s above this locus, incrementally larger quantities of RE are stored (shown in Figure 6.2b on an annual basis) at a higher quality (higher T_{set}). This improves power generated from TES with little added charging costs. At this point, the gain in annual electricity production outgrows the additional charging costs and the LCOE decreases. This decrease is less evident at lower installed heater capacities.

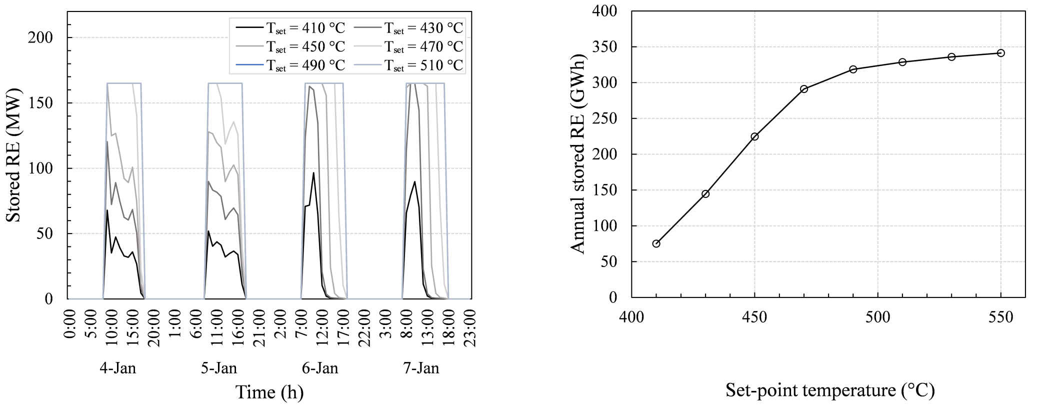

(a) RE charging profile snapshot.

(b) Annual stored RE.

Figure 6.2: RE charging characteristics vs. T_{set}.

Figure 6.2 illustrates the aforementioned underlying charging dynamic, with data collected for 4.5 TES hours and $H_{\text{cap}} = 165$ MW. From Figure 6.2a, at $T_{\text{set}} = 490$ °C and 510 °C as an example, the heater charging profiles overlap as the entire installed heater capacity becomes utilised to meet T_{set}. From

Figure 6.2b, the plateau in annual stored RE with T_{set} is evident.

Figure 6.3, drawn for 4.5 TES hours at increased installed heater capacities, shows the LCOE for lines of constant H_{cap} from Figure 6.1b. The locus of local maxima is indicated by the red dots. From the locus, larger H_{cap}'s coincide with higher T_{set}'s at which the LCOE peaks. Therefore, RE charging profiles only become overlapped at increasingly higher T_{set}'s as the installed heater capacity is increased (relating to Figure 6.2a). As a result, the annual stored RE and associated charging costs reach a plateau for larger T_{set}'s as H_{cap} is raised (relating to Figure 6.2b).

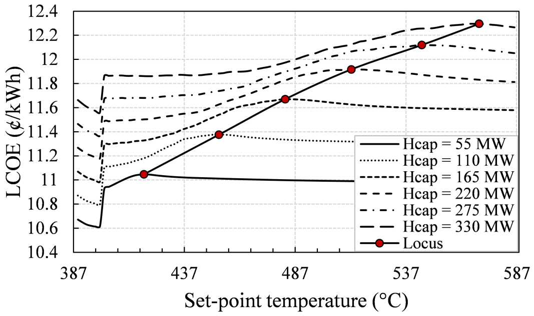

Figure 6.3: Relationship between LCOE_{max}, T_{set} and H_{cap}.

The impact of the RE charging cost on the shape of Figure 6.1b is assessed. In Figure 6.4, three LCOE surfaces are generated at 4.5 TES hours: the first for a 10 % reduction in the hourly TOU tariff, the second a 20 % reduction and the third a 50 % reduction. By lessening charging costs, it is apparent that the LCOE eventually transitions from high to low as T_{set} is increased at a given H_{cap}. Thus, the gain in annual electricity production more readily outgrows the added variable operating costs from charging RE to higher temperatures, given a reduction in the TOU tariff. As such, the economically optimum T_{set} can correspond to the thermodynamic optimum (as given by the CF, for example). At larger reductions in $C_{\text{RE}}(t)$ (Figure 6.4c), the integration of H_{cap} at a given T_{set} becomes increasingly favourable for a lower LCOE.

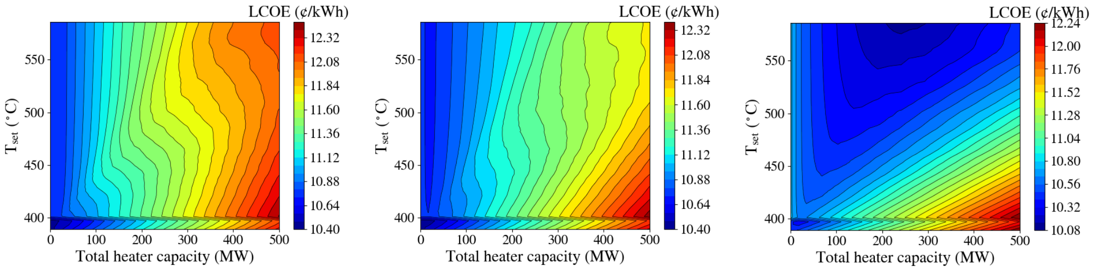

(a) 10 % reduction.
(b) 20 % reduction.
(c) 50 % reduction.

Figure 6.4: $LCOE(H_{\text{cap}}, T_{\text{set}})$ response to reduction in $C_{\text{RE}}(t)$.

Figure 6.1c: CF

Returning to Figure 6.1c, the maximum CF is attained at large installed heater capacities and high set-point temperatures. Contours of constant CF appear asymptotic in terms of H_{cap} and T_{set}, such that:

$$\text{As } H_{\text{cap}} \rightarrow H_{\text{cap}_{\text{UB}}}, \quad \left(\frac{\partial CF}{\partial H_{\text{cap}}}\right)_{T_{\text{set}}} \approx 0 \tag{6.2.1}$$

$$\text{As } T_{\text{set}} \rightarrow T_{\text{set}_{\text{UB}}}, \quad \left(\frac{\partial CF}{\partial T_{\text{set}}}\right)_{H_{\text{cap}}} \approx 0 \tag{6.2.2}$$

especially holds for regions further away from the maximum CF. A combination of lower H_{cap} and higher T_{set} therefore provides a CF equal to that from a higher H_{cap} and lower T_{set}. Indefinitely increasing one design variable, with the other held fixed (for $\mathbf{x}_{\text{fixed}} \not\approx \mathbf{x}_{\text{UB}}$), will not indefinitely increase the CF. The combination of lowest H_{cap} and T_{set} providing a maximum CF traces a diagonal edge of inflection points across the surface. Progressing along this diagonal instead, a sustained increase in the CF is guaranteed up to CF_{max} while utilising a minimum combination of each design variable.

A higher T_{set} is thermodynamically advantageous. This is conveyed in Figure 6.5, constructed for $t_{\text{TES}} = 4.5$ hours and $H_{\text{cap}} = 165$ MW. A higher T_{set} overcomes the thermal limitations imposed by the thermal oil on the hot molten salt. As discussed in Section 2.4.1, this is an inherent thermodynamic drawback of indirect TES in parabolic trough CSP plants. In this model, for example, an overall 10 °C oil-to-salt (5 °C) and salt-to-oil (5 °C) TES heat exchanger approach temperature drop is bridged by a higher T_{set} (Figure 6.5a). Due to Carnot's efficiency law, this increases the quality of work generated from TES. A higher T_{set} also prolongs TES discharge, due to an overall higher charge state of the hot molten salt (Figure 6.5b). The cumulative effect is a higher CF. Nonetheless, it is clear that the CF (purely thermodynamic) and LCOE-based optimum T_{set}'s could oppose depending on the TOU charging costs.

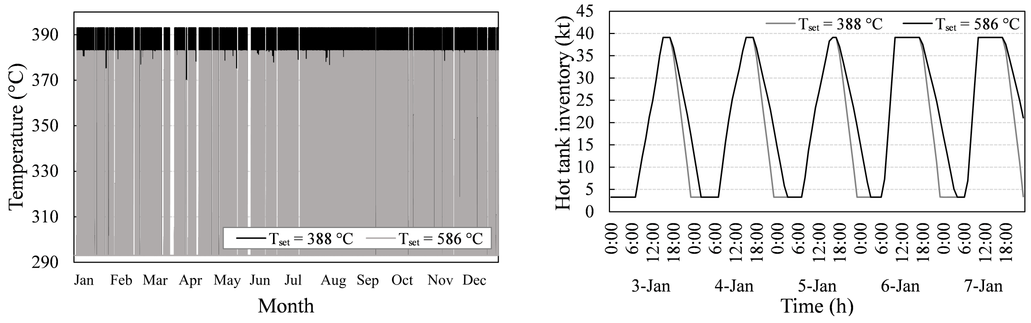

(a) TES HTF discharge temperature.

(b) TES discharge duration.

Figure 6.5: Influence of T_{set} on TES discharge characteristics.

6.2.2 TES Hours against Set-point Temperature

In Figure 6.6 the TES hours are varied against the set-point temperature at a fixed 165 MW installed heater capacity. The response surfaces of the LCOS (Figure 6.6a), LCOE (Figure 6.6b) and CF (Figure 6.6c) are shown.

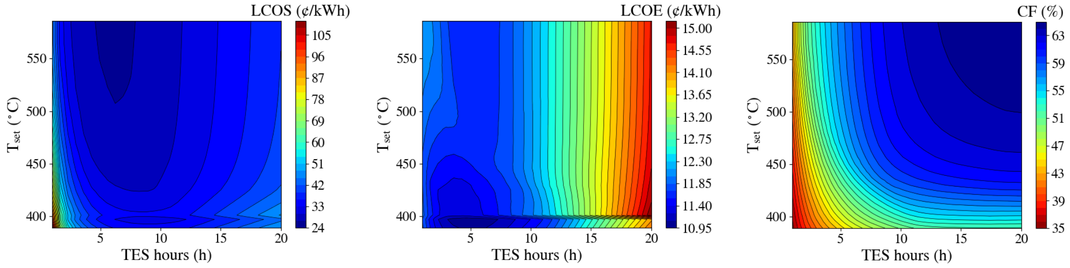

(a) $LCOS(t_{\text{TES}}, T_{\text{set}})$. (b) $LCOE(t_{\text{TES}}, T_{\text{set}})$. (c) $CF(t_{\text{TES}}, T_{\text{set}})$.

Figure 6.6: Parametric analysis: t_{TES} vs. T_{set}.

Figure 6.6a: LCOS

Regarding LCOS, a clear uneconomic operating point is that of a low T_{set} and small t_{TES}, resulting in substantial power cycle expenses not thoroughly compensated by electricity generated from storage (Equation 4.2.51). The advantage of a high T_{set} on the annual electricity production has been illustrated in Section 6.2.1.

Furthermore, a low t_{TES} restricts the electricity production from TES regardless of H_{cap}. This is expected, as TES capacity is an obvious prerequisite to store any quantity of RE via heater capacity. The TES capacity therefore ultimately governs the power generated from storage. At any T_{set}, a t_{TES} can be located that minimises the LCOS. This valley appears well-located about a band of optimum t_{TES}. Once more, LCOS decreases as T_{set} is increased. On the LCOS-level, this is indicative of the increased annual electricity production from storage outgrowing the increased charging costs from storing more RE.

Figure 6.6b: LCOE

In Figure 6.6b a valley of local minimum LCOE's is apparent, which shifts to slightly larger TES capacities as the set-point temperature is raised. The valley then remains largely fixed around a specific TES capacity as T_{set} is increased further. However, a slight decrease in LCOE is also evident. This response is likely due to the increase in RE charged as T_{set} is raised (increasing the LCOE), which stabilises and reduces the LCOE once a threshold T_{set} is reached (Section 6.2.1: Figures 6.2 and 6.3).

Figure 6.6c: CF

Lastly, Figure 6.6c essentially mirrors the response of Figure 6.1c and Equations 6.2.1 and 6.2.2. The highest CF is obtained at the near-maximum T_{set} and t_{TES}. A combination of low TES capacity and high T_{set} can provide the same CF as that from a high TES capacity and low T_{set}.

6.2.3 TES Hours against Installed Heater Capacity

In Figure 6.7 the TES capacity is varied against installed heater capacity at a fixed $T_{\text{set}} = 586$ °C. The response surfaces of the LCOS (Figure 6.7a), LCOE (Figure 6.7b) and CF (Figure 6.7c) are shown.

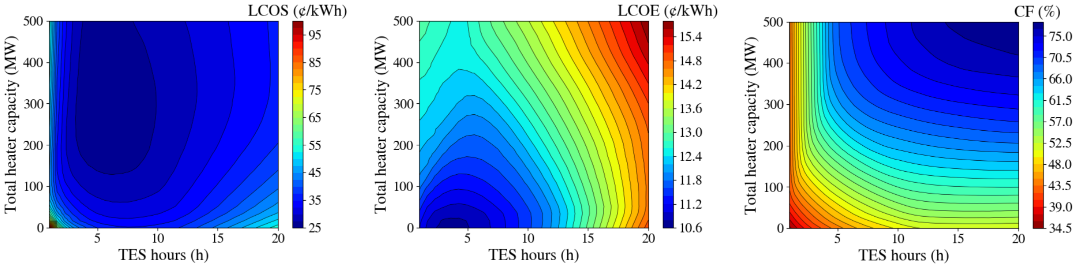

(a) $LCOS(t_{\text{TES}}, H_{\text{cap}})$. (b) $LCOE(t_{\text{TES}}, H_{\text{cap}})$. (c) $CF(t_{\text{TES}}, H_{\text{cap}})$.

Figure 6.7: Parametric analysis: t_{TES} vs. H_{cap}.

Figure 6.7a: LCOS

As noted previously, the LCOS displays a spike at $t_{\text{TES}} \approx 0$ hours and $H_{\text{cap}} \approx 0$ MW, due to the fixed investment cost of the power cycle at a 100 MW nameplate capacity. This is roughly 21.9 % more expensive than a conventional 4.5 hour TES system. If the power cycle was excluded from Equation 4.2.51, the minimum LCOS would be found near zero TES and heater capacity. That is where the associated variable and investment costs would drive to zero.

This however is a trivial minimisation which justifies the inclusion of the power cycle in the LCOS. The power cycle is an essential component of the Carnot battery, without which no electricity would be generated from stored thermal energy. The LCOS therefore favours a suitable t_{TES} (centred around an optimum valley) and substantial H_{cap} to maximise the power generated from storage, in order to overcome the fixed power cycle investment cost.

Figure 6.7b: LCOE

For a given t_{TES}, the LCOE increases with H_{cap} and traces a valley of local minima. As H_{cap} is raised, the valley initially shifts towards slightly larger TES capacities and eventually returns to smaller capacities. Gedle *et al.* (2020) presents a similar observation. This shift could likely be attributed to the interplay between stored solar thermal energy and RE. As demonstrated in Section 6.6 below, larger H_{cap}'s correspond to smaller TES capacities in order to mitigate excessive solar thermal energy curtailment.

Lastly, a reduction in the TOU tariff structure alters the LCOE surface in response to t_{TES} and H_{cap} (Figure 6.8). As the TOU charging costs are reduced, the global minimum LCOE favours increasingly larger H_{cap}'s, all centered around a definite valley in terms of t_{TES}. Figure 6.8's percentage reductions are arbitrarily selected to observe response transitions in $LCOE(t_{\text{TES}}, H_{\text{cap}})$. As such, the percentages differ from those in Figure 6.4 selected for $LCOE(H_{\text{cap}}, T_{\text{set}})$ response observations.

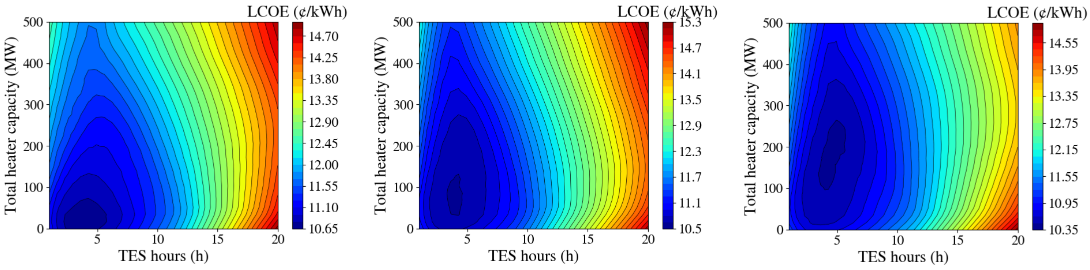

(a) 20 % reduction. (b) 33 % reduction. (c) 40 % reduction.

Figure 6.8: $LCOE(t_{\text{TES}}, H_{\text{cap}})$ response to reduction in $C_{\text{RE}}(t)$.

Figure 6.7c: CF

The remaining Figure 6.7c exhibits a response already familiar. The CF is maximised at large TES and heater capacities with a response reminiscent of Equations 6.2.1 and 6.2.2. A combination of a larger TES capacity and smaller heater capacity can provide the same CF as the converse combination.

6.3 Techno-economic Sensitivity Study

As a result of the high-level analysis, inherent uncertainty and potential dispute exists in the assumed values of economic parameters. The sensitivity of key TES, heater block and power cycle economic parameters are studied through the LCOE and LCOS. In Figure 6.9, the x-axis perturbs the default value of the economic parameter, where the y-axis measures the corresponding relative change in LCOE and LCOS. The figures are plotted for 4.5 TES hours, a 165 MW installed heater capacity and T_{set} = 586 °C. All unperturbed parameters remain at their default values.

The sensitivity study ultimately highlights parameters exerting the strongest influence on the outcome of techno-economic metrics. Sensitivities relevant to CSP costs only, such as the solar field, are not considered. They are not exclusively relevant to the Carnot battery (unlike the TES, heater and power blocks). Sensitivity towards time value of money parameters is also not considered.

Figure 6.9a confirms that the LCOE is most sensitive to the TOU charging cost, as suspected from preceding sections. Its influence on the LCOE of the Carnot battery far outweighs that of the direct capital cost (DCC) associated with the heater block installation. The power cycle and TES direct capital costs near equally exert the second largest influence on the LCOE. Regarding power cycle O&M costs, it is followed by the fixed and then the variable cost.

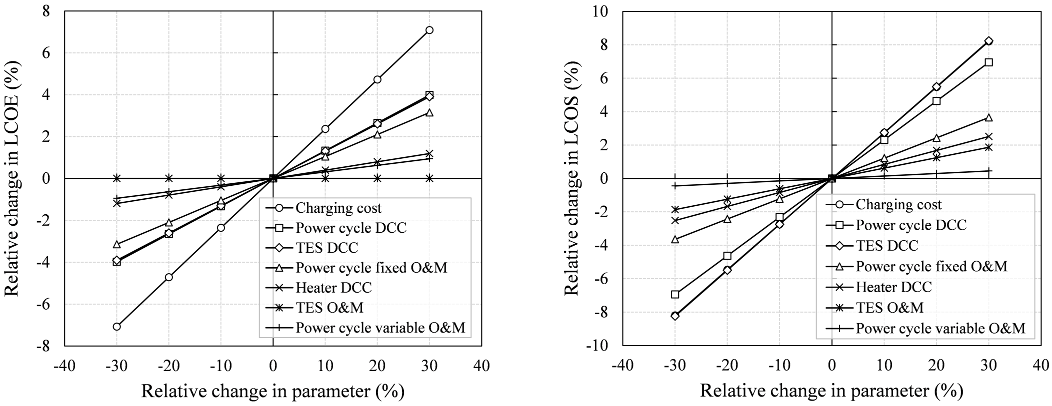

(a) LCOE sensitivity analysis.

(b) LCOS sensitivity analysis.

Figure 6.9: Sensitivity study of techno-economic parameters.

The LCOS is studied in Figure 6.9b. The TOU charging cost, together with the TES direct capital cost, exerts the strongest influence on the LCOS. Both far outweigh the heater direct capital cost. Following is the power cycle direct capital cost. Regarding O&M expenditures, the power cycle fixed O&M expenditure exerts the strongest change in LCOS, followed by the TES O&M expenditure and lastly, the power cycle variable O&M expenditure.

The cost of importing RE deserves emphasis: this parameter clearly exerts the greatest influence on the financial performance metrics and is more interesting in terms of uncertainty and future development. One avenue for calculating $C_{\mathrm{RE}}(t)$ is by assumption that the Megaflex tariffs apply (Section 4.2.8.2). However, this is not necessarily representative of the actual case. Future uptake of RE can significantly alter wholesale electricity price patterns from that of the present (Seel *et al.*, 2018).

Although Figures 6.4 and 6.8 are hypothetical, it could illustrate a future scenario where increased PV penetration leads to reduced wholesale electricity prices to incentivise consumption of and demand for abundant midday electricity through, for example, Carnot batteries. As the figures show, reduced charging costs will impact the installed heater capacity for which the LCOE is a minimum. In Figure 6.4 it can also alter the very definition of what constitutes an economically optimum set-point temperature for a certain H_{cap}.

The charging cost scheme in this thesis is but one of many likely outcomes in literature. Seel *et al.* (2018) suggests an overall decrease in the 2030 USA hourly average electricity wholesale price with increased RE uptake. High solar penetration effects substantial change in diurnal price patterns and overall price variation, whereas wind contributes to irregularity in pricing patterns. Furthermore, temporal and geographic changes in price profiles, as well as negative and volatile prices are emphasises by Wiser *et al.* (2017).

A study by Mahony and Baartman (2018) paints additional uncertainty for South Africa, which has seen electricity tariff escalations above inflation. As Eskom's primary revenue from industrial electricity sales decline due to reduced consumption from these users, a positive feedback loop is set in motion. When consumers progressively switch to off-grid technologies (such as solar PV), power utilities are forced to increase tariffs to cover fixed costs.

At the same time, the remaining pool of grid-connected consumers shrinks due to the increase imposed on them (Eskom, 2017). Arguably, increased RE uptake in South Africa could escalate wholesale electricity prices even further. According to Mahony and Baartman (2018) however, Eskom proposed more cost-reflective tariffs, specifically aimed at industrial consumers, stabilising and growing their consumption to counteract the so-called “utility death spiral”.

Considering these viewpoints, the evolution of wholesale electricity prices in South Africa might exacerbate or alleviate the assumed charging costs in Section 4.2.8.2. For the purpose of this thesis however, changes in future power system characteristics are uncertainties to be kept in consideration.

6.4 Technical Benefits of a Carnot Battery to the Power Cycle

Figure 6.10 illustrates the effect of added heater capacity, at a $t_{\text{TES}} = 4.5$ hours and $T_{\text{set}} = 586$ °C example case, on the power cycle. The TES discharge window (unshaded) is the period of time during which the power cycle requires, but cannot necessarily be fully supplied with energy from TES. This typically occurs between sunset and sunrise, when the solar field produces inadequate or no solar thermal energy. The RE charge window (shaded blue) shows periods where RE electricity is imported for storage. A snapshot of the accompanying TES charge state is provided in Figure 6.12a.

By installing a larger heater capacity for the RE charge windows, the TES system is able to supply a greater portion of the discharge window. The enhanced quality of thermal energy supplied to the power cycle is evident from the higher net power generated when $H_{\text{cap}} > 0$. Therefore, more of the high-temperature stored thermal energy is converted into work. The increased quantity of stored thermal energy also allows for prolonged power generation during the TES discharge window, in comparison to a scenario with no heaters installed.

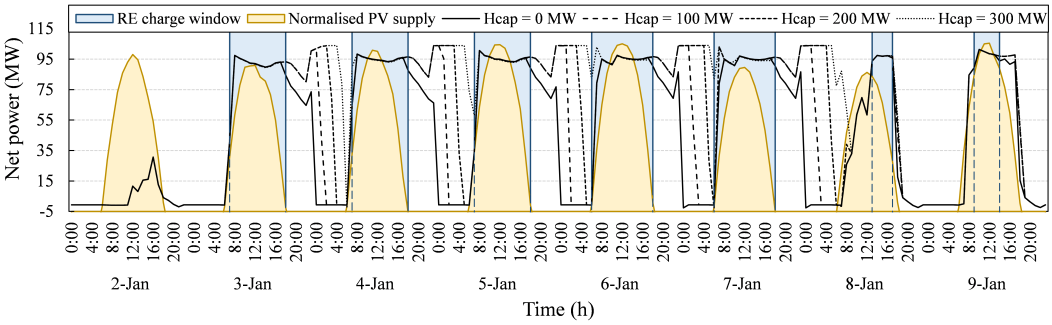

Figure 6.10: Effect of H_{cap} on power cycle performance.

During periods of poor solar resource (2, 8 and 9 January), the power output essentially remains unchanged regardless of the heater capacity. This is because the power cycle receives a greater share of thermal energy from the solar field. As a result, solar thermal charge cycles are brief (8 and 9 January) or non-existent (2 January). The performance during winter months achieves few of the aforementioned technical benefits. The Carnot battery generally charges less RE due to the diminished solar thermal charge cycles. These rarely attain a full solar thermal charge state during winter.

Increasing H_{cap} for a given t_{TES} shows potential to reduce the frequency of power cycle startups (and shutdowns) throughout the year, thereby increasing utilisation of the power block. Startup cycles strongly contribute to thermal stresses endured by steam turbines (Leyzerovich, 2008; Garcia *et al.*, 2013). Thermal stresses are the prevailing problem in cycling steam turbines. Reducing these stresses can lessen long-term wear and tear, equipment repair and replacement, unit unavailability (Flynn, 2003) and thermal fatigue (Leyzerovich, 2008), thereby increasing turbine operating life (Poole and Dinter, 2017).

The potential for startup reduction is assessed, and confirmed, in Figure 6.11 for $T_{\text{set}} = 586$ °C. Given that range of design variables, power cycle startups can vary between 357 and 139 annually (a reduction potential of nearly 61 %) for this case. The onset of startup reduction is defined as the boundary where reduction is initiated, dashed white in Figure 6.11b. For any H_{cap}, a TES capacity below this boundary does not influence the power cycle startups. When increasing H_{cap} within the lower band of roughly 38 MW to 225 MW, the onset of startup reduction occurs at lower TES capacities. For larger values of H_{cap}, the onset levels off at about 3.1 hours. Power cycle startups cannot be altered by H_{cap} for TES capacities below 3.1 hours.

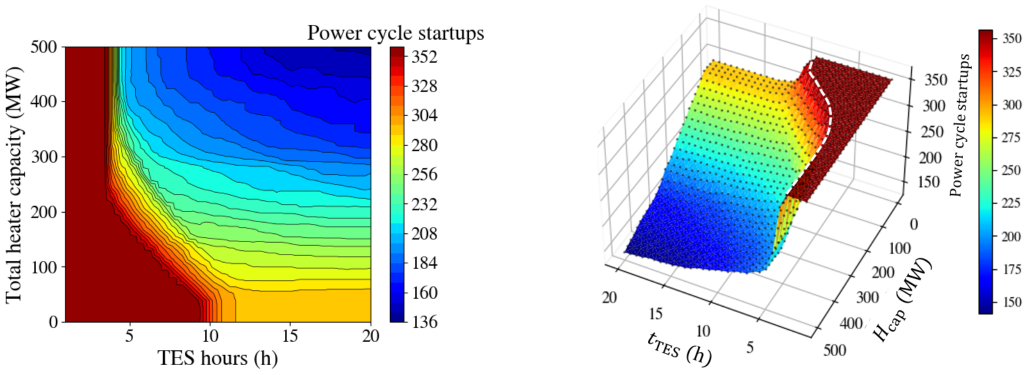

(a) (b)

Figure 6.11: Annual power cycle startups as $f(t_{\text{TES}}, H_{\text{cap}})$.

6.5 Value of the CSP Carnot Battery's Service

Future duck curves will be strongly affected by the solar PV generation profile that peaks central daylight hours. Storage technologies such as Carnot batteries should therefore operate to shift grid-scale quantities of energy "away" from this central period of overproduction to periods of underproduction for several hours per day (Pearre and Swan, 2015; Dumont *et al.*, 2020). Figure 6.10 shows that the Carnot battery is operating as intended. It stores grid-scale quantities of potentially abundant and intermittent RE (in this case, solar PV) during the RE charge window.

It proceeds to discharge that energy as a dispatchable base-load supply during the evenings and early mornings, generating stable and reliable power in the absence of sunlight. For example, at a heater capacity of 300 MW and a set-point temperature of 586 °C, Kathu's CF increases from 43.5 % to 64.4 %, much higher than the typical average capacity factors for CSP plants in South Africa (Figure 2.1b). However, this raises the LCOE by 1.73 ¢/kWh. For investment profitability, the LPOE increases from 0.096 ¢/kWh to 0.108 ¢/kWh.

The value of the Carnot battery's service to the grid could outweigh the general LCOE increase. In fact, a major shortfall in measuring performance with LCOE or LCOS is its lack of quantifying the value of the service provided by the storage technology (Denholm *et al.*, 2021). The service under consideration is referred to as the time-shifting of electric energy - an important flexibility provided by grid-scale energy storage to a future grid with a high share of RE. If the off-peak RE is in surplus to the demand, it would otherwise be curtailed (Akhil *et al.*, 2015) to avoid over-frequency generator-tripping (Guo *et al.*, 2018).

A study by Garcia *et al.* (2013), which considers time-shifting grid electricity from low to high demand periods through thermocline TES in CSP, arrives at a similar conclusion. Their analysis also indicates an increased LCOE using electric heaters to facilitate electric energy arbitrage. The authors advise against the LCOE as sole performance metric since it cannot convey the value of electricity generated from TES in light of the TOD remuneration structure (Garcia *et al.*, 2013). However, for a flat TOD tariff structure, the LCOE will indicate the ideal plant configuration (Auret, 2015; Poole, 2017).

The seasonality of standard solar thermal charge cycles and discharge cycles of a baseload parabolic trough plant in assisting the time-shifting of RE is assessed. Figure 6.12 supports the observations to follow.

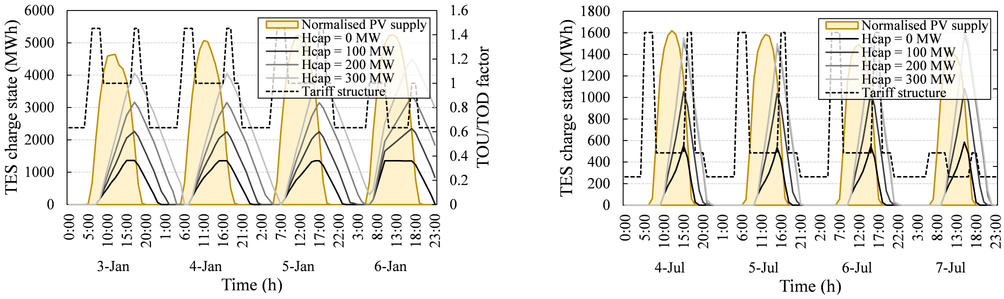

(a) Summer snapshot.

(b) Winter snapshot.

Figure 6.12: Effects of seasonality on RE time-shifting.

Ideal time-shifting cannot be guaranteed during all seasons. Intermittency aside, a Carnot battery reliant on solar thermal charge cycles to store RE will provide better time-shifting, both temporally and in magnitude, during summer, as opposed to winter. During summer, over-generation of field solar thermal energy in excess of the power cycle demand typically arises earlier in the day and occurs with greater abundance. In comparison to winter, it tends to coincide conveniently (time-of-day wise) with increased solar PV generation and off-peak periods on the grid.

Thus during summer months, solar PV can be stored when it is most abundant and potentially in excess, in an effort to mitigate the duck curve's belly. Under baseload operation, the power cycle's demand for thermal energy appropriately arises later in the day as the solar PV supply diminishes. The stored RE is only discharged at that time, enhancing ideal time-shifting of abundant solar PV on the grid. Due to the higher charge states attained, energy discharge can often continue into the night and early mornings. This is rarely the case for winter.

During winter, less surplus solar thermal energy is generated by the field, of which the power cycle has priority in consuming it. As such, winter solar thermal charge cycles tend to arise later in the day compared to summer. They are also shorter and prone to attain lower charge states. This results in less

RE stored during abundant solar PV periods. The power cycle tends to demand stored thermal energy earlier in the day than during summer months, resulting in an overall sub-optimal time-shift of the stored RE. To achieve the same temporal magnitude of summer time-shifting during winter, a tailored TOD control or dispatch strategy is suggested.

Another beneficial service of the CSP Carnot battery is the inertia inherent to the power generated (Section 2.2.2.2 considers the advantages of inertia). As per Section 2.2.2.2, a challenge with the increased uptake of solar PV generation (inverter-based power supply) is the lack of inherent inertial support as provided by large rotating generators (Denholm *et al.*, 2020). However, the CSP Carnot battery transforms “inertialess” solar PV generation into power inherently generated with inertia. As seen from Figure 6.11, the CSP Carnot battery can be sized to enhance the continuity of this support.

CSP Carnot batteries could encourage the uptake of more inverter-based renewable generators while maintaining a level of inherent inertial support in the grid. (Battery energy storage, on the contrary, does not provide inherent inertial support.) In the Western USA for example, fast-responding inverter-based generators coupled with renewable synchronous generators (such as CSP) could permit higher proportions of RE uptake without a fundamentally different approach to grid stability (Denholm *et al.*, 2020).

6.6 Interplay between Stored Solar Thermal Energy and Imported RE

With a larger ΔT between the hot and cold tank, increasing $H_{\text{cap}} > 0$ can prolong the TES discharge duration (contributing to a higher CF). This is illustrated with arrows in Figure 6.13 for 4.5 TES hours and T_{set} = 586 °C.

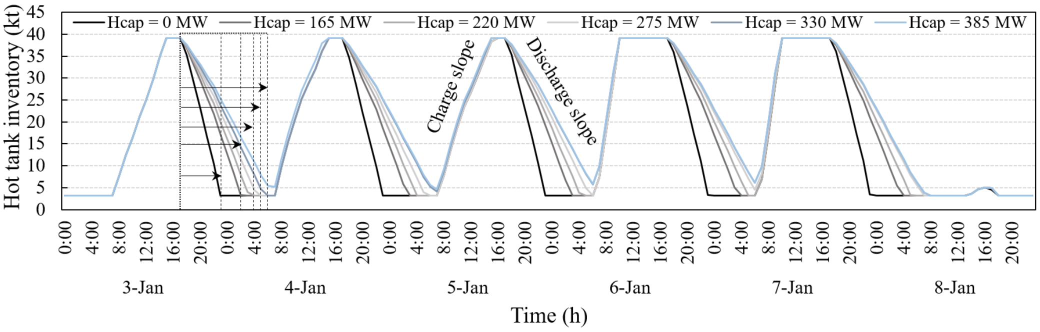

Figure 6.13: TES hot inventory level for $H_{\text{cap}} = 0$ and $H_{\text{cap}} > 0$.

For baseload operation, ideal charge-discharge cycles have solar thermal charging of the TES commence almost immediately once the hot inventory is depleted. Such performance is desirable, but not necessarily always guaranteed. The TES capacity is utilised optimally, because the discharge cycle is prolonged without adverse effects on the subsequent solar thermal charge cycle.

However, indefinitely adding more heaters results in incomplete discharge (eventually superimposed at larger H_{cap}), as also evidenced by Figure 6.13. The residual hot inventory at the end of a discharge reduces the available intake capacity of a subsequent solar thermal charge cycle, thereby exacerbating TES overcharge. A quantity of solar thermal energy that would otherwise be stored, is curtailed during the subsequent solar thermal charge cycle. This reduces the utilisation factor unnecessarily - a scenario that should be avoided if possible. Figure 6.14 is constructed to aid in this regard. Here T_{set} is maintained at 586 °C which, drawing from Figure 6.5b, accounts for the "worst case" scenario in terms of a premature decrease in the utilisation factor.

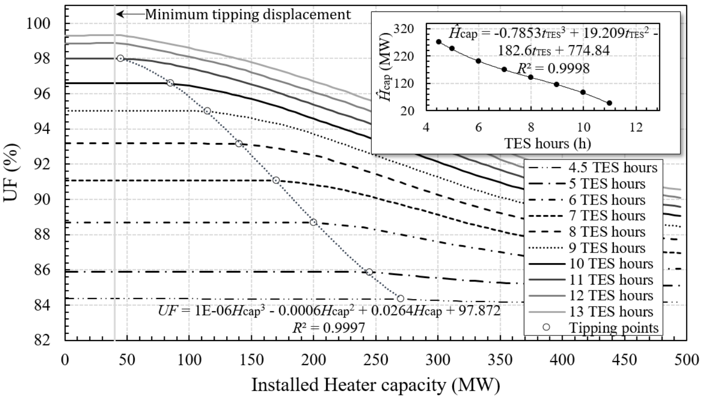

Figure 6.14: UF vs. installed heater capacity and TES hours.

Firstly, by increasing the TES capacity the UF increases incrementally. This is expected, since a larger storage capacity reduces the need to curtail surplus solar thermal energy from the field. Secondly, as heaters are integrated at a fixed TES capacity, a tipping point occurs at which the UF begins to drop below its attainable maximum. This locus is fitted accordingly. A minimum tipping displacement is also shown where H_{cap} reaches a minimum for all UF tipping points. This occurs at roughly a 40 MW installed heater capacity.

With increased H_{cap}, the UF drop becomes more pronounced at larger TES capacities. An additional trendline (shown in Figure 6.14's window plot) suggests an inverse relationship between the TES capacity and installed heater capacity at the tipping point (hereon denoted $\hat{H}_{\text{cap}}$). By designing the system solely on the tipping point locus, a larger heater capacity will correspond to a smaller TES capacity, and *vice versa*. It appears that a larger H_{cap} essentially recovers the solar thermal contribution reduced by smaller TES hours.

The solar thermal discharge duration at a given storage capacity (for $H_{\text{cap}} = 0$)

contributes an explanation for this inverse relationship. By increasing the TES capacity, the period of solar thermal charge depletion decreases (Figure 6.15). Through Figure 6.13, its is known that adding heater capacity prolongs discharge duration (indicated by the arrows) and decreases the discharge slope.

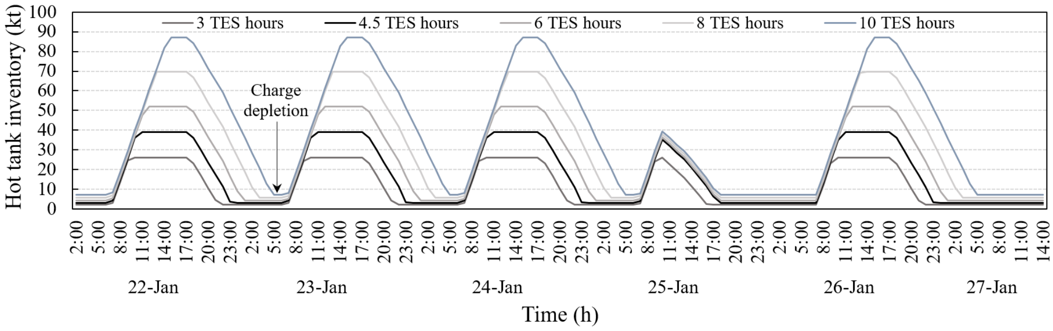

Figure 6.15: TES hot inventory level as $f(t_{\text{TES}}, H_{\text{cap}} = 0)$.

Thus it is graphically concluded that the addition of heater capacity (lower discharge slopes) to a larger TES capacity (shorter charge depletions) results in a quicker RE overcharge (characterised by an incomplete discharge) than for a lower TES capacity. In short, smaller TES capacities with longer periods of solar thermal charge depletion can be fitted with greater heater capacities before the onset of overcharge from RE. Larger TES capacities introduce shorter periods of charge depletion and is more susceptible to an RE overcharge when heater capacity is added. As evidenced by 25 January 8:00-17:00, the charge depletion effect is mild during periods of poorer solar resource.

Operating purposefully beyond $\hat{H}_{\text{cap}}$ will reduce the annual stored field energy. Therefore, imported RE is stored at the expense of solar thermal energy. The solar field as an investment essentially becomes more expensive and oversized, because its cost remains unchanged but its utilisation decreases. The value of Figure 6.14 lies in consulting it to avoid such a scenario.

6.7 Optimisation Set-up

MOO is performed to reveal insights into what constitutes an "optimally designed" CSP Carnot battery and why. Design variables $\mathbf{x} = [t_{\text{TES}}, H_n, T_{\text{set}}]^T$ and objective functions $\mathbf{F} = [LCOS, LCOE, -CF]^T$ are optimised. The selection of objective functions and design variables is motivated in Section 6.1. The particle swarm optimisation is configured as follows: convergence trial-and-error testing yields an acceptable swarm size of $\psi = 7$ and inertia factor $\omega = 0.5$. Cognitive and social scaling factors are weighted equally, $c_1 = c_2 = 1.49445$. Five runs are conducted, each terminating at 30 iterations. Optimum results at the end of the iterations are stored and averaged across the runs.

As per Section 5.0.3, **M** is found by applying PSO to each individual unconstrained objective ($\mathbf{x} \in \mathbf{D}$):

$$\mathbf{M} = \begin{bmatrix} 25.25 & 12.06 & -65.787 \\ 44.26 & 10.73 & -41.038 \\ 35.68 & 15.75 & -77.892 \end{bmatrix} \tag{6.7.1}$$

during which a maximum standard deviation of 0.0329 occurs in LCOE_U. Section 6.6 motivates selecting $H_{\text{cap}} \leqslant \hat{H}_{\text{cap}}$ at a given t_{TES} for $T_{\text{set}} = 586$ °C. This is implemented as a boxed constraint:

$$H_{\text{cap}} \in [H_{\text{cap}_{\text{LB}}}, \hat{H}_{\text{cap}}(t_{\text{TES}})|_{T_{\text{set}}=586\ ^\circ\text{C}}] \tag{6.7.2}$$

where $\hat{H}_{\text{cap}}(t_{\text{TES}})$ is the correlation given in the window plot of Figure 6.14. The remaining design variables are bounded by boxed constraints (Equation 5.0.4).

6.8 Optimisation Performance and Results

The same PSO configuration is next applied to the actual constrained MOO problem ($\mathbf{x} \in \mathbf{S}$), for which the results are provided below. Technical considerations on the application of PSO to this compromise MOO problem are shown first, after which the significance of the results is explored.

The optimum compromise results are found with repeated accuracy and little deviation from the mean across runs, as summarised in Table 6.1. Each independent run samples the optimum results ($\mathbf{p}^g$ and associated $\mathbf{x}^*$) at the end of 30 iterations of PSO. This therefore suggests that the swarm confidently strives towards the true constrained global minimum λ across runs.

Table 6.1: PSO repeatability in optimum results.

Parameter	**Average**	**Standard deviation**	**Unit**
t^*_{TES}	5.07	0.0004	h
H^*_{cap}	240.475	0.0199	MW
T^*_{set}	586	0	°C
λ^*	0.474	2.75×10^{-6}	-

Table 6.1 also shows that Constraint 6.7.2 is satisfied, as $H^*_{\text{cap}} \approx \hat{H}_{\text{cap}}(t^*_{\text{TES}})$. For the given t^*_{TES}, an appropriate capacity of heaters $H^*_{\text{cap}} = \hat{H}_{\text{cap}}$ can thus be included without unnecessarily discarding solar thermal energy from the field. This ensures the field is maximally utilised at t^*_{TES}. The rather fast convergence history in each $\mathbf{x}$ and λ is illustrated in Figures 6.16a-6.16d. Figure 6.16c and Table 6.1 indeed confirm that $T^*_{\text{set}} = 586$ °C, indicating that the LCOE's penalty for higher T_{set}'s is outweighed by other priority considerations.

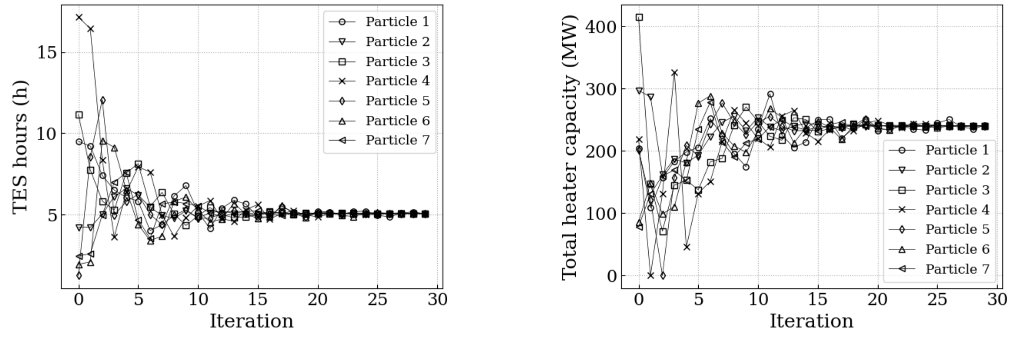

(a) Example convergence of t_{TES}. (b) Example convergence of H_{cap}.

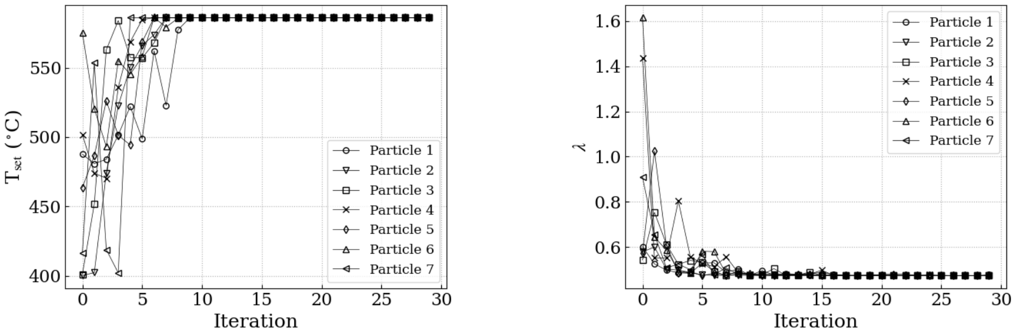

(c) Example convergence of T_{set}. (d) Example convergence of λ.

Figure 6.16: PSO convergence study.

The optimised results are summarised and compared to that from the benchmark plant in Table 6.2.

Table 6.2: Optimised vs. benchmark variables and metrics.

Parameter or metric	**Baseline value**	**Optimised value**	**Unit**
TES hours	4.5	5.07	h
Total heater capacity	-	240.48	MW
T_{set}	-	586	°C
LCOS	35.75	25.55	¢/kWh
LCOE	10.43	11.86	¢/kWh
CF	43.54	62.57	%
UF	84.36	86.07	%
Bid price	11.00	12.51	¢/kWh
Round-trip efficiency	26.95	29.78	%
LPOE	0.096	0.105	¢/kWh

In this case, the compromise optimum design would decrease the LCOS by 10.2 ¢/kWh, raise the LCOE by 1.43 ¢/kWh and boost the CF by 19.03 percentage points. The bid price is raised by 1.51 ¢/kWh and the round-trip efficiency increases by 2.83 percentage points (even though it is excluded as an objective function). Although the LCOE increases, it can be argued that this increase is outweighed by the actual value of the service provided by the Carnot battery (Section 6.5). Should the decision maker deem the LCOE more important a performance metric, a weighted global criterion method, as outlined in Arora (2012), is more appropriate to determine the compromise solution. Currently, all objective functions are weighted equally with no decision-maker bias. Despite the LCOE increase, the compromise solution remains profitable as Equation 4.2.49 calculates the LPOE as 0.105 ¢/kWh.

As a point of interest, the MOO is also executed for $\dot{P}_{\text{RE}}$ imported from wind instead of solar PV electricity. It is observed that the MOO results do not differ significantly from the solar PV case. This is predominantly due to similar heater charging cycles (both temporally and in magnitude), regardless of whether RE is charged from wind or solar PV electricity for storage.

6.9 Pareto Front Analysis

By studying the Pareto fronts, more insight can be gained into this particular MOO problem and its compromise solution in Table 6.2. The analysis is depicted in Figure 6.17, obtained by simulating 1600 designs at $T_{\text{set}} = 586$ °C.

The blue shaded regions depict objectives in $\mathbf{Z}$ which are attainable, corresponding to designs not violating Constraint 6.7.2 ($H_{\text{cap}} \leqslant \hat{H}_{\text{cap}}$). Also shown are the results for: the 2D unconstrained optimum for validation purposes only ($\mathbf{F}$ consisting only of the two objectives shown on the axes, disregarding constraints); the 3D unconstrained optimum (considering all three objectives in $\mathbf{F}$, disregarding constraints); as well as the 3D constrained optimum (all three objectives in $\mathbf{F}$, restricted to the attainable $\mathbf{Z}$).

As $\mathbf{Z} \in \mathbb{R}^{k=3}$, P is projected onto mutually perpendicular planes in Figures 6.17a-6.17c, revealing the trade-offs between each of the objectives in 2D with eased interpretation. It is seen that all 2D unconstrained solutions lie on the frontier. This validates the MOO routine developed in Chapter 5, because utopian point compromise solutions are Pareto optimal (Arora, 2012). By activating Constraint 6.7.2, solutions become bounded to those attainable in $\mathbf{Z}$. These might not necessarily be $\in P$ in some projections, but would be near to it, as illustrated in the given figures. All standard deviations in λ^* are $\leqslant 0.0007$.

Figure 6.17a considers $P(LCOE, LCOS)$, with $DM_{\text{LCOE}} = 1.32$ ¢/kWh and $DM_{\text{LCOS}} = 19.01$ ¢/kWh. The trade-off between LCOE and LCOS is clear: a relatively small sacrifice in LCOE can improve the LCOS significantly ($DM_{\text{LCOE}} \ll DM_{\text{LCOS}}$), assuming both are equally important to the decision maker. The swarm therefore locates LCOE* near its nadir component and LCOS* close to its utopian component in the 3D unconstrained and constrained problems.

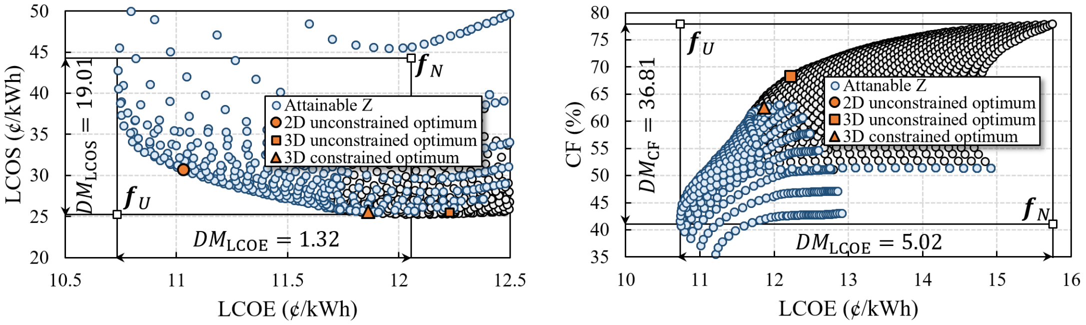

(a) $P(LCOE, LCOS)$.

(b) $P(LCOE, CF)$.

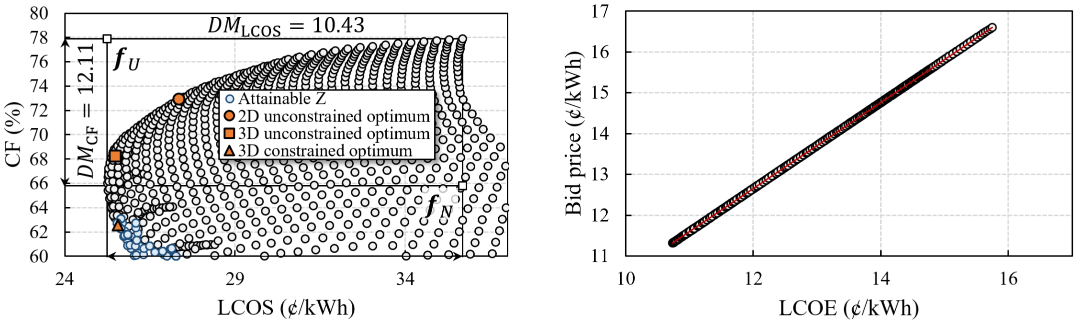

(c) $P(LCOS, CF)$.

(d) $P(LCOE, Bid\ price)$.

Figure 6.17: Pareto front analysis.

Figure 6.17b examines $P(LCOE, CF)$, with $DM_{\text{LCOE}} = 5.02$ ¢/kWh and $DM_{\text{CF}} = 36.81$ %. Here the compromise is less obvious, considering this trade-off contains the strongest (largest) DM's in both LCOE and CF. As a result, the unconstrained 3D optimum compromise is not located particularly close to any nadir or utopian components (as in Figure 6.17a's case), but rather occupy the same vicinity on the "nose" of P. Clearly the LCOE-CF trade-off dominates the full unconstrained MOO problem. Adding a third dimension to $\mathbf{F}$ hardly alters the 3D from the 2D unconstrained solution. Thus in the 3D unconstrained case, $P(LCOE, CF)$ governs $P(LCOE, LCOS)$ and $P(LCOS, CF)$. Figure 6.17b's optimum constrained compromise solution in 3D becomes restricted to slightly lower CF's and LCOE's.

Figure 6.17c observes $P(LCOS, CF)$, with $DM_{\text{LCOS}} = 10.43$ ¢/kWh and $DM_{\text{CF}} = 12.11$ %. This trade-off contains the second strongest DM in LCOS and the weakest in CF. Consequently, the unconstrained 3D solution lies near the utopian LCOS and nadir CF. However, the 3D constrained optimum is shifted towards the attainable $\mathbf{Z}$ closest to P.

Why can the bid price or LPOE be excluded from $\mathbf{F}$? A power utility should be particularly interested in the bid price, being the final "¢/kWh-agreement" at which the plant sells electricity to the utility. This could justify the inclusion of the bid price as a fourth objective function to accommodate the utility's interests. A minimised bid price (yet profitable LPOE) would yield a more competitive PPA from both entities' perspective.

It follows that Figure 6.17d reveals a linear relationship between LCOE and bid price, as might be anticipated from Section 4.2.6. No compromise exists, since the minimum bid price would exist at the minimum LCOE. Therefore, both entities' interests (a competitive PPA) is taken into consideration with the LCOE in $\mathbf{F}$. Due to its interdependence, the LPOE is also excluded from $\mathbf{F}$. The linearity only holds for flat TOD tariff structures (Section 4.2.6.4).

6.10 Significance of the Optimisation Results

In Table 6.2, why is it preferable to incur a relatively small change in TES capacity while there is a large (and maybe unrealistic) increase in H_{cap}? Increasing the TES capacity is costly if it is not utilised properly. Proper utilisation of t_{TES} can be viewed from two contrasting perspectives:

1. The trade-off between stored solar thermal energy only and the cost thereof (conventional plant);
2. The trade-off between stored solar thermal energy and imported RE as well as the cost of storing both (Carnot battery plant).

Considering the former, there is a limit to the actual quantity of solar thermal energy stored as the TES capacity, and associated capital and operating expenditures, is increased. Theoretically, this limit occurs as UF approaches its attainable maximum for t_{TES} near its upper bound. However, for $t_{\text{TES}_{\text{LB}}} < t_{\text{TES}} < t_{\text{TES}_{\text{UB}}}$, solar thermal sizing of t_{TES} can already reach a point where the added costs outweigh the gain in stored solar thermal energy. Although it is difficult to exactly pinpoint this occurrence, Figure 6.18 can assist in the judgement thereof.

Figure 6.18a assesses the former perspective by plotting the Carnot battery's lifetime[25] cost and stored energy (normalised about their maximums), against the TES capacity, for $H_{\text{cap}} = 0$. Lifetime costs increase steadily with t_{TES}. However, stored energy initially increases considerably with t_{TES}, but stabilises at larger capacities. Figure 6.18b plots the derivative of Figure 6.18a. Here, the rate of stored energy gained with larger t_{TES} plummets towards zero for

---

[25] "Lifetime" variables represent the sum of discounted values across the plant lifetime to the present year.

$t_{\text{TES}} > 10$ hours. Based on purely storing solar thermal energy, it is unlikely to obtain economic solar thermal TES sizing at $\geqslant 10$ h, as the rate of stored solar thermal energy gained is poor compared to the cost increase. In fact, the TES capacities on the LCOE-LCOS Pareto curve are between 5 h to 8 h.

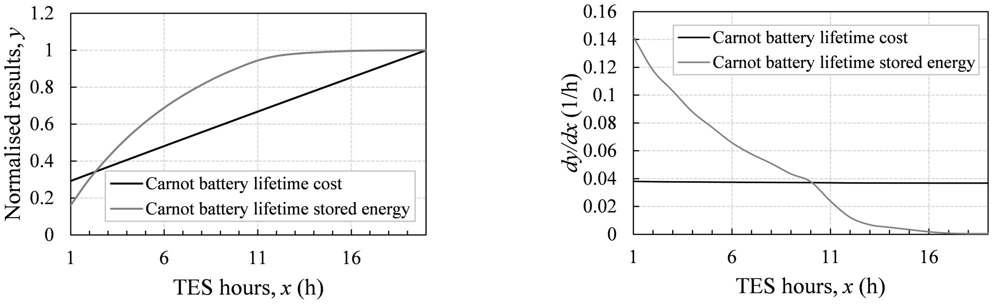

(a) Normalised results vs. t_{TES}.

(b) dy/dx vs. t_{TES}.

Figure 6.18: Carnot battery lifetime parameters vs. t_{TES} for $H_{\text{cap}} = 0$.

The function or purpose of the CSP plant also influences the appropriate storage capacity. Plants targeting peaking periods typically have smaller TES capacities (Poole, 2017; Lovegrove *et al.*, 2018). According to Pan (2020), Kathu intentionally targets peaking periods to maximise profit. Therefore, it does not require a larger TES capacity (and perhaps solar field) which would give baseload-like generation (Poole, 2017).

In contrast, Bokpoort CSP with a 9.3 hour TES capacity operates as a baseload plant. This is primarily ascribed to Bokpoort being awarded in BW2 (bid window) under the REIPPPP (Renewable Energy Independent Power Producer Procurement Programme) with a uniform or flat TOD remuneration structure, whereas Kathu was awarded in BW3.5. BW3.5 comprises of a two-tier TOD tariff structure to incentivise high-demand period power generation, with no remuneration during the night (Pan, 2020). Its peak period lasts for five hours (Poole, 2017), which is comparable to Kathu's TES capacity.

Once a Carnot battery, why is the compromise t^*_{TES} (Table 6.2) lower than that expected for baseload generation, as prioritised by the computational plant? It is presumed that the definition of what constitutes an optimum TES capacity changes once heater capacity is integrated (the latter perspective).

Figure 6.19 depicts two distinct curves worth considering: the plateauing curve, E_0, shows the system's stored energy-cost relationship obtained from increasing t_{TES} with $H_{\text{cap}} = 0$ (i.e. for a conventional CSP plant without RE import). The family of outward-extending diagonal curves plot the stored energy-cost relationship for added H_{cap} at different t_{TES}'s. "Lifetime cost" considers capital and operational costs specific to the TES, power cycle and heater blocks, over the plant lifetime, discounted to the present value (LCOS numerator).

"Lifetime stored energy" is the total stored energy over the plant lifetime, discounted to the present value. The optimum investment in TES capacity (t^*_{TES}) to which heater capacity should be added, emerges as the curve E_1 that contains a point of tangency with E_0, such that $dE_0/dC_l \approx dE_1/dC_l$ at t^*_{TES}.

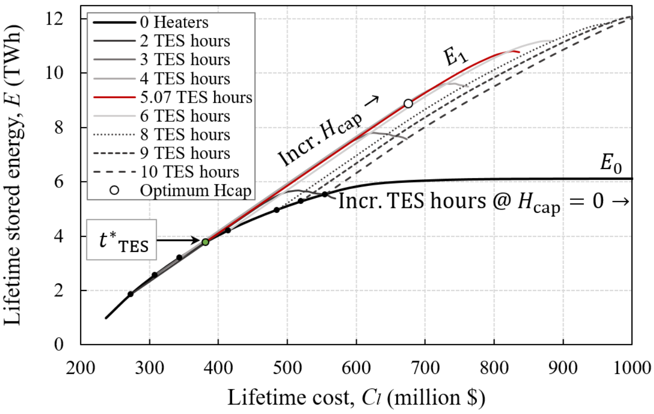

Figure 6.19: Carnot battery lifetime stored energy vs. cost as $f(t_{\text{TES}}, H_{\text{cap}})$.

Thus, to improve the CF and LCOS, it is best to add heaters at a $t^*_{\text{TES}} \approx$ 5.07 hour capacity to guarantee essentially the largest gain in stored energy for the same cost over the storage system's lifetime (for the given SM). Furthermore, Figure 6.19 shows in general that a lower t_{TES} fitted with more H_{cap} can store the same quantity of energy at a reduced cost than a higher t_{TES} fitted with less H_{cap}. A similar observation is highlighted in Gedle *et al.* (2020).

Some leniency exists towards t^*_{TES} near the region of tangency (small H_{cap}). The diagonals possess strong linearity near E_0. This decreases slightly towards larger H_{cap}, and more greatly for larger t_{TES}. The sensitivity of compromise MOO towards scaling should also be kept in mind when assessing Figure 6.19's exactness in corroborating the optimisation results.

The point of tangency along E_0 will differ depending on the stored energy-cost characteristics of the battery. Less efficient heaters, although installed at the same H_{cap}, will contribute less energy to storage at the same variable and capital costs during operation. As a result, the slope of the diagonals decreases, which locates the point of tangency at a larger t_{TES}. Intuitively this is clear: a Carnot battery with a sub-efficient heater block favours a larger solar thermal contribution (a larger t_{TES}) to compensate for the RE purchased, but lost through heater inefficiencies. Logically, less efficient heaters will also result in a larger $\hat{H}_{\text{cap}}(t_{\text{TES}})$ in Figure 6.14. That is the onset of overcharge is delayed.

If the actual charging costs are more expensive than that assumed in the model, and assuming 100 % efficient heaters, the diagonal slopes will decrease for the same quantity of stored energy (this does not alter Figure 6.14 though). As such, the point of tangency also shifts to larger TES capacities. It is noted that according to Section 6.6, larger TES capacities will correspond to lower installed heater capacities at the point of overcharge.

The value of Figure 6.19 is the fact that extensive parametric analyses (as in Figure 6.7) are no longer required to determine a fair value for t^*_{TES}. This is often the default optimisation approach in literature. Instead, knowledge of E_0 and the Carnot battery's stored energy-cost relationship, from integrating H_{cap} at a given T_{set}, can reveal t^*_{TES} with less effort.

6.11 Other Techno-economic Considerations

Other important techno-economic results are presented for the optimised Carnot battery. These are: the storage temperatures (an indirect constraint) (Section 6.11.1), round-trip efficiency (Section 6.11.2), cost (Section 6.11.3) and energy (Section 6.11.4) allocations and TOU/TOD considerations (Section 6.11.5).

6.11.1 Storage Temperatures

The hot and cold tank average HSF temperatures are assessed in Figure 6.20.

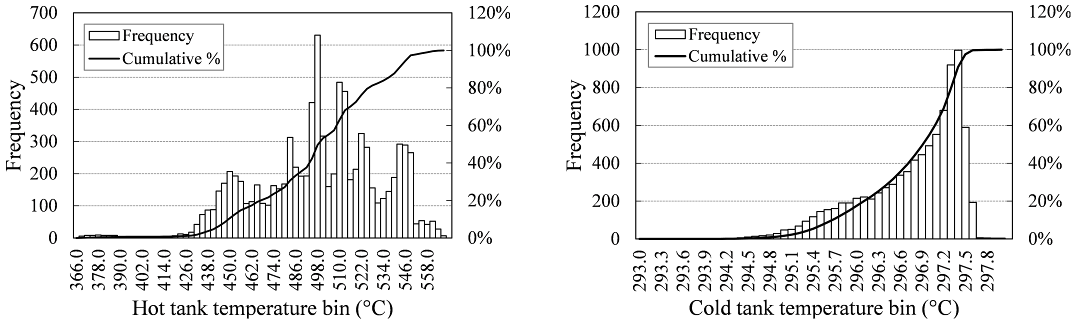

(a) Hot tank.

(b) Cold tank.

Figure 6.20: Tank average temperature distributions.

A prevalent limitation of molten salt is the onset of freezing and thermal decomposition at its lower and upper temperature limits (Lovegrove and Stein, 2012). Hitec solar salt (considered as HSF in this thesis) can operate up to 593 °C, but is typically limited to 565 °C when stored (Heller, 2013). Storage tanks operating at higher temperatures would be constructed from more expensive materials, as the corrosivity of the molten salt increases with temperature (Lovegrove and Stein, 2012).

According to NREL (2020*b*), Hitec solar salt has a minimum operating temperature of 238 °C, 16 °C above its freeze-point temperature (Heller, 2013). Therefore, hourly average hot and cold tank molten salt temperatures of the optimised system should be confined to 238 °C $\leqslant \overline{T}^{t}_{h/c} \leqslant$ 565 °C during a typical year.

Hot tank temperatures are located well above the minimum operating temperature, and nearly 100 % below 565 °C. All cold tank temperatures are located above the minimum operating temperature, and rightly below 565 °C. No auxiliary heating is required in either tanks. Consequently, the temperature control strategy outlined in Section 4.2.8.1 is deemed an appropriate one.

6.11.2 Round-trip Efficiency

Round-trip efficiency is a common performance indicator when comparing different storage technologies (Enescu *et al.*, 2020; Dumont *et al.*, 2020; Denholm *et al.*, 2021). As with LCOS, a single definition of round-trip efficiency does not exist; it varies depending on the storage technology (Brun *et al.*, 2020). In this thesis, the round-trip efficiency is defined by Equation 4.2.35. Parametric results are presented in Figure 6.21 for $T_{\text{set}} = T^{*}_{\text{set}} = 586$ °C.

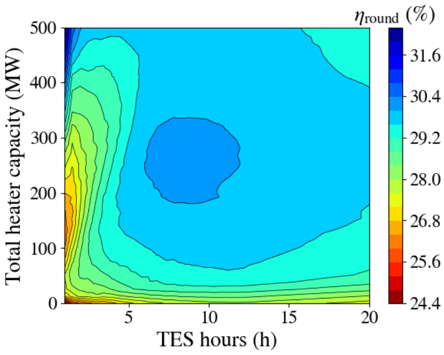

Figure 6.21: Round-trip efficiency parametric analysis.

Two distinct regions are observed around one to two hours: a region of low η_{round} from $H_{\text{cap}} \approx 0\,\text{MW}$ to $250\,\text{MW}$, transitioning into higher efficiency up to 500 MW. In theory, it is more efficient to store a larger thermal charge (therefore higher $\overline{T}_h$) in a smaller space with minimal surface area. A combination of a large installed H_{cap} and small TES capacity (considering Equation 4.2.21) can provide that. Conversely, a lower thermal charge (accompanied by lower H_{cap} and $\overline{T}_h$) results in poorer conversion of stored energy into net electrical energy. In general, η_{round} is low regardless of TES capacity near $H_{\text{cap}} = 0$. The optimum design (Table 6.2) occurs near the circular region of "second-best" η_{round}, as the global minimum η_{round} presents an infeasible design.

An unfortunate drawback of TES Carnot batteries is the overall low round-trip efficiency compared to PV with battery storage (Schöniger *et al.*, 2020), such as Li-ion (Section 2.5). The strongest penalisation occurs within the power cycle, where thermal efficiency ranges between 0 % to 34.7 % ($\eta_{\mathrm{th}} = 0$ % during power cycle shutdown). The TES discharge-to-charge ratio is generally high, around 96.6 % (Equation 4.2.34), as is the power cycle gross-to-net conversion rate at 92.8 % (Equation 4.2.19).

The optimum capacity of installed heaters could be reminiscent of a plant with a sub-optimal solar thermal contribution for baseload generation, due to seasonal effects, an undersized SM, undersized TES or excessive solar thermal curtailment. (As such, Section 6.12 considers increasing the solar thermal contribution and studying its effect on the Carnot battery's performance.) Purchasing RE on this scale is expensive (Section 6.11.3) and a likely incentive for the LCOE preferring a low H_{cap} (Figure 6.7b). It is sensible that charging costs should be reduced, as considered in Figures 6.4 and 6.8, to counteract the low η_{round} and thereby improve the LCOE. The value of the Carnot battery in the price arbitrage space should also be considered. This can amplify revenue by purchasing off-peak RE at a low tariff, with electricity sales at a higher peak price. Unfortunately, the LCOE does not convey this value.

6.11.3 Expenditures

A breakdown of the current price[26] capital and variable expenditures is provided in Figure 6.22.

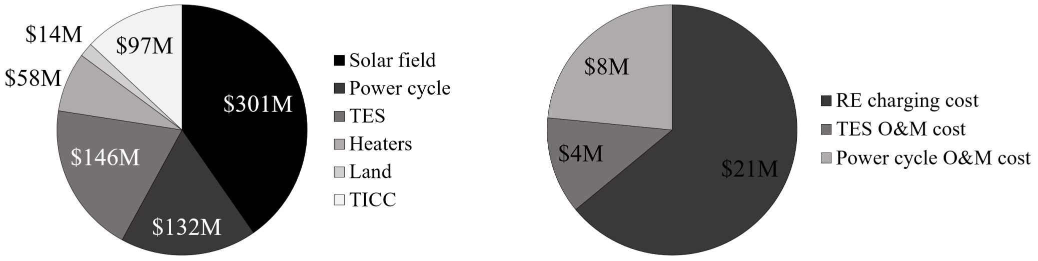

(a) Plant capital costs.

(b) Battery-specific variable costs.

Figure 6.22: Cost analysis of the optimised CSP Carnot battery.

Regarding capital costs (Figure 6.22a), the solar field presents the largest investment in the parabolic trough plant, followed by TES and the power cycle. The cost components agree with typical ranges in literature: the solar field representing 35 % to 49 % of the total installed cost, the TES at 9 % to 20 %, the power cycle at 14 % to 21 % and the total indirect capital cost at 3 % to 16 % (IRENA, 2012). Land costs can occupy up to 2 % according to Hinkley *et al.* (2011). The heater block occupies roughly 7.8 % of the total installed capital cost for the optimised plant.

---

[26] I.e. non-discounted annual cash outflows.

Figure 6.22b analyses the optimised Carnot battery's annual variable costs (the constituents of Equation 4.2.53). The cost of purchasing RE (annual sum of Equation 4.2.64) exceeds other variable costs, at 63.6 % of the total. Carnot battery power cycle O&M costs (Equation 4.2.55) occupy 24.2 % and TES O&M costs (Equation 4.2.54) 12.1 %. The discounted cost of purchased RE over the plant's lifetime equates to roughly $218M, 3.76 times more expensive than the capital investment into the heater block. The cost of purchasing grid electricity in the MW range typically exceeds the associated electric heater capital cost (McKechnie *et al.*, 2020).

6.11.4 Energy Allocation

In Figure 6.23a, imported RE occupies the greatest share (57.6 %) of the annual stored thermal energy. This majority share stems from the LCOS and CF maximising electricity generated from TES by importing more RE. This is because there is a limit to the quantity of solar thermal energy which can be stored economically, especially with the integration of H_{cap} (Section 6.10). Considering the net electrical power produced in Figure 6.23b, 71 % is derived from solar thermal energy. Therefore, 29 % of electricity is generated from imported RE. Roughly 32.6 % of imported RE is converted into net electricity.

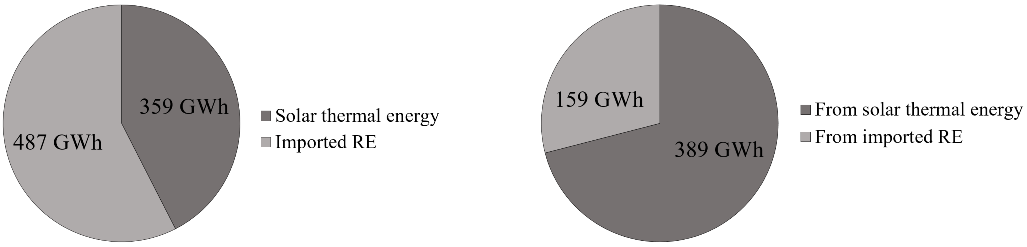

(a) Thermal energy storage.

(b) Net electricity generation.

Figure 6.23: Annual energy breakdown of the optimised CSP Carnot battery.

6.11.5 Time-of-use and Time-of-delivery

It is quantified to which extent the standard solar thermal charge-discharge cycles of the optimised CSP Carnot battery are equipped to facilitate time-shifting of imported RE. "Ideal" time-shifting occurs when solar thermal charge cycles allow RE to be charged solely during daytime off-peak periods (central daylight hours). Discharge is shifted to the evening peak, nighttime hours and perhaps a portion of the morning peak. Peak-purchased RE is more expensive and also consumes renewable electricity otherwise required to sustain or supply the peak. In essence, this defeats the objective of the Carnot battery, which is to store RE during lower demand and off-peak periods on the grid.

Following this, the Megaflex structure in Figure 4.11 is employed to measure the frequency of RE charging (import) cycles interfering and discharge cycles coinciding with the total peak periods in a year. Central daylight (off-peak) periods are also established based on the Megaflex structure. The solar angle calculator developed by Stine and Geyer (2001) is implemented to develop a hourly structure for day and nighttime hours for each month of the year at Kathu. This is implemented to measure the frequency of discharge cycles coinciding with total hours after sunset. The results are presented in Table 6.3.

Table 6.3: Carnot battery TOU and TOD frequency analysis.

	Time of day	**RE charge cycles**	**TES discharge cycles**
(1)	Morning + evening peak	13.13 %	28.82 %
(2)	Morning peak	13.28 %	4.22 %
(3)	Evening peak	12.88 %	72.74 %
(4)	Central daylight hours	68.95 %	8.04 %
(5)	After sunset	9.5 %	61.78 %

A greater portion of TES discharging coincides with a morning and evening peak than RE charging (1). RE charging is near equally likely to interfere with a morning or evening peak, whereas TES discharge cycles are clearly more centred around evening peaks (2 & 3). RE charging strongly coincides with central daylight hours, with TES discharge cycles in the minority (4). After sunset, RE charging is infrequent relative to TES discharging (5). Based on the overall results, it can be argued that the natural solar thermal charge-discharge cycles of the parabolic trough CSP plant promote time-shifting of RE. Arguably, dispatch optimisation could enhance this service even further.

Next, the MOO of Section 6.7 is re-applied with RE charging restricted to central daylight off-peak periods and TES discharge restricted to after-sunset hours. These restrictions should enhance the time-shifting of RE. An updated tipping-point constraint is calculated according to Figure 6.14's methodology:

$$\hat{H}_{\text{cap}}(t_{\text{TES}}) = 0.7015t_{\text{TES}}^3 - 10.702t_{\text{TES}}^2 + 8.4376t_{\text{TES}} + 319.75 \quad (R^2 = 1) \quad (6.11.1)$$

MOO yields $t_{\text{TES}} = 4.23$ hours, $H_{\text{cap}} = 216.75$ MW and $T_{\text{set}} = 586$ °C. Compared to Table 6.2, it is apparent that the optimum TES and heater capacities have decreased, indicative of a plant with a lower demand for RE and TES due to restricted TOU (RE charging) and TOD (TES discharging) periods.

Compared to the unrestricted optimised case in Table 6.2, the LCOS increases by 1.01 ¢/kWh, the LCOE decreases by 0.22 ¢/kWh, as does the CF by 5.17 percentage points. Repeating an exercise of Figure 6.19's nature confirms ≈ 4.23 hours as the optimum TES capacity for heater addition in the restricted case. With TOD restricted, the potential for TES overcharge is more severe. Lower UF's are observed with UF tipping points shifting towards lower H_{cap}.

6.12 Optimised Solar Field Size

The solar field size is optimised to comprehend the CSP Carnot battery's response to an increased share of solar thermal energy. Emphasis is placed on the change in interplay between stored solar thermal energy and imported RE, as well as the optimum TES capacity for heater allocation.

6.12.1 Procedure

With the SAM benchmark model, a parametric analysis is run between SM and t_{TES}. LCOE is the selected objective function, as shown in Figure 6.24. The benchmark TES capacity and SM is [4.5 hours, 2.6]. The optimum SM and TES capacity increases to $[t^*_{\text{TES}}, SM^*] = [11.513 \text{ hours}, 3.666]$ for a minimum LCOE of 10.26 ¢/kWh (standard deviation in LCOE* $= 1.2 \times 10^{-7}$ ¢/kWh across runs). Seeing that the field size changes from that of the benchmark, the relevant time-varying performance model inputs are re-calculated in SAM.

Figure 6.24 traces a valley by incrementally fixing t_{TES} and locating SM*. In accordance with Poole (2017); Gedle *et al.* (2020), the trace confirms that larger TES capacities favour larger SM*'s. As the power cycle's nameplate capacity and therefore design thermal input remains unaltered, the share of surplus solar thermal energy increases with SM. To utilise the larger surplus, the optimum TES capacity increases accordingly.

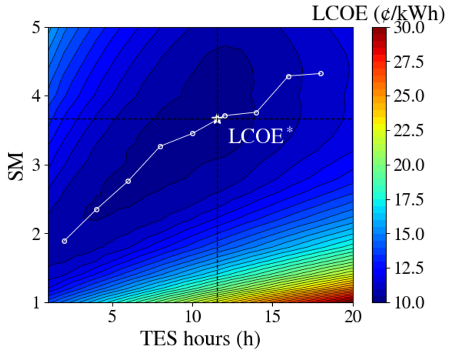

Figure 6.24: Optimisation of $LCOE(t_{\text{TES}}, SM)$.

6.12.2 Response Observations

An increased solar thermal share of stored energy notably alters the Carnot battery's response, as depicted in Figure 6.25. Here "response" considers the UF curves as a function of TES and installed heater capacities (Figure 6.25a), as well as stored energy-cost curves used to determine the optimum TES capacity for integrating heater capacity (Figure 6.25b).

Due to the increased share of solar thermal energy, the TES system becomes more prone to RE overcharge for the same t_{TES} and H_{cap} when compared to the unoptimised field case. This is observed in Figure 6.25a. The UF's are overall lower when compared to the unoptimised field case (Figure 6.14). In addition, the minimum tipping displacement shifts to a lower H_{cap}, as do the tipping points in general. As a result, tipping-point constrained optimisation will yield lower H^*_{cap}'s. Therefore, a plant with a larger solar field and thus a greater share of surplus solar thermal energy has less capacity for optimally allocated heaters. A larger nameplate capacity can possibly mitigate this.

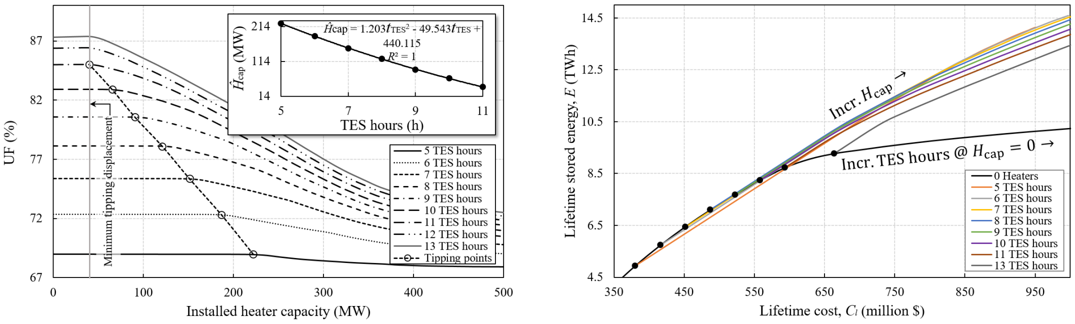

(a) UF tipping points.

(b) Energy-cost curves.

Figure 6.25: Carnot battery response to increased solar thermal energy.

Hence the predicament from Figure 6.24 is this: parabolic trough plants are optimally designed along the locus of local minimum LCOE's up to LCOE*. This entails increasing t_{TES} and the SM. Deduced from Section 6.6, a larger TES capacity can accommodate less heater capacity to avoid RE overcharge. It is also exacerbated by the increased surplus solar thermal energy due to larger SM's. This can be an inherently conflicting barrier to technical synergy.

Energy-cost curves (Figure 6.25b) are no longer as straightforward in this case. Figure 6.19 suggests a near single optimum TES capacity for heater addition (for all feasible lifetime costs). However, Figure 6.25b suggests different optimum TES capacities that are more dependent on the intended range of installed H_{cap}. This is due to the fact that the diagonals are no longer linear at lower lifetime costs as the share of field solar thermal energy is increased. This shift is most likely attributed to TES overcharge occurring much earlier, owing to the increased share of solar thermal energy sent to TES.

The optimum TES capacities for heater addition are generally larger compared to results for the unoptimised solar field case. Majority of newly built CSP plants employ a two-tank molten salt TES system with an average capacity of 9.3 hours (Schöniger *et al.*, 2020). Therefore, a system with larger TES capacity and some added heater capacity could be more representative of industry trends. Hence, this could favour the optimised solar field case. Such a system also strengthens baseload power generation (higher CF's are observed).

Chapter 7

Conclusion

The purpose of this thesis is the techno-economic assessment as well as optimisation of a Carnot battery application in a CSP plant. In this chapter, the main findings and contributions of the thesis are summarised. The extent to which the research objectives and questions (Section 3.2) are met is also examined and the results thereof summarised. Lastly, the limitations of this research are considered and suggestions for future research are provided.

7.1 Concluding Remarks

Chapter 4 addresses objective 1 by documenting the formulation of a techno-economic computational model for a conventional parabolic trough CSP plant applied as a Carnot battery. During solar thermal charge cycles, resistive heaters import renewable electricity from the grid, which is stored as thermal energy in the CSP plant's TES system. This boosts the solar thermal charge cycle. The plant discharges stored thermal energy to promote baseload power generation at a fixed 100 MW nameplate capacity. The model is validated internally, via energy and mass balances, and to an external SAM benchmark model. Overall, validation results are deemed to be satisfactory.

Chapter 5 argues for the MOO of the CSP Carnot battery, as this can unlock additional insights into what constitutes an optimum design and why. A framework for the MOO of the CSP Carnot battery is developed (objective 5a). It rests on the principles of Pareto frontiers. The utopian point selection method, when coupled with PSO, facilitates the selection of a compromise Pareto optimal solution from the frontier P. However, compromise optimal solutions are subject to $P \in$ attainable $\mathbf{Z}$. Solutions in attainable $\mathbf{Z}$ are those corresponding to $\mathbf{x} \in \mathbf{S}$, the feasible design space $\subseteq \mathbf{D}$. Attainable points are not necessarily Pareto optimal points.

Chapter 6 contains the investigation into the majority of Section 3.2's objectives and questions. The Carnot battery's techno-economic response to design and economic parameter changes (objective 2) is established in Section 6.2 and 6.3. Among others, a key finding (objective 2a) is that unlike the LCOS and CF, the LCOE does not readily favour the integration of heater capacity (Figures 6.1 and 6.7). A sensitivity study reveals that the economic metrics are strongly influenced by the RE charging cost (Section 6.3). A reduction in the RE charging tariff not only promotes the integration of heater capacity at a given set-point temperature and optimum TES capacity (Figure 6.8), it also governs the very definition of what constitutes an economically optimal heater set-point temperature (Figure 6.4). This is not necessarily the same as the thermodynamic optimum set-point temperature (Figures 6.1c, 6.6c and 6.7c).

The uncertainties surrounding RE charging costs can introduce barriers to economic synergy (objective 2b). However, the technical value and grid-scale service potential of the CSP plant, especially once applied as a Carnot battery, is evident. With the integration of heater capacity, around-the-clock power generation is considerably enhanced (objective 4b). By studying CF response surfaces, it is evident that CSP Carnot batteries are technically (in a thermodynamic sense) apt for baseload power generation. Increased CF's can enhance the continuity of inertial support and suppress the intermittency of CSP. From an operational perspective, a proposition regarding CSP's inherent suitability to substitute conventional fossil-fueled baseload plants is a valid one. This is especially true for South Africa, a country with abundant solar resource and retiring coal plants.

This thesis considers two grid scale services sought for mass RE integration, namely RE time-shifting and inertial support. The standard solar thermal charge-discharge cycles of the TES subsystem promote the time-shifting of grid-scale quantities of solar PV (Figure 6.10 and Table 6.3). With the integration of heater capacity, potentially surplus and off-peak grid RE is stored and converted back to electricity during higher demand and nighttime periods. This is a desired attribute of utility-scale storage technologies in a power system at risk of the duck curve (objective 4a). Data shows that CSP's time-shifting service attains stronger potential during summer than winter (Section 6.5).

CSP is uniquely positioned as a RE technology in providing inherent inertial support to the grid. Once applied as a Carnot battery, the system can be sized to enhance the continuity of this support. This is evident when viewing the aforementioned CF response surfaces together with Figure 6.11. The CSP Carnot battery essentially transforms "inertaileess" solar PV generation into power generated with inertia (objective 4a).

The Carnot battery application introduces operational trade-offs in the CSP plant (objectives 3a and 3b). This primarily stems from the interplay between stored imported RE and solar thermal energy (Section 6.6). Depending on the heater capacity, TES overcharge can occur (Figure 6.14). This indicates an oversized heater capacity. Higher charge states are obtained which cannot be drained completely during subsequent discharge cycles. The hot tank retains a residual charge which reduces the intake capacity of a subsequent solar thermal charge cycle. As a result, solar thermal energy is unnecessarily curtailed.

Analyses suggest an inverse relationship between the TES capacity and installed heater capacity at the onset of overcharge. That is, a larger TES capacity can accommodate less installed heater capacity before overcharge occurs, and *vice versa*. When the solar field size is increased (Section 6.12), the onset of TES overcharge shifts to even lower installed heater capacities (Figure 6.25a). Therefore, parabolic trough CSP plants with lower SM's display greater potential to optimally sustain heater integration for a Carnot battery application. This could constitute a barrier to technical or operational synergy between a CSP plant and its Carnot battery counterpart (objective 3b).

Pertaining to objective 5b, the selection of LCOS, LCOE and CF as Carnot battery performance metrics is motivated in Section 6.1. A Pareto analysis (Section 6.9) further shows that because $\mathbf{DM} > \mathbf{0}$, these objectives are conflicting in nature and do not lead to redundancy in the optimisation of $\mathbf{F}$. As such, they are appropriate objective functions for the MOO. Furthermore, the LCOE-CF trade-off dominates the full unconstrained MOO problem.

In the MOO with trade-offs of a nature $DM_{f_k} \ll DM_{f_{k+1}}$, the former objective can endure a relatively small sacrifice for a larger improvement in the latter. The objective with a larger DM is then located closer to its utopian component, whereas the objective with a smaller DM is closer to its nadir component. This is evident in the 3D unconstrained LCOE-LCOS and LCOS-CF Pareto fronts, which are governed by the LCOE-CF front. Constrained designs ($\mathbf{x} \in \mathbf{S}$) yield compromise solutions not necessarily on the Pareto frontier.

Regarding objective 5c, it is determined that the optimum TES capacity for heater addition is not necessarily the purely solar thermal optimum capacity (Section 6.10). Instead, the former can be reasonably located as the curve with a point of tangency on the Carnot battery's stored energy-cost graph (Figure 6.19). This is also in line with the optimum TES capacity returned by the compromise MOO (Table 6.2). This TES capacity yields the greatest return in stored energy (solar thermal and imported RE) for the additional costs incurred with heater integration. With increased shares of solar thermal energy at larger SM's, a single optimum TES capacity for heater integration becomes less apparent (Figure 6.25b). Instead, the optimum TES capacity is much more dependent on the intended range of installed heater capacity.

Lastly, other techno-economics are considered. The storage temperatures conform to acceptable ranges for molten salt storage inside stainless steel tanks (Section 6.11.1). The round-trip efficiency (Figure 6.21), largely impeded by the power cycle thermal efficiency, is much lower than competitive Li-ion battery energy storage technologies. A cost breakdown (Section 6.11.3) shows that the heater block occupies a relatively small fraction of all capital expenditures. However, charging costs dominate variable expenditures. An energy breakdown (Section 6.11.4) indicates that roughly 32.6 % of stored RE is converted into electricity, perhaps an unfortunate outcome when considering the substantial charging costs.

In closing, this thesis aims to provide a fundamental techno-economic understanding of the conventional parabolic trough CSP Carnot battery. It cannot indisputably confirm, nor deny the feasibility of the technology. Various factors should be considered in reaching such a conclusion. These are beyond the scope of the current, but not necessarily future, research. This thesis emphasises the CSP Carnot battery technology's potential strengths, shortcomings and underlying principles as a stepping stone towards reaching that conclusion.

7.2 Limitations of this Research

This research encounters many uncertainties that are simplified into assumptions. Uncertainties are especially prevalent in the long-term assumptions made throughout the plant's lifetime. Furthermore, the results are only for a single meteorological case at Kathu. Different, or new conclusions might be drawn for regions with better or poorer solar resource. It is submitted that this work is not intended as a detailed design of a CSP Carnot battery in terms of exhaustive component-level or financial modelling and analyses. Such an approach would provide even less scope than already exists to address the end research objectives and questions. Therefore, when considering the results, the reader should be cognisant of the uncertainties and assumptions involved.

7.3 Potential for Future Research

The results of this thesis can serve as a foundation for future research. To this end, suggestions and questions are summarised:

1. Investigate the application of a CSP Carnot battery as a load-following plant. How does this compare, technically and economically, to the baseload scenario?
2. Investigate technical strategies to mitigate TES overcharge with the storage of RE (for example, larger nameplate capacities). How can RE be stored with less detriment to the UF? Can this be done economically?
3. Compare central receiver CSP Carnot batteries to parabolic trough CSP Carnot batteries on a techno-economic basis;
4. As baseload coal-fired plants are decommissioned in South Africa, what substituting role can CSP Carnot batteries play in this field?
5. Assess a system more similar to the Midelt project: daytime surplus solar PV boosting TES, with power generated from TES only, after sunset.

List of References

Akhil, A., Huff, G., Currier, A., Kaun, B., Rastler, D., Chen, S., Cotter, A., Bradshaw, D. and Gauntlett, W. (2015). DOE/EPRI electricity storage handbook in collaboration with NRECA. Report, Sandia National Laboratories.

Akinyele, D. and Rayudu, R. (2014). Review of energy storage technologies for sustainable power networks. *Sustainable Energy Technologies and Assessments*, vol. 8, pp. 74–91.

Alva, G., Lin, Y. and Fang, G. (2018). An overview of thermal energy storage systems. *Energy*, vol. 144, pp. 341–387.

Antonelli, M., Barsali, S., Desideri, U., Giglioli, R., Paganucci, F. and Pasini, G. (2017). Liquid air energy storage: Potential and challenges of hybrid power plants. *Applied Energy*, vol. 194, pp. 522–529.

Antúnez, P. (2015). *Modelling of thermal energy storage systems for bulk electricity storage*. PhD, Cambridge University.

Argyrou, M., Christodoulides, P. and Kalogirou, S. (2018). Energy storage for electricity generation and related processes: Technologies appraisal and grid scale applications. *Renewable and Sustainable Energy Reviews*, vol. 94, pp. 804–821.

Arora, J. (2012). *Introduction to optimum design*. 4th edn. Academic Press, London. ISBN 978-0-12-800806-5.

Auret, C. (2015). *Scenario modelling for short to long term rollout of concentrating solar power in South Africa*. Masters Thesis, Stellenbosch University, Department of Mechanical and Mechatronic Engineering.

Barnes, R. (2017). *Performance modelling, validation and operational feasibility of a parabolic trough power plant*. Masters Thesis, Stellenbosch University, Department of Mechanical and Mechatronic Engineering.

Biswas, D., Bose, S., Dalvi, V., Deshmukh, S., Shenoy, N. and Panse, S. (2020). A techno-economic comparison between piston steam engines as dispatchable power generation systems for renewable energy with concentrated solar harvesting and thermal storage against solar photovoltaics with battery storage. *Energy*, vol. 213.

Black, M. and Strbac, G. (2006). Value of storage in providing balancing services for electricity generation systems with high wind penetration. *Journal of Power Sources*, vol. 162, pp. 949–953.

Blaga, R. and Paulescu, M. (2018). Quantifiers for the solar irradiance variability: a new perspective. *Solar Energy*, vol. 174, pp. 606–616.

Brouwer, A., Van Den Broek, M., Seebregts, A. and Faaij, A. (2014). Impacts of large-scale intermittent renewable energy sources on electricity systems, and how these can be modeled. *Renewable and Sustainable Energy Reviews*, vol. 33, pp. 443–466.

Brun, K., Allison, T. and Dennis, R. (2020). *Thermal, mechanical, and hybrid chemical energy storage systems.* London: Academic Press, an imprint of Elsevier. ISBN 978-0-12-819892-6.

CAISO (2013). What the duck curve tells us about managing a green grid. Facts sheet, California Independent System Operator.
Available at: `http://large.stanford.edu/courses/2015/ph240/burnett2/docs/flexible.pdf`

Calitz, J. and Wright, J. (2021). Statistics of utility-scale power generation in South Africa. Conference presentation slides.

Carson, R. and Novan, K. (2013). The private and social economics of bulk electricity storage. *Journal of Environmental Economics and Management*, vol. 66, pp. 404–423.

Castillo, A. and Gayme, D. (2014). Grid-scale energy storage applications in renewable energy integration: a survey. *Energy Conversion and Management*, vol. 87, pp. 885–894.

Çengel, Y. and Boles, M. (2015). *Thermodynamics: an engineering approach.* 8th edn. McGraw-Hill Education, New York.

Chiandussi, G., Codegone, M., Ferrero, S. and Varesio, F. (2012). Comparison of multi-objective optimization methodologies for engineering applications. *Computers and Mathematics with Applications*, vol. 63, pp. 912–942.

Church, E. (1935). *Steam turbines.* 2nd edn. McGraw-Hill Book Company, New York & London.

Correia, C., Flynn, D., Uliana, E., Wormald, M. and Dillon, J. (2015). *Financial management.* 8th edn. Juta & Company, Cape Town. ISBN 9781485104902.

De Klerk, B. (2015). STERG symposium presentation. Presentation slides.

Denholm, P., Cole, W., Frazier, A., Podkaminer, K. and Blair, N. (2021). The four phases of storage deployment: a framework for the expanding role of storage in the U.S. power system. Tech. Rep., National Renewable Energy Laboratory.

Denholm, P., Mai, T., Kenyon, R., Kroposki, B. and O'Malley, M. (2020). Inertia and the power grid: a guide without the spin. Technical report, NREL.
Available at: `https://www.nrel.gov/docs/fy20osti/73856.pdf`

Denholm, P., O'Connell, M., Brinkman, G. and Jorgenson, J. (2015). Overgeneration from solar energy in California: a field guide to the duck chart. Technical report, National Renewable Energy Laboratory.

Department of Energy (2019). Integrated Resource Plan 2019. Document, Department of Energy - Republic of South Africa.

Department of Energy: Republic of South Africa (2010). IRP input parameters [Online]. Available: http://www.energy.gov.za/IRP/irp%20files/IRP%20Parameter%20-%20S3%20Discount%20Rate.pdf [2021-07-10].

Donga, R. and Kumar, S. (2019). Thermal performance of parabolic trough collector with absorber tube misalignment and slope error. *Solar Energy*, vol. 184, pp. 249–259.

Dumont, O., Frate, G., Pillai, A., Lecompte, S., De Paepe, M. and Lemort, V. (2020). Carnot battery technology: a state-of-the-art review. *Journal of Energy Storage*, vol. 32.

Dumont, O. and Lemort, V. (2020). Mapping of performance of pumped thermal energy storage (Carnot battery) using waste heat recovery. *Energy*, vol. 211.

Enescu, D., Chicco, G., Porumb, R. and Seritan, G. (2020). Thermal energy storage for grid applications: Current status and emerging trends. *Energies*, vol. 13, no. 2.

Eskom (2017). Eskom 2018/19 revenue application - NERSA public hearings, Kimberley. Presentation slides.

Eskom (2018). Integrated demand management programme. Fact sheet, Eskom. Available at: `https://www.eskom.co.za/CustomerCare/IDM/Pages/IDM.aspx`

Eskom (2019). Schedule of standard prices for Eskom tariffs 1 April 2019 to 31 March 2020 for non-local authority supplies, and 1 July 2019 to 30 June 2020 for local authority supplies [Online]. Available: https://www.eskom.co.za/CustomerCare/TariffsAndCharges/Documents/Eskom%20schedule%20of%20standard%20prices%202019_20%20Rev00%20(full%20version%20excl%20Transflex).pdf [2020-07-04].

Eskom (2020). Megaflex gen and Ruraflex gen [Online]. Available: https://www.eskom.co.za/CustomerCare/TariffsAndCharges/WhatsNew/Pages/Genflex.aspx [2020-07-04].

Eskom (2021*a*). Data request form [Online]. Available: https://www.eskom.co.za/dataportal/data-request-form/ [2021-09-07].

Eskom (2021*b*). Tariff history. [Online]. Available: https://www.eskom.co.za/CustomerCare/TariffsAndCharges/Pages/Tariff_History.aspx [2021-06-06].

Eskom (2021*c*). Tariffs and charges [Online]. Available: https://www.eskom.co.za/CustomerCare/TariffsAndCharges/Pages/Tariffs_And_Charges.aspx [2021-07-10].

EXHEAT (2020). Electric process heater. Quotation form, reference no. ENQ/20/Q4043.

EXHEAT (2021). Process heaters for high temperature applications [Online]. Available: http://www.exheat.com/products/catalogue/high-temperature-applications [2021-01-04].

Fan, X., Liu, B., Liu, J., Ding, J., Han, X., Deng, Y., Lv, X., Xie, Y., Chen, B., Hu, W. and Zhong, C. (2020). Battery technologies for grid-level large-scale electrical energy storage. *Transactions of Tianjin University*, vol. 26, pp. 92–103.

Farmer, W. and Rix, A. (2020). Optimising power system frequency stability using virtual inertia from inverter-based renewable energy generation. *The Institution of Engineering and Technology Renewable Power Generation*, vol. 14, no. 15, pp. 2820–2829. ISSN 1752-1416.

Feldman, D., Margolis, R., Denholm, P. and Stekli, J. (2016). Exploring the potential competitiveness of utility-scale photovoltaics plus batteries with concentrating solar power, 2015 to 2030. Technical report, National Renewable Energy Laboratory, U.S. Department of Energy.
Available at: `https://www.nrel.gov/docs/fy16osti/66592.pdf`

Flynn, D. (2003). *Thermal power plant simulation and control.* 43rd edn. IEE Power & Energy Series, United Kingdom. ISBN 0852964196.

Fourie, D. (2018). *Assessing the economic feasibility of utility-scale electrical energy storage technologies for South Africa.* Masters Thesis, North-West University, Department of Economics.

Franchini, G., Barigozzi, G., Perdichizzi, A. and Ravelli, S. (2015). Simulation and performance assessment of load-following CSP plants. In: *Third Southern African Solar Energy Conference*, pp. 289–294.

Garcia, E., Ghobeity, A., Totten, M. and Mitsos, A. (2013). Optimal operation of a solar-thermal power plant with energy storage and electricity buy-back from grid. *Journal of Energy*, vol. 51, pp. 61–70.

Gazman, V. (2019). *Renewable energy leasing.* House of the Higher School of Economics. ISBN 978-5-7598-2041-3.

Gedle, Y., Schmitz, M., Gielen, H., Schmitz, P., Herrmann, U., Boura, C., Mahdi, Z., Caminos, R. and Dersch, J. (2020). Analysis of an integrated CSP-PV hybrid power plant. SolarPACES.

Gilman, P. (2020). LCOE in SAM using FCR and single owner financial models. Available: https://sam.nrel.gov/images/web_page_files/sam-lcoe-fcr-vs-cash-flow.pdf.

Glatzmaier, G. (2011). Developing a cost model and methodology to estimate capital costs for thermal energy storage. Technical report, National Renewable Energy Technology.
Available at: `https://www.nrel.gov/docs/fy12osti/53066.pdf`

Global Solar Atlas (2020). Available: https://globalsolaratlas.info/map [2020-05-12].

Google Earth (2021). Google Earth: Kathu Solar Park [Online]. Available: https://www.google.com/earth/versions/ [2021-06-15].

GOV.UK (2021). VAT rates [Online]. Available: https://www.gov.uk/vat-rates [2021-01-04].

Grodzevich, O. and Romanko, O. (2006). Normalization and other topics in multi-objective optimization. In: *Proceedings of the Fields-MITACS Industrial Problems Workshop*.

Gross, R., Heptonstall, P., Anderson, D., Green, T., Leach, M. and Skea, J. (2006). The costs and impacts of intermittency: an assessment of the evidence on the costs and impacts of intermittent generation on the British electricity network. Report, Imperial College London.

Guo, Y., Nan, H., Guan, X. and Wu, L. (2018). Discussion on the over-frequency generator tripping scheme of the power grid. In: *International Conference on Energy, Electrical and Power Engineering*. IOP Publishing.

Hartner, M. and Permoser, A. (2018). Through the valley: the impact of PV penetration levels on price volatility and resulting revenues for storage plants. *Renewable Energy*, vol. 115, pp. 41184–1195.

Hayes, A. (2021). Bid price [Online]. Available: https://www.investopedia.com/terms/b/bidprice.asp [2021-07-31].

Heal, G. (2009). The economics of renewable energy. Working Paper 15081, National Bureau of Economic Research.
Available at: `http://www.nber.org/papers/w15081`

Helios CSP (2020). ENGIE starts operations of Kathu, a 100 MW concentrated solar power plant and one of South Africa's largest renewable energy projects [Online]. Available: https://helioscsp.com/engie-starts-operations-of-kathu-a-100-mw-concentrated-solar-power-plant-and-one-of-south-africas-largest-renewable-energy-projects/ [2021-07-12].

Heller, L. (2013). Literature review on heat transfer fluids and thermal energy storage systems in CSP plants. Tech. Rep., Solar Thermal Energy Research Group, Stellenbosch University.
Available at: `https://sterg.sun.ac.za/wp-content/uploads/2011/08/HTF_TESmed_Review_2013_05_311.pdf`

Hinkley, J., Curtin, B., Hayward, J., Wonhas, A., Boyd, R., Grima, C., Tadros, A., Hall, R., Naicker, K. and Mikhail, A. (2011). Concentrating solar power - drivers and opportunities for cost-competitive electricity. Tech. Rep., CSIRO.
Available at: `https://publications.csiro.au/rpr/download?pid=csiro:EP111647&dsid=DS3`

Hirth, L. (2014). *The economics of wind and solar variability. How the variability of wind and solar power affects their marginal value, optimal deployment, and integration costs.* PhD, Technische Univ. Berlin (Germany). Fakultaet VI - Planen Bauen Umwelt.

Hou, Q., Zhang, N., Du, E., Miao, M., Peng, F. and Kang, C. (2019). Probabilistic duck curve in high PV penetration power system: Concept, modeling, and empirical analysis in China. *Applied Energy*, vol. 242, pp. 205–215.

IEA (2018). World energy outlook. Document, International Energy Agency.
Available at: `https://iea.blob.core.windows.net/assets/77ecf96c-5f4b-4d0d-9d93-d81b938217cb/World_Energy_Outlook_2018.pdf`

IEC (2011). Electrical energy storage. White paper, International Electrotechnical Commission.
Available at: `https://www.iec.ch/basecamp/electrical-energy-storage`

IRENA (2012). Renewable energy technologies: cost analysis series, concentrating solar power. IRENA working paper 2, International Renewable Energy Agency.
Available at: `https://www.irena.org/-/media/Files/IRENA/Agency/Publication/2012/RE_Technologies_Cost_Analysis-CSP.pdf`

IRENA (2019). Utility-scale batteries - innovation landscape brief. Report, International Renewable Energy Agency.

Joskow, P. (2008). Capacity payments in imperfect electricity markets: Need and design. *Utilities Policy*, vol. 16, pp. 159–170.

Karni, J. (2015). Solar thermal power generation. *Annual Review of Heat Transfer*, pp. 37–92.

Kearns, J. (2017). *Effects of intermittent generation on the economics and operation of prospective baseload power plants.* Masters Thesis, Massachusetts Institute of Technology.

Kearton, W. (1944). *Steam turbine theory and practice.* 4th edn. Sir Isaac Pitman & Sons, London.

Kennedy, J. and Eberhart, R. (1995). Particle swarm optimization. In: *IEE International Conference on Neural Networks*, vol. 4, pp. 1942–1948. IEE.

Kesseli, D., Wagner, M., Guidéz, R. and Turchi, C. (2018). CSP-plant modeling guidelines and compliance of the System Advisor Model (SAM). SolarPACES (Preprint).

Killer, M., Farrokhseresht, M. and Paterakis, N. (2020). Implementation of large-scale Li-ion battery energy storage systems within the EMEA region. *Applied Energy*, vol. 260.

Kiviluoma, J. (2013). *Managing wind power variability and uncertainty through increased power system flexibility.* PhD, Aalto University.

Koohi-Fayegh, S. and Rosen, M. (2020). A review of energy storage types, applications and recent developments. *Journal of Energy Storage*, vol. 27.

Kraemer, S. (2017). Commercializing standalone thermal energy storage [Online]. Available: https://www.renewableenergyworld.com/2016/01/08/commercializing-standalone-thermal-energy-storage/gref [2020-05-14].

Kraemer, S. (2020). Morocco pioneers PV with thermal storage at 800 MW Midelt CSP project [Online]. Available: solarpaces.org/morocco-pioneers-pv-to-thermal-storage-at-800-mw-midelt-csp-project/ [2020-08-26].

Kröger, D. (1998). *Air-cooled heat exchangers and cooling towers: Thermal-flow performance evaluation and design.* Thesis (PhD), Stellenbosch University, Department of Mechanical Engineering.

Kumana, J. (2017). Thermodynamic analysis of steam turbines for industrial applications. In: *Industrial Energy Technology.*
Available at: `https://www.researchgate.net/publication/318402919`

Kuravi, S., Trahan, J., Goswami, D., Rahman, M. and Stefanakos, E. (2013). Thermal energy storage technologies and systems for concentrating solar power plants. *Progress in Energy and Combustion Science*, vol. 39, pp. 285–319.

Lara-Fanego, V., Ruiz-Arias, J., Pozo-Vázquez, D., Santos-Alamillos, F. and Tovar-Pescador, J. (2012). Evaluation of the WRF model solar irradiance forecasts in Andalusia (southern Spain). *Solar Energy*, vol. 86, pp. 2200–2217.

Larsson, P. and Börjesson, P. (2018). *Cost models for battery energy storage systems.* Bachelors Thesis, KTH School of Industrial Engineering and Management.

Lazar, J. (2016). Teaching the "duck" to fly. Document (second edition), Montpelier, VT: The Regulatory Assistance Project.
Available at: `https://www.raponline.org/wp-content/uploads/2016/05/rap-lazar-teachingtheduck2-2016-feb-2.pdf`

Leadbetter, J. and Swan, L. (2012). Battery storage system for residential electricity peak demand shaving. *Energy and Buildings*, vol. 55, pp. 685–692.

Leyzerovich, A. (2008). *Steam turbines for modern fossil-fuel power plants.* The Fairmont Press, Lilburn, GA. ISBN 0-88173-548-5.

Li, M., Du, W. and Nian, F. (2014). An adaptive particle swarm optimization algorithm based on directed weighted complex network. *Mathematical Problems in Engineering*, vol. 2014.

Limleamthong, P. and Guillén-Gosálbez, G. (2017). Rigorous analysis of Pareto fronts in sustainability studies based on bilevel optimization: Application to the redesign of the UK electricity mix. *Journal of Cleaner Production*, vol. 164, pp. 1602–1613.

Linder, J. and Lindkvist, S. (2011). *Interactive multiobjective optimization with application to hot rolling mills.* Masters Thesis, Chalmers University of Technology.

Liu, M., Tay, N., Bell, S., Belusko, M., Jacob, R., Will, G., Saman, W. and Bruno, F. (2016). Review on concentrating solar power plants and new developments in high temperature thermal energy storage technologies. *Renewable and Sustainable Energy Reviews*, vol. 53, pp. 1411–1432.

Lovegrove, K., James, G., Leitch, D., Milczarek, A., Ngo, A., Rutovitz, J., Watt, M. and Wyder, J. (2018). Comparison of dispatchable renewable electricity options: Technologies for an orderly transition. Tech. Rep., ARENA.
Available at: `https://arena.gov.au/assets/2018/10/Comparison-Of-Dispatchable-Renewable-Electricity-Options-ITP-et-al-for-ARENA-2018.pdf`

Lovegrove, K. and Stein, W. (2012). *Concentrating solar power technology: Principles, developments and applications.* 21st edn. Woodhead Publishing, Oxford, Cambridge, Philadelphia, New Delhi. ISBN 978-0-85709-617-3.

Lubkoll, M. and Claassen, M. (2019). Solar thermal energy systems. Presentation slides.

Lubkoll, M., Hockaday, S., Harms, T., von Backström, T., Amsbeck, L. and Buck, R. (2018). Integrating solar process heat into manganese ore pre-heating. In: *5th Southern African Solar Energy Conference.* SASEC, Durban, South Africa.

Luo, X., Wang, J., Dooner, M. and Clarke, J. (2015). Overview of current development in electrical energy storage technologies and the application potential in power system operation. *Applied Energy*, vol. 137, pp. 511–536.

Madaly, K. (2014). *Indentifying the optimum storage capacity for a 100 MWe concentrating solar power plant in South Africa.* Masters Thesis, Stellenbosch University, Department of Mechanical and Mechatronic Engineering.

Mahachi, T. (2016). *Energy yield analysis and evaluation of solar irradiance models for a utility scale solar PV plant in South Africa.* Masters Thesis, Stellenbosch University, Department of Electrical and Electronic Engineering.

Mahdi, Z., Merige, P., Caminos, R., Schmitz, P., Herrmann, U., Boura, C., Schmitz, M., Gielen, H., Gedle, Y. and Dersch, J. (2020). Modeling the thermal behavior of solar salt in electrical resistance heaters for the application in PV-CSP hybrid power plants. SolarPACES.

Mahlia, T., Saktisahdan, T., Jannifar, A., Hasan, M. and Matseelar, H. (2014). A review of available methods and development on energy storage; technology update. *Renewable and Sustainable Energy Reviews*, vol. 33, pp. 532–545.

Mahony, C. and Baartman, J. (2018). Tariff developments for electricity intensive industry in South Africa. *The Journal of the Southern African Institute of Mining and Metallurgy*, vol. 118, pp. 569–574.

Masdar (2022). Noor Midelt. [Online]. Available: https://masdar.ae/en/Masdar-Clean-Energy/Projects/Noor-Midelt [2022-02-08].

McKechnie, T. (2021). *Field layout and dispatch optimisation strategies for a concentrating solar thermal plant providing high-temperature process heat.* Masters Thesis, Stellenbosch University, Department of Mechanical and Mechatronic Engineering.

McKechnie, T., McGregor, C. and Venter, G. (2020). Concentrating solar thermal process heat for manganese ferroalloy production: Plant modelling and thermal energy storage dispatch optimization. In: *Proceedings of the ASME 2020 14th International Conference on Energy Sustainability*. ASME, Denver, CO, USA.

McLarnon, F. and Cairns, E. (1989). Energy storage. *Annual Review of Energy*, vol. 14, pp. 241–271.

Meteotest (2021). Meteonorm software [Online]. Available: https://meteonorm.com/en/ [2021-06-11].

Milligan, M., Ela, E., Hodge, B., Kirby, B., Lew, D., Clark, C., DeCesaro, J. and Lynn, K. (2011). Integration of variable generation, cost-causation, and integration costs. *The Electricity Journal*, vol. 24, pp. 51–63.

Montes, M., Abánades, A., Martínez-Val, J. and Valdés, M. (2009). Solar multiple optimization for a solar-only thermal power plant, using oil as heat transfer fluid in the parabolic trough collectors. *Journal of Solar Energy*, vol. 83, pp. 2165–2176.

Moriarty, P. and Honnery, D. (2016). Can renewable energy power the future? *Energy Policy*, vol. 93, pp. 3–7. ISSN 03014215.

Mostafa, M., Aleem, S., Ali, S., Ali, Z. and Abdelaziz, A. (2020). Techno-economic assessment of energy storage systems using annualized life cycle cost of storage (LCCOS) and levelized cost of energy (LCOE) metrics. *Journal of Energy Storage*, vol. 29.

National Grid (2016). System operability framework. Document. Available at: `https://www.nationalgrid.com/sites/default/files/documents/8589937803-SOF%202016%20-%20Full%20Interactive%20Document.pdf`

National Institute of Standards and Technology (2021). NIST chemistry webbook [Online]. Available: https://webbook.nist.gov/chemistry/.

NEA (2012). Nuclear energy and renewables: System effects in low-carbon electricity systems. Executive summary, Nuclear Energy Agency.

Nikolaidis, P. and Poullikkas, A. (2018). Cost metrics of electrical energy storage technologies in potential power system operations. *Sustainable Energy Technologies and Assessments*, vol. 25, pp. 43–59.

Notton, G. (2015). Importance of islands in renewable energy production and storage: the situation of the French islands. *Renewable and Sustainable Energy Reviews*, vol. 47, pp. 260–269.

Notton, G., Nivet, M., Voyant, C., Paoli, C., Darras, C., Motte, F. and Fouilloy, A. (2018). Intermittent and stochastic character of renewable energy sources: Consequences, cost of intermittence and benefit of forecasting. *Renewable and Sustainable Energy Reviews*, vol. 97, pp. 96–105.

NREL (2020*a*). Kathu Solar Park [Online]. Available: https://solarpaces.nrel.gov/kathu-solar-park [2020-07-02].

NREL (2020*b*). System Advisor Model version 2020.2.29 r3. Available: https://sam.nrel.gov/.

Obaid, Z., Cipcigan, L., Abrahim, L. and Muhssin, M. (2019). Frequency control of future power systems: Reviewing and evaluating challenges and new control methods. *Journal of Modern Power Systems and Clean Energy*, vol. 7, no. 1, pp. 9–25.

Pan, C. (2020). *A technical and economic assessment of molten salt parabolic trough power plants and operating strategies in Southern Africa*. PhD, Stellenbosch University.

Patel, S. (2019). Solar baseload in the Kalahari: Kathu Solar Park [Online]. Available: powermag.com/solar-baseload-in-the-kalahari-kathu-solar-park/ [2020-07-03].

Patnode, A. (2006). *Simulation and performance evaluation of parabolic trough solar power plants*. Masters Thesis, University of Wisconsin-Madison.

Pearre, N. and Swan, L. (2015). Technoeconomic feasibility of grid storage: Mapping electrical services and energy storage technologies. *Applied Energy*, vol. 137, pp. 501–510.

Pelay, U., Luo, L., Fan, Y., Stitou, D. and Rood, M. (2017). Thermal energy storage systems for concentrated solar power plants. *Renewable and Sustainable Energy Reviews*, vol. 79, pp. 82–100.

Pierce, W. (2013). *Solar assisted power generation (SAPG): Investigation of solar preheating of feedwater*. Masters Thesis, Stellenbosch University, Department of Mechanical and Mechatronic Engineering.

Poole, I. (2017). *Concentrating solar power in South Africa - a comparison between parabolic trough and power tower technologies with molten salt as heat transfer fluid*. Masters Thesis, Stellenbosch University, Department of Mechanical and Mechatronic Engineering.

Poole, I. and Dinter, F. (2017). A molten salt tower model used for site selection in South Africa using SAURAN meteorological data. In: *AIP Conference Proceedings*.

Praveen, R., Baseer, M., Awan, A. and Zubair, M. (2018). Performance analysis and optimization of a parabolic trough solar power plant in the Middle East region. *Energies*, vol. 11, no. 4, p. 741.

Rahman, M., Oni, A., Gemechu, E. and Kumar, A. (2020). Assessment of energy storage technologies: a review. *Energy Conversion and Management*, vol. 223.

Remund, J. and Müller, S. (2011). Solar radiation and uncertainty information of Meteonorm 7. In: *ISES Solar World Congress 2011*. ISES, Bern.

Riffelmann, K., Weinrebe, G. and Balz, M. (2020). Hybrid CSP-PV plants with integrated thermal storage. In: *SolarPACES*. SolarPACES.

Rossum, G.V. and Drake, F. (1995). *Python reference manual.* Centrum voor Wiskunde en Informatica Amsterdam.

SARS (2021). Duties and taxes for importers [Online]. Available: https://www.sars.gov.za/Pages/default.aspx [2021-01-04].

Schmidt, O., Melchior, S., Hawkes, A. and Staffell, I. (2019). Projecting the future levelized cost of electricity storage technologies. *Joule*, vol. 3, pp. 81–100.

Schöniger, F., Thonig, R., Resch, G. and Lilliestam, J. (2020). Making the sun shine at night: Comparing the cost of dispatchable concentrating solar power and photovoltaics with storage. *Energy Sources*, vol. 16.

Scolan, S., Serra, S., Sochard, S., Delmas, P. and Reneaume, J. (2020). Dynamic optimization of the operation of a solar thermal plant. *Solar Energy*, vol. 198, pp. 643–657.

Seel, J., Mills, A., Wiser, R., Deb, S., Asokkumar, A., Hassanzadeh, M. and Aarabali, A. (2018). Impacts of high variable renewable energy futures on wholesale electricity prices, and on electric-sector decision making. Technical report, Lawrence Berkeley National Laboratory.
Available at: `https://escholarship.org/content/qt2xq5d6c9/qt2xq5d6c9_noSplash_6c736ce8661e71aa1932bca7f4ef8339.pdf?t=p8rrvi`

Sener (2021). Parabolic trough plant Kathu [Online]. Available: https://www.energy.sener/project/parabolic-trough-plant-kathu [2021-06-08].

Short, W., Packey, D. and Holt, T. (1995). A manual for the economic evaluation of energy efficiency and renewable energy technologies.

Solar Energy Laboratory, University of Wisconsin Madison (2006). TRNSYS 16: Weather data.

Solargis (2021). Solar resource maps of South Africa [Online]. Available: https://solargis.com/maps-and-gis-data/download/south-africa [2021-09-11].

SolarPACES (2018). How CSP works: tower, trough, Fresnel or dish [Online]. Available: https://www.solarpaces.org/how-csp-works/ [2020-04-12].

Soliman, M., Talaat, H. and Attia, M. (2021). Power system frequency control enhancement by optimization of wind energy control system. *Ain Shams Engineering Journal*, vol. Article in press.

Solutia (2020). Therminol VP-1 [Online]. Available: http://twt.mpei.ac.ru/tthb/hedh/htf-vp1.pdf [2020-09-03].

Staffell, I. and Rustomji, M. (2016). Maximising the value of electricity storage. *Journal of Energy Storage*, vol. 8, pp. 212–225.

Starke, A., Cardemil, J., Escobar, R. and Colle, S. (2018). Multi-objective optimization of hybrid CSP-PV system using genetic algorithm. *Solar Energy*, vol. 147, pp. 490–503.

Steinmann, W., Jockenhöfer, H. and Bauer, D. (2019). Thermodynamic analysis of high-temperature Carnot battery concepts. *Energy Technology*. ISSN 21944296.

Stine, W. and Geyer, M. (2001). *Power from the Sun*.
Available at: `https://www.powerfromthesun.net/book.html`

Suberu, M., Mustafa, M. and Bashir, N. (2014). Energy storage systems for renewable energy power sector integration and mitigation of intermittency. *Renewable and Sustainable Energy Reviews*, vol. 35, pp. 499–514. ISSN 13640321.

Thaker, S., Olufemi, A. and Kumar, A. (2017). Techno-economic evaluation of solar-based thermal energy storage systems. *Energy Conversion and Management*, vol. 153, pp. 423–434.

Tielens, P. and Van Hertem, D. (2012). Grid inertia and frequency control in power systems with high penetration of renewables.

Trading Economics (2020). South African inflation rate [Online]. Available: https://tradingeconomics.com/south-africa/inflation-cpi [2020-07-03].

Trieb, F. and Thess, A. (2020). Storage plants - a solution to the residual load challenge of the power sector? *Journal of Energy Storage*, vol. 31.

Van Wyngaardt, M. (2016). Construction starts on 100 MW Kathu Solar Park [Online]. Available: https://www.engineeringnews.co.za/article/construction-starts-on-100-mw-kathu-solar-park-2016-10-07/rep_id:4136 [2020-09-02].

Wagner, M. (2008). *Simulation and predictive performance modeling of utility-scale central receiver system power plants.* Masters Thesis, University of Wisconsin-Madison.

Wagner, M. (2017*a*). *Optimization of stored energy dispatch for concentrating solar power systems.* PhD, Colorado School of Mines.

Wagner, M. (2017*b*). SAM webinars 2017: Modeling molten salt power tower systems in SAM 2017.1.17. Presentation slides.

Wagner, M. and Gilman, P. (2011). Technical manual for the SAM physical trough model. Technical report, NREL.
Available at: `https://www.nrel.gov/docs/fy11osti/51825.pdf`

Wagner, M., Newman, A., Hamilton, W. and Braun, R. (2017). Optimized dispatch in a first-principles concentrating solar power production model. *Applied Energy*, vol. 203, pp. 959–971.

Wang, Z. and Rangaiah, G. (2017). Application and analysis of methods for selecting an optimal solution from the Pareto-optimal front obtained by multiobjective optimization. *Industrial & Chemical Engineering Research*, vol. 56, pp. 560–574.

Wilke, D., Kok, S. and Groenwold, A. (2006). Comparison of linear and classical velocity update rules in particle swarm optimization: Notes on diversity. *International journal for numerical methods in Engineering*, vol. 70, pp. 962–984.

Wiser, R., Mills, A., Seel, J., Levin, T. and Botterud, A. (2017). Impacts of variable renewable energy on bulk power system assets, pricing, and costs. Technical report, Lawrence Berkeley National Laboratory & Argonne National Laboratory.
Available at: `https://emp.lbl.gov/publications/impacts-variable-renewable-energy`

Zakeri, B. and Syri, S. (2015). Electrical energy storage systems: a comparative life cycle cost analysis. *Renewable and Sustainable Energy Reviews*, vol. 42, p. 569â596.

Zaversky, F., Cabello, F., Bernardos, A. and Sánchez, M. (2020). A novel high-efficiency solar thermal power plant featuring electricity storage - ideal for the future power grid with high shares of renewables. SolarPACES.

Zhai, R., Liu, H., Chen, Y., Wu, H. and Yang, Y. (2017). The daily and annual technical-economic analysis of the thermal storage PV-CSP system in two dispatch strategies. *Energy Conversion and Management*, vol. 154, pp. 56–67.

Appendices

Appendix A

Benchmark Model

Kathu Solar Park is a 100 MW parabolic trough CSP plant with 4.5 hours of TES (Sener, 2021), located near the town of Kathu in the Northern Cape of South Africa. This section details the development of a representative model of Kathu in SAM, termed the benchmark model.

A.1 Meteorological Data Acquisition

A typical meteorological year weather file for Kathu Solar Park is obtained from Meteonorm version 7.1.11.24422 (Meteotest, 2021) with coordinates -27.611 ° latitude, 23.028 ° longitude and an elevation of 1187 m, sufficiently close to the plant (Google Earth, 2021). Meteonorm, as utilised in Pierce (2013); Mahachi (2016); Lubkoll *et al.* (2018); McKechnie *et al.* (2020); Pan (2020), is a widely used meteorological data repository in the solar community. Radiation data is from the period 1991-2010, and temperature data from 2000-2009. Atmospheric turbidity is interpolated.

The location's average air dry-bulb temperature is 20.43 °C, wet-bulb temperature 11.9 °C, wind speed 3.5 m/s, relative humidity 41.3 % and atmospheric pressure 88.6 kPa respectively. The annual DNI surmounts to 2736.4 $\mathrm{kWh/m^2}$, with a daily average of 7.5 $\mathrm{kWh/m^2}$. Interpolation is used to reconcile ground measurements with satellite-derived data, which introduces error.

A Meteonorm weather station is located in Upington at -28.43 ° latitude and 21.27 ° longitude (Solar Energy Laboratory, University of Wisconsin Madison, 2006). The Meteonorm data file is approximately 194 km from the weather station, therefore the data is certainly interpolated. According to Remund and Müller (2011), an annual uncertainty of $\approx 6.7\,\%$ to $7.3\,\%$ is expected for a deviation of this magnitude. The annual and daily total DNI from the Kathu Solar Park Meteonorm typical meteorological year data appears in line with the DNI maps published by Solargis (2021). Additional descriptive statistics of the meteorological data are provided in Appendix A.3.1-A.3.2.

A.2 Sourced SAM Inputs

The selected SAM technology is the physical parabolic trough with a single owner PPA financial model. The model is detailed by the various plant specifications sourced from literature (Table A.1). It is indicated how these specifications differ from the SAM default values. Sources for Table A.1 are provided in Table A.2.

Table A.1: Adjustments to SAM default design values.

Parameter	**Unit**	**SAM default**	**Actual**	**Key**
Loop outlet HTF temperature	°C	391	393	[1]
Hours of storage	h	6	4.5	[1]
SCE length	m	14.375	13	[2]
Number of loops	-	181	250	[2]
SCE aperture width	m	6	6.87	[2]
Absorber tube thickness	mm	2	3	[3]
Glass envelope outer diameter	mm	120	125	[3]
Absorber absorptance	-	0.963	0.96	[3]
Mirror reflectance	-	0.93	0.96	[3]
Envelope transmittance	-	0.964	0.97	[3]
Row spacing	m	15	21	[4]
Number of field subsections	-	2	4	[4]
SCA length	m	115	150	[5]
SCE's per SCA	-	8	12	[5]
Inflation rate	%	2.5	4.5	[6]
Minimum condenser pressure	inHg	1.25	2	[7]
PPA price escalation rate	%	1	4.5	[8]
Real discount rate	%	6.4	8.2	[9]

Table A.2: Sources for Table A.1.

Key	**Source**
[1]	NREL (2020*a*)
[2]	Patel (2019)
[3]	Donga and Kumar (2019)
[4]	Google Earth (2021)
[5]	De Klerk (2015)
[6]	Trading Economics (2020)
[7]	Wagner and Gilman (2011)
[8]	Pan (2020)
[9]	Fourie (2018); Department of Energy (2019)

Deduced from the SAM webinar videos released by NREL, the default values are reasonable and represent state of the art values for CSP plants. Therefore, in cases where a literature search does not indicate otherwise, the default values are used throughout.

A.3 Computed SAM Inputs

A.3.1 Design-point DNI

The design-point DNI is the DNI at which the plant should achieve its specified thermal rating (Wagner, 2017*b*). According to NREL (2020*b*), the design-point or reference DNI is best selected as the maximum value of the field collector DNI cosine product. This should be close to the maximum DNI expected for the location. An insufficiently low reference DNI yields excessive curtailed solar thermal energy. In comparison, an insufficiently high reference DNI creates an undersized solar field (NREL, 2020*b*).

The maximum collector DNI cosine product is 1086.04 W/m^2. Figure A.1 confirms that nearly 100 % of all DNI readings are contained below this reference DNI, which should yield an appropriate thermally sized solar field. A study by Poole and Dinter (2017) uses a similar design point DNI of 1000 W/m^2 for six CSP plants modelled in the higher DNI regions of South Africa. These are Springbok, Upington, Laingsburg, Kimberley, Vryburg and Molteno. The SAM default DNI of 950 W/m^2 is updated with 1086.04 W/m^2.

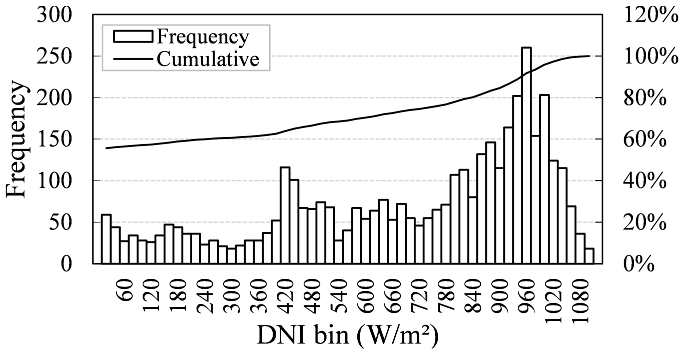

Figure A.1: Histogram of Meteonorm DNI.

A.3.2 Design-point Ambient Dry-bulb Temperature

A design-point dry-bulb temperature is specified as an input to the SAM benchmark model. Figure A.2 depicts a histogram of the ambient dry-bulb temperature data. At a cumulative percentage of ≈ 95 %, the design-point dry-bulb temperature is selected as 34 °C. Therefore, roughly 95 % of all temperatures occur below 34 °C. The SAM default of 42 °C is updated accordingly.

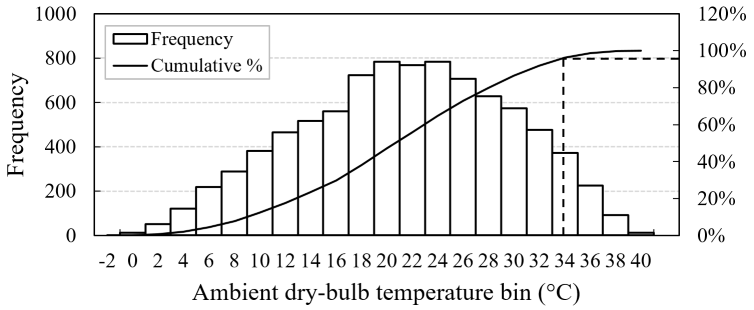

Figure A.2: Histogram of Meteonorm ambient dry-bulb temperature.

A.3.3 Power Cycle Design Thermal Efficiency

The power cycle design thermal efficiency is selected as 34 %, based on an estimation from the Chambadal-Novikov relation (Karni, 2015):

$$\eta_{\text{th}} = 1 - \sqrt{T_L/T_H} \tag{A.3.1}$$

where $T_H = 393 + 273.15 = 666.15$ K and $T_L = 34 + 273.15 = 307.15$ K are the design temperatures of the high and low thermal energy reservoirs between which the power cycle operates. The 34 % design thermal efficiency is well within the typical expected range of 32.3 % to 37.3 %. According to Lovegrove and Stein (2012), this range corresponds to a design high pressure steam inlet temperature of 373 °C (Table B.2). The default SAM efficiency of 37 % is updated as 34 %.

A.3.4 Field Aperture

The field aperture is used to define the solar field. According to NREL, it is the total solar energy collection area of the solar field (being less than the total mirror surface area). From the data in Table A.1, a solar collector element (SCE) has an aperture area of 13 m · 6.87 m = 89.31 m^2. The field aperture at design is then calculated as:

$$A_{\text{aperture,des}} = \frac{4\ \text{SCA's}}{\text{Loop}} \cdot \frac{250\ \text{Loops}}{\text{Field}} \cdot \frac{12\ \text{SCE's}}{\text{SCA}} \cdot \frac{89.31\ \text{m}^2}{\text{SCE}} = 1071720\ \text{m}^2/\text{field} \tag{A.3.2}$$

The default SAM value of 877000 m^2 is updated with the calculated value in Equation A.3.2. Lastly, the reflective aperture area is adjusted from 656 m^2 to 1075 m^2 to match the number of loops with the specified 250 loops (Table A.1).

Appendix B

Performance Model Formulation

This appendix provides additional information regarding the formulation of mathematical models for each of the parabolic trough CSP plant subsystems. Appendix B.1 considers the solar field, Appendix B.2 the power cycle, Appendix B.3 the TES system and Appendix B.4 the economic model.

B.1 Solar Field

B.1.1 Notes on the Pseudo Steady-state Approach

Deriving a detailed thermal and optical field model is outside the scope of this thesis. Instead, a simplified pseudo steady-state model, accounting for changes between steady-states, is formulated to deliver results with comparable accuracy. A macro CV is placed across the field which contains all solar collector assemblies, as depicted in Figure 4.3, with the indicated mass and energy flows across the CV boundary. Instead of performing extensive calculations to determine the net energy absorbed by the HTF running in the field, this is modelled externally in the SAM benchmark model. Its value, already accounting for aspects such as field optics, piping, layout, thermal losses and start-up requirements, is fed to the performance model's solar field CV as an hourly input.

The following section considers the transient energy and mass balance of the field macro CV and evaluates the requirements for negligible influence of transient effects. A mass balance of Figure 4.3's CV gives:

$$\sum_{\text{in}} \dot{m} - \sum_{\text{out}} \dot{m} = dm_{\text{CV}}/dt \tag{B.1.1}$$

Since $\dot{m}_{f,i} = \dot{m}_{f,o} = \dot{m}$, $dm_{\text{CV}}/dt = 0$. Hence, $m_{\text{CV}} \neq m_{\text{CV}}(t)$. This is not the case for the TES system (Appendix B.3.5). An energy balance conducted in

Poole (2017) can also be applied to Figure 4.3's CV. It yields the end-result:

$$T_{f,o}(t) = 2\left[\overline{T}^{0} - T_{f,i} - \dot{Q}_{f,\mathrm{HTF}}/(2\dot{m}\overline{c}_{p,\mathrm{HTF}})\right]\exp(-2t\dot{m}/m) + T_{f,i} + \dot{Q}_{f,\mathrm{HTF}}/(\dot{m}\overline{c}_{p,\mathrm{HTF}}) \tag{B.1.2}$$

with $\overline{T}^{0}$ the field CV's initial average HTF temperature and m the HTF mass contained in the CV. The transient response is locked up in the complimentary term, with the steady-state response in the particular term. Clearly:

$$\lim_{t\to\infty} T_{f,o}(t) = T_{f,i} + \dot{Q}_{f,\mathrm{HTF}}/(\dot{m}\overline{c}_{p,\mathrm{HTF}}) \tag{B.1.3}$$

which is the equation utilised in the pseudo steady-state model (Section 4.2.3.1). Therefore, the pseudo steady-state assumption becomes increasingly accurate for larger simulation time steps. The magnitude of the transient term is assessed between the design field inlet and outlet temperatures as initial condition and heat transfer and mass flow rates at various design levels. It is approximated that m is the HTF mass contained in all solar collector assemblies at the design field average temperature (the primary mass participating in solar thermal heat transfer within the CV).

Ranging heat transfer and mass flow rates from 80 % to 100 % of that at design, with $t = \Delta t = 3600$ s, the transient contribution is estimated between -0.27 °C to -0.008 °C. Disregarding data within 0 % to 1 % of design, majority of heat transfer rate and mass flow rate data points from the SAM benchmark occur within 90 % to 100 % of their designed maximums. The transient term can therefore be omitted without expecting significant sacrifice in accuracy.

Deduced from Patnode (2006), the omission of transient terms is a valid simplification throughout majority of the operating day, but can impede accuracy during warm-up cycles (such as HTF recirculation). This manifests itself as a higher-than-usual field outlet temperature in the performance model. As the performance of the Carnot battery is not quite dependent on HTF recirculation modes, this error is not expected to propagate.

B.1.2 Parasitics

The following field parasitics are identified and included in the model: HTF pumping power and collector tracking power. From the SAM benchmark model the HTF pumping power is calibrated against the HTF mass flow rate for a given SM. The result is shown in Figure B.1. A sufficient correlation is obtained in each case. This allows the performance model's solar field pumping power to be determined, for a certain SM, at any HTF mass flow rate within the allowable range $N_{\mathrm{loops}} \cdot [\dot{m}_{f,\mathrm{HTF,min}}, \dot{m}_{f,\mathrm{HTF,max}}]$.

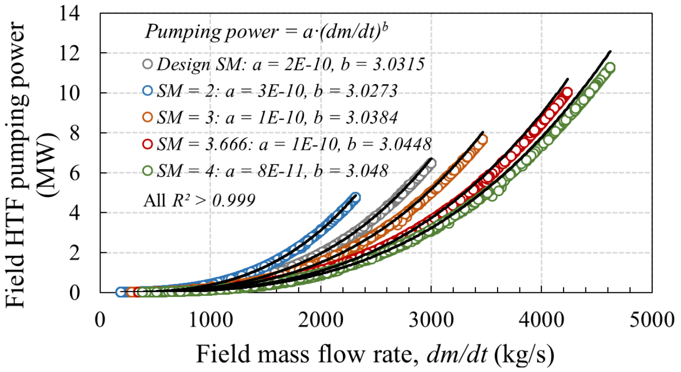

Figure B.1: Correlation for the field HTF pumping power.

Figure B.2 illustrates a relationship between DNI and collector tracking power. Simply put, full tracking power is consumed during daylight hours when DNI > 0. Therefore, tracking power is simulated in the SAM benchmark model and is included in the performance model as a hourly profile for the typical year. It is noted that a larger SM yields higher tracking power. Therefore, as with $\dot{Q}_{f,\mathrm{HTF}}(SM,t)$, so is $\dot{P}_{\mathrm{tracking}}(SM,t)$.

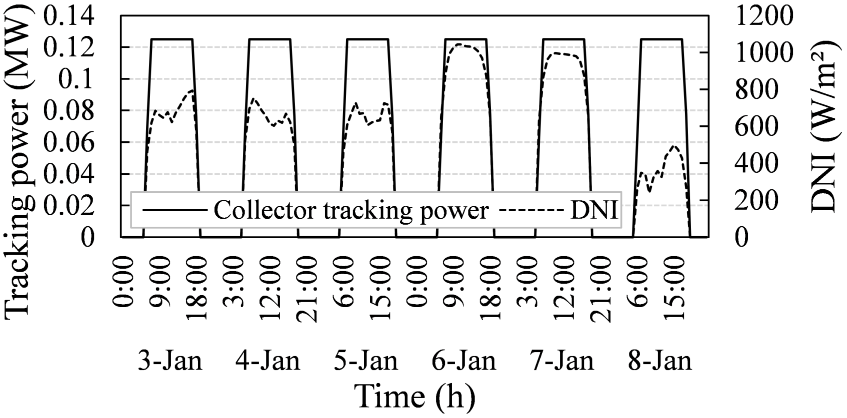

Figure B.2: Relationship between daylight hours and collector tracking power.

The cumulative field parasitics is:

$$\dot{P}_f = \dot{P}_{\mathrm{HTF,pumping}} + \dot{P}_{\mathrm{tracking}} \tag{B.1.4}$$

A summary of SAM benchmark parameters utilised in the performance model is given in Table B.1. For the plant in Section 6.12, time-varying input parameters to the performance model's solar field are re-computed in SAM.

Table B.1: Summary of SAM benchmark model inputs (solar field).

Parameter	Value	Unit
$\dot{Q}_{f,\text{HTF,net,abs}}$	$f(SM, t)$	MW
$\dot{Q}_{f,\text{HTF,loss}}$	$f(SM, t)$	MW
$T_{f,i,\text{des}}$	293	°C
$T_{f,o,\text{des}}$	393	°C
$\dot{m}_{f,\text{HTF,min}}$	1	kg/s/loop
$\dot{m}_{f,\text{HTF,max}}$	12	kg/s/loop
$N_{\text{loops,des}}$	250	loops
$\dot{P}_{\text{tracking,des}}$	125	W/SCA
$T_{\text{HTF,max}}$	393	°C

B.2 Power Cycle

B.2.1 Notes on Selecting a Basis Power Cycle

Performance modelling of CSP plants becomes complicated when accounting for the vast power cycle configurations for tailored applications. This necessitates the selection of a basis power cycle, representative of a general steam Rankine cycle design for parabolic trough CSP plants. Such a configuration is presented in Figure 4.4. Furthermore, the design specifications in Table B.2 match representative parabolic trough plant operating conditions for the given configuration (Wagner and Gilman, 2011). It is therefore also incorporated into the performance model. The cycle's T-s diagram is illustrated in Figure 4.5. Design parameters are summarised in Table B.3.

Table B.2: Design specifications for the basis Rankine power cycle (Wagner and Gilman, 2011).

Parameter	Value	Unit
HTF inlet temperature, $T_{\text{HTF,PC,des},i}$	393	°C
HTF outlet temperature, $T_{\text{HTF,PC,des},o}$	293	°C
HP turbine steam inlet temperature, T_{17}	373	°C
Boiler pressure, P_{HP}	10	MPa
Condenser pressure, P_{cond}	8.5	kPa
HP steam extraction fraction, y	0.13	-
IP steam extraction pressure, P_{IP}	2.39	MPa
LP steam extraction fraction, z	0.16	-
LP steam extraction pressure, P_{LP}	0.29	MPa
Turbine isentropic efficiency, $\eta_{s,t}$	0.7	-
Pump isentropic efficiency, $\eta_{s,p}$	0.695	-

B.2.2 Governing Assumptions

Certain assumptions pertain to the entire analysis (Patnode, 2006): it is assumed that all power cycle components, except for the cooling system, are adiabatic. Therefore, heat transfer to the surroundings is neglected. It is also analysed at pseudo steady-state (only hourly variations from one steady-state to another are considered). Kinetic and potential energy changes in working fluid streams are neglected. Changes in working fluid states between the outlet of one component and the inlet of another is neglected. No startup and shutdown cost penalties are incurred, but a startup energy penalty is enforced. Similar in SAM, startup and shutdown cost penalties are only implemented during dispatch optimisation and do not affect any of the output financial metrics (NREL, 2020*b*).

Minimum turbine operation and maximum turbine over-design levels are 0 and 1 respectively in both benchmark and performance models. All turbine startups follow a complete shutdown (Appendix B.2.12). Arguably, a minimum turbine operating level might be more applicable when solely considering load-following applications. The change in CF for a 0 % to 20 % change in the minimum turbine operating level (20 % being SAM's default value) for a flat TOD scheme is only 0.2 percentage points. As such, the turbine's minimum operating level is regarded negligible at the plant output level under uniform TOD.

In order to reduce the average moisture content of steam passing through the turbine stages, it is assumed the IP and LP extraction lines remove all moisture. As such, each successive turbine's inlet steam quality equals 1 (especially on the P_{LP} pressure line in Figure 4.5). Practically, this is achieved with the use of separators. Kearton (1944) presents a similar regenerative cycle to reduce turbine erosion owing to excessive steam moisture content.

Furthermore, the model assumes that pressure and temperature conditions on the P_{HP}, P_{IP} and P_{LP} pressure lines are fixed. Only conditions on the condenser pressure line vary with time. All steam property data are obtained from the National Institute of Standards and Technology (2021) and Çengel and Boles (2015).

B.2.3 Condenser Pump

The specific work required by the LP condenser pump is approximated as:

$$w_{p\text{LP}} \approx v_{11} \cdot (P_{\text{LP}} - P_{\text{cond}}) \cdot (1 - y) \cdot (1 - z)/\eta_{s,p} \tag{B.2.1}$$

where $v_{11} = v_{f@P_{\text{cond}}}$ is the working fluid saturated liquid specific volume at state 11 (assuming no subcooling) and $\eta_{s,p}$ is the pump isentropic efficiency. The condenser pressure is determined by an external model (Appendix B.2.10).

For a given condenser saturation pressure, v_{11} is given by the correlation in Figure B.3.

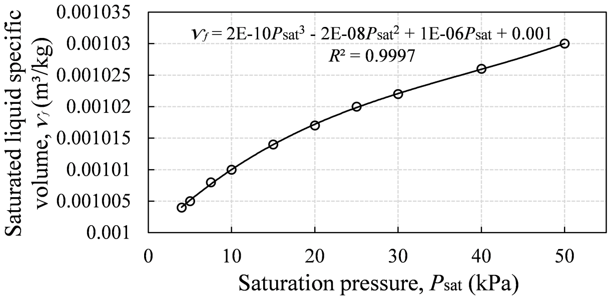

Figure B.3: $v_{11} = f(P_{\text{cond}})$.

B.2.4 Low Pressure Open Feedwater Heater

The LP OFWH mixes steam extracted from the turbine at P_{LP} directly with feedwater exiting the LP pump. By raising the average working fluid temperature prior to it entering the boiler, regeneration increases the temperature of heat addition in the boiler. This boosts the cycle's thermal efficiency (Çengel and Boles, 2015). An energy balance across the LP OFWH gives:

$$h_{13} = zh_{19a} + (1 - z) \cdot h_{12a} \tag{B.2.2}$$

where:

$$h_{12a} = h_{f@P_{\text{cond}}} + w_{p\text{LP}} \tag{B.2.3}$$

For the ideal cycle however, it can be assumed the working fluid mixture leaves the OFWH as a saturated liquid at the heater pressure (Çengel and Boles, 2015). Hence, $x_{13} = 0$ and:

$$h_{13} \approx h_{f@P_{\text{LP}}} \tag{B.2.4}$$

where x represents steam quality.

B.2.5 Intermediate Pressure Pump

The specific work required by the IP pump is approximated as:

$$w_{p\text{IP}} \approx v_{13} \cdot (P_{\text{IP}} - P_{\text{LP}}) \cdot (1 - y)/\eta_{s,p} \tag{B.2.5}$$

where $v_{13} = v_{f@P_{\text{LP}}}$ due to the designation $x_{13} = 0$.

B.2.6 High Pressure Open Feedwater Heater

An energy balance across the HP OFWH, together with the ideal cycle approximation, gives:

$$h_{15} = (1-y)\cdot h_{14a} + y h_{18a} \approx h_{f@P_{\mathrm{IP}}} \tag{B.2.6}$$

The inlet to the HP pump is therefore approximated at a quality $x_{15} = 0$.

B.2.7 High Pressure Pump

The specific work required by the HP pump is approximated as:

$$w_{p\mathrm{HP}} \approx v_{15}\cdot(P_{\mathrm{HP}} - P_{\mathrm{IP}})/\eta_{s,p} \tag{B.2.7}$$

where $v_{15} = v_{f@P_{\mathrm{IP}}}$. An energy balance across the HP pump gives:

$$h_{16a} = h_{15} + w_{p\mathrm{HP}} \tag{B.2.8}$$

which is the pre-heater inlet enthalpy.

B.2.8 Steam Generator

The energy flow diagram of Figure B.4 is incorporated into the power cycle model. The net thermal power available to the cycle is the gross thermal power supplied less mandatory deductions:

$$\dot{Q}_{\mathrm{PC,net,avail}} = \dot{Q}_{\mathrm{PC,in}} - \dot{Q}_{\mathrm{PC,su}} - \dot{Q}_{\mathrm{PC,bd}} \tag{B.2.9}$$

where $\dot{Q}_{\mathrm{PC,in}}$ is the total steam generator heat input rate, $\dot{Q}_{\mathrm{PC,su}} = f_{\mathrm{su}}\cdot\dot{Q}_{\mathrm{PC,in}} = E_{\mathrm{PC,su}}/\Delta t$ is the startup thermal power (Appendix B.2.12.2) and $\dot{Q}_{\mathrm{PC,bd}} = f_{\mathrm{bd}}\cdot(\dot{Q}_{\mathrm{PC,in}} - \dot{Q}_{\mathrm{PC,su}})$ is the thermal power lost through steam blowdown.

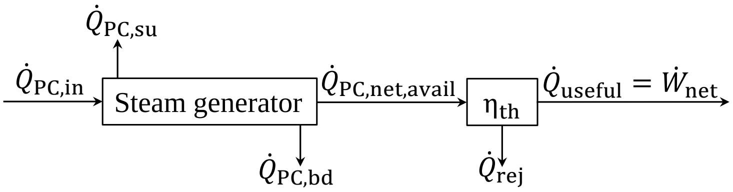

Figure B.4: Power cycle energy flows.

The power cycle's thermal efficiency divides the net available thermal power into useful and rejected quantities. The useful thermal power is converted into net mechanical power. The blowdown and startup deductions are therefore different from internal power cycle irreversibilities such as isentropic inefficiencies. These are regarded as inherent component "defects" or irreversibilities.

B.2.9 Turbine

B.2.9.1 Steam Moisture and Turbine Isentropic Efficiency

The turbine analysis neglects various internal steam turbine losses. Although the turbine inlet condition is superheated, this superheat decreases towards the outlet. As such, the last turbine stages are mostly operated with wet steam (Church, 1935). This is evident in the Rankine cycle of the performance model, where the IP and LP stages encounter saturated and wet steam respectively (Figure 4.5). An important consideration is the adverse effect of wetness (moisture) on the design turbine isentropic efficiency. Superheated stages operate with higher efficiencies than stages located in the wet region (Church, 1935). According to Church (1935), it is customary to assume a 1.15 % decrease in turbine stage efficiency per 1 % increase in the average stage moisture content:

$$\eta_{t,\text{red}} = [1 - 1.15(1-x)_m] \tag{B.2.10}$$

where $\eta_{t,\text{red}} \cdot \eta_{s,t}$ represents the reduced turbine design isentropic efficiency and $(1-x)_m$ is the mean moisture content between turbine inlet i and outlet o stages:

$$(1-x)_m = 0.5[(1-x)_i + (1-x)_o] \tag{B.2.11}$$

Since the design isentropic efficiency in Table B.2 is reported to match that of common parabolic trough Rankine power cycles, it should be evaluated whether $\eta_{s,t} = 0.7$ already accounts for a reduction due to moisture. In the absence of manufacturer data, Kumana (2017) presents the following correlation for turbine isentropic efficiency with fair accuracy:

$$\begin{aligned} \eta_{s,t} &= \dot{W}_{t,\text{gross,des}} / (B_1 + B_2 \dot{W}_{t,\text{gross,des}}) \qquad \text{(B.2.12)} \\ B_1 &= 3.53\Delta T_t - 463 \\ B_2 &= 1.22 + 0.000148\Delta T_t \end{aligned}$$

where ΔT_t is the difference between the turbine steam inlet and outlet temperatures. At design, Equation B.2.12 gives $\eta_{t,s} = 0.784$.

Figure B.5 depicts the LP turbine outlet steam quality at various condenser saturation pressures.

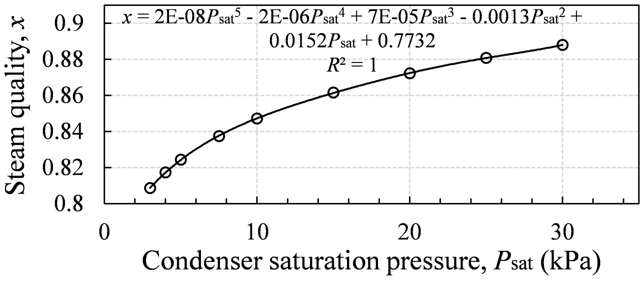

Figure B.5: Turbine outlet steam quality as a function of condenser pressure.

At the design condenser pressure, $x_o = 0.842$. Taking $x_i = 1$ (the HP turbine inlet condition is superheated), Equation B.2.11 gives $(1-x)_m = 0.5[(1-1)+(1-0.842)] = 0.079$ as the average moisture in the turbine. Equation B.2.10 then gives $\eta_{t,\mathrm{red}} = (1 - 1.15 \cdot 0.079) = 0.909$. Thus, the overall turbine isentropic efficiency, accounting for moisture, is $\eta_{t,\mathrm{red}} \cdot \eta_{s,t} = 0.909 \cdot 0.784 = 0.713$.

This independently calculated efficiency exhibits better accordance to the design value listed in Table B.2, as opposed to 0.784 which includes no moisture effects. On this basis, it is assumed that the design isentropic efficiency of 0.7 already incorporates steam moisture effects and will not be derated any further. As a simplification, all turbine stages assume this value.

B.2.9.2 Work

In Equation 4.2.11, $h_{17} - h_{18s}$ is the design isentropic enthalpy drop across the HP turbine. In Equation 4.2.12, $h_{18a} - h_{19s}$ is the design isentropic enthalpy drop across the IP turbine. The design isentropic enthalpy drop across the LP turbine is not fixed, but varies according to h_{20s} at the condenser pressure, being the outlet pressure of the LP turbine:

$$h_{20s} = h_{f@P_{\mathrm{cond}}} + x_{20s} \cdot h_{fg@P_{\mathrm{cond}}} \tag{B.2.13}$$

where the isentropic steam quality x_{20s} is determined as:

$$x_{20s} = (s_{20s} - s_{f@P_{\mathrm{cond}}})/s_{fg@P_{\mathrm{cond}}} \tag{B.2.14}$$

$$s_{20s} = s_{19} \tag{B.2.15}$$

Interpolations are implemented for the properties dependent on P_{cond}, the condenser saturation pressure, in Equations B.2.13 and B.2.14. The correlations are depicted in Figures B.6 and B.7.

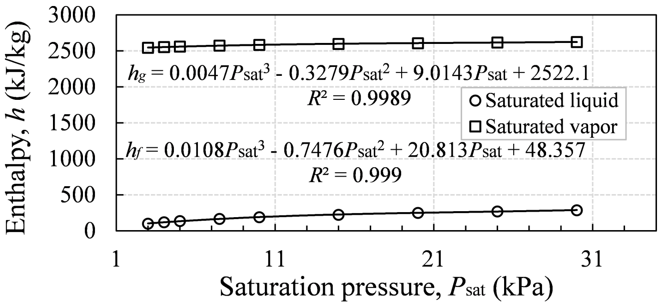

Figure B.6: Steam enthalpy correlations for Equation B.2.13.

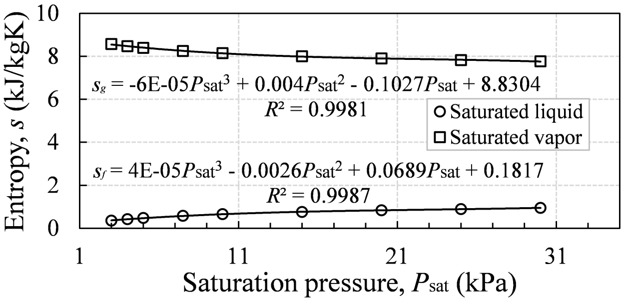

Figure B.7: Steam entropy correlations for Equation B.2.14.

B.2.10 Heat Rejection

The design cooling load is:

$$\dot{Q}_{\text{rej,des}} = \dot{Q}_{\text{PC,in,des}} \cdot (1 - \eta_{\text{th,des}}) \cdot (1 - f_{\text{bd}}) \tag{B.2.16}$$

which needs to be rejected by the cooling system at design. This corresponds to the design air mass flow rate:

$$\dot{m}_{a,\text{des}} = \dot{Q}_{\text{rej,des}} / [\bar{c}_{p,a} \cdot (T_{\text{ITD,des}} - \Delta T_{\text{out}})] \tag{B.2.17}$$

with $\bar{c}_{p,a}$ the average specific heat of dry air (Appendix D.3) in the ACC section. The initial temperature difference (steam to ambient) at design is $T_{\text{ITD,des}}$ and ΔT_{out} is the temperature difference at the condenser's hot side. These temperatures are illustrated in Figure B.8.

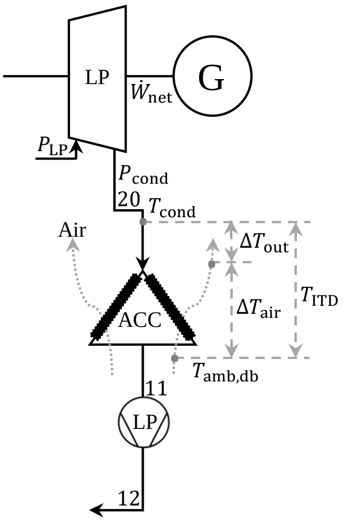

Figure B.8: Dry cooling temperature levels.

Similar to the approach outlined in Wagner and Gilman (2011), the actual cooling load and air mass flow rate are obtained from the off-design evaluations of Equation B.2.16:

$$\dot{Q}_{\text{rej}} = (1-\eta_{\text{th}})\cdot\dot{Q}_{\text{PC,net,avail}} \neq \dot{Q}_{\text{rej,des}} \tag{B.2.18}$$

and Equation B.2.17:

$$\dot{m}_a = \dot{Q}_{\text{rej}}/[\bar{c}_{p,a}\cdot(T_{\text{ITD}} - \Delta T_{\text{out}})] \tag{B.2.19}$$

However, $\dot{m}_a$ is limited to two part-load levels at either 50 % or 100 % of $\dot{m}_{a,\text{des}}$. Therefore:

$$\begin{cases} \dot{m}_a = 0.5\dot{m}_{a,\text{des}} & \text{if } 0 < \dot{m}_a \leqslant 0.5\dot{m}_{a,\text{des}} \\ \dot{m}_a = \dot{m}_{a,\text{des}} & \text{if } 0.5\dot{m}_{a,\text{des}} < \dot{m}_a \leqslant \dot{m}_{a,\text{des}} \end{cases} \tag{B.2.20}$$

The condenser temperature can be calculated as:

$$T_{\text{cond}} = T_{\text{amb,db}} + T_{\text{ITD}} \tag{B.2.21}$$

where $T_{\text{amb,db}}$ is the ambient dry-bulb temperature and T_{ITD} is calculated as:

$$T_{\text{ITD}} = \Delta T_{\text{out}} + \dot{Q}_{\text{rej}}/(\dot{m}_a\bar{c}_{p,a}) \tag{B.2.22}$$

The condenser pressure is simply $P_{\text{sat}@T_{\text{cond}}}$, for which a correlation is established in Figure B.9.

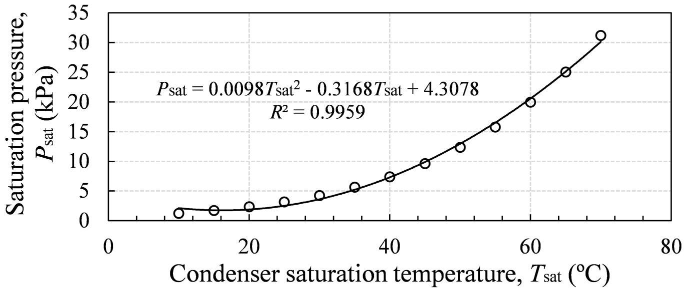

Figure B.9: Steam $P_{\text{cond}} = f(T_{\text{cond}})$.

Should $P_{\text{cond}} < P_{\text{cond,min}}$, then the condenser pressure is set to the minimum allowable pressure and the correlation in Figure B.9 is solved for a new estimate of $T_{\text{sat}} = T_{\text{cond}}$. Equation B.2.21 then solves an updated estimate of T_{ITD} and a new $\dot{m}_a$ is calculated, again limited to either 50 % or 100 % of $\dot{m}_{a,\text{des}}$.

Regardless of the $P_{\text{cond,min}}$ requirement, the power cycle's performance always depends on the condenser pressure. Thus the accompanying sub-models are interconnected via P_{cond}. Accordingly, they are executed consecutively and iterated until collective convergence is reached. The iteration sequence is described in short, with an initial estimate of $\dot{Q}_{\text{rej}}$ as starting point: $\cdots$ Equation B.2.18 → Equation B.2.19 → Equation B.2.20 → Equation B.2.22 → Equation B.2.21 → $P_{\text{cond}} = f(T_{\text{cond}})$ → P_{cond} check (if true, execute the outlined corrections) → Equation B.2.14 → Equation B.2.13 → Equation 4.2.13 → Equation 4.2.14 → Equation B.2.23 → Equation B.2.24 → Equation 4.2.15 → Equation 4.2.17 → Equation B.2.18 $\cdots$.

B.2.11 Off-design Power Generation

The effect of a varying steam generator heat input rate, $\dot{Q}_{\text{PC,in}}$, is captured in the power cycle's off-design performance. It is evident from Figure B.10 (generated from the SAM benchmark model for illustrative purposes only) that the nature of $\dot{Q}_{\text{PC,in}}$ linearly governs the power generation. As a simplification, $\dot{Q}_{\text{PC,in}}$ is allowed to linearly scale the performance of the basis Rankine cycle during off-design operation (without the use of any hard-coded correlation, such as the one established in Figure B.10).

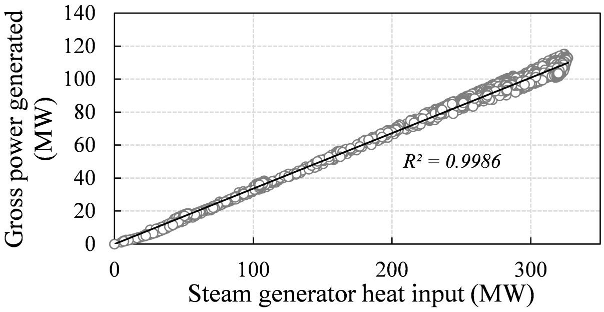

Figure B.10: Power cycle heat input rate vs. power generated.

Furthermore, the turbine only achieves its design isentropic efficiency when producing the rated power at the rated steam generator heat input and working fluid mass flow rates. In order to accommodate a deviation from the rated point, the isentropic efficiency is derated at throttled steam mass flow rates (Wagner, 2008) when $\dot{Q}_{\text{PC,in}} < \dot{Q}_{\text{PC,in,des}}$ from Equation 4.2.9. Authors such as Wagner and Gilman (2011); Barnes (2017); Poole and Dinter (2017) account for off-design effects by including thermal efficiency and scaling parameters based on $T_{\text{HTF,PC},i}$, $\dot{m}_{\text{HTF,PC}}$ or $T_{\text{amb,db}}$. Instead, it is assumed that off-design effects are well-captured by solely derating the performance of the turbine as considered here. In the absence of vendor data on turbine part-load isentropic efficiency, Kumana (2017) suggests the correlation in Figure B.11.

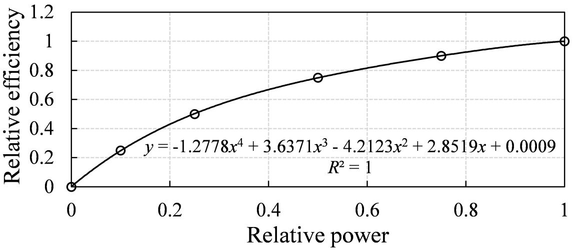

Figure B.11: Part-load turbine efficiency (Kumana, 2017).

The relative power (at a throttled steam mass flow rate) is calculated as:

$$Relative\ power = \dot{W}_t / \dot{W}_{t,\mathrm{gross,des}} \tag{B.2.23}$$

The gross turbine power is then derated to:

$$\dot{W}_{t,\mathrm{derated}} = Relative\ efficiency \cdot \dot{W}_t \tag{B.2.24}$$

and is used to recalculate the reduced net mechanical power (Equation 4.2.15), thermal efficiency (Equation 4.2.17) and net electrical output (Equation 4.2.16). Off-design performance considerations are neglected for all pumps, because $|pump\ work| \ll |turbine\ work|$.

B.2.12 Operating Modes

B.2.12.1 Shutdown

A shutdown of the power cycle occurs once the primary thermal energy sources (solar field and TES) become depleted. At this point, the power cycle shuts down as it ceases to receive thermal energy in the steam generator. This results in zero gross power output.

B.2.12.2 Startup

In CSP plants without auxiliary heating, a power cycle shutdown is followed by a startup once the solar thermal resource re-establishes itself. In a parabolic trough plant, this occurs as soon as the solar field produces sufficient thermal power. However, during startup the power cycle cannot produce power immediately at its rated capacity. The power cycle requires a certain startup thermal energy before it can produce power. This thermal energy is first required to heat up various components of the power cycle (such as the turbine and boiler). This raises the components from a cold state to a warmed state, in line with thermal constraints inherent to the component materials (Flynn, 2003).

A startup mode is initiated when the following criteria are met:

$$\dot{Q}_{\mathrm{PC,in}}^{t-\Delta t} = 0 \quad \& \quad \dot{Q}_{\mathrm{PC,in}}^{t} > 0 \quad \& \quad E_{\mathrm{tally}}^{t} = 0 \tag{B.2.25}$$

During this period the gross thermal power available, $\dot{Q}_{\mathrm{PC,in}}$, first contributes to meeting the design startup energy:

$$E_{\mathrm{PC,su,des}} = f_{\mathrm{su}} \cdot \dot{Q}_{\mathrm{PC,in,des}} \cdot \Delta t \tag{B.2.26}$$

The available startup energy is:

$$E_{\mathrm{PC,su}}^{t} = \min(\dot{Q}_{\mathrm{PC,in}}^{t} \cdot \Delta t, E_{\mathrm{PC,su,des}}) \tag{B.2.27}$$

and the startup energy tally becomes:

$$E_{\text{tally}}^{t+\Delta t} = E_{\text{tally}}^{t} + E_{\text{PC,su}}^{t} \tag{B.2.28}$$

The startup energy is implemented as a running tally. Therefore, the remaining required startup energy (if any) carries over to the next time step:

$$E_{\text{PC,su}}^{t+\Delta t} = \min(E_{\text{PC,su,des}} - E_{\text{tally}}^{t+\Delta t}, \dot{Q}_{\text{PC,in}}^{t+\Delta t} \cdot \Delta t) \tag{B.2.29}$$

Once $E_{\text{tally}}^{t+\Delta t} = E_{\text{PC,su,des}}$, the startup cycle is completed and the tally is set back to 0. Whenever $E_{\text{PC,su}}^{t} > 0$ during time t, the quantity $\dot{Q}_{\text{PC,su}}^{t} = E_{\text{PC,su}}^{t}/\Delta t$ is deducted from $\dot{Q}_{\text{PC,in}}^{t}$ and therefore lowers $\dot{Q}_{\text{PC,net,avail}}^{t}$.

B.2.13 Parasitics

The cumulative power cycle parasitics consist of:

$$\dot{P}_{\text{PC}} = \dot{P}_{\text{fan}} + \dot{P}_{\text{PC,HTF}} + \dot{P}_{\text{PC,backg}} \tag{B.2.30}$$

The individual parasitics are elaborated next.

B.2.13.1 Air-cooled Condenser Fan Power

The parasitic fan power is based on a model by Wagner and Gilman (2011). Treating dry air as an ideal gas, the isentropic fan outlet temperature is:

$$T_{\text{fan,out},s} = T_{\text{fan,in}} \cdot r_{p,\text{cond}}^{(R/c_{p,a})} \tag{B.2.31}$$

where $T_{\text{fan,in}} = T_{\text{amb,db}}$, $r_{p,\text{cond}}$ is the ACC air pressure ratio, R is the gas constant for air (0.287 kJ/kgK) and $c_{p,a}$ is the specific heat of dry air (Appendix D.3) evaluated at the fan inlet. Noting that $h_{\text{fan,in}} = h_{@T_{\text{fan,in}}}$ and $h_{\text{fan,out,s}} = h_{@T_{\text{fan,out},s}}$, the actual air outlet enthalpy is:

$$h_{\text{fan,out},a} = h_{\text{fan,in}} + (h_{\text{fan,out},s} - h_{\text{fan,in}})/\eta_{\text{fan},s} \tag{B.2.32}$$

with h the dry air's enthalpy (Appendix D.3) and $\eta_{\text{fan},s}$ the fan isentropic efficiency (a value of 0.96 is used). The fan power is then calculated as:

$$\dot{P}_{\text{fan}} = \dot{m}_a \cdot (h_{\text{fan,out},a} - h_{\text{fan,in}})/\eta_{\text{fan}} \tag{B.2.33}$$

with η_{fan} the fan mechanical efficiency, taken as 0.97.

B.2.13.2 Heat Transfer Fluid Pumping Power

This parasitic is simply expressed as:

$$\dot{P}_{\text{PC,HTF}} = \dot{m}_{\text{HTF,PC}} \cdot p_{\text{PC,HTF}} \tag{B.2.34}$$

where $\dot{m}_{\text{HTF,PC}}$ is the mass flow rate of HTF in the steam generator and $p_{\text{PC,HTF}}$ is a fixed pumping power per $\dot{m}_{\text{HTF,PC}}$.

B.2.13.3 Fixed Background Parasitic

Power plants typically encounter an additional fixed “background” parasitic, accounting for minor consumptions such as lighting, power supplied to offices and various operating equipment (Barnes, 2017). The performance model assumes a fixed background parasitic, $p_{\text{PC,fixed}}$, of 0.6105 MW/h. Therefore:

$$\dot{P}_{\text{PC,backg}} = p_{\text{PC,fixed}} \cdot \Delta t \tag{B.2.35}$$

B.2.14 Power Cycle Control Strategy

A high-level summary of the control strategy implemented for the power cycle's operation follows:

1. The power cycle is initialised with default design-point values;
2. Equation 4.2.14 is used to determine the working fluid mass flow rate $\dot{m}_w$ required to achieve the turbine's design gross mechanical power $\dot{W}_{t,\text{gross,des}}$;
3. Equation 4.2.9 is used to determine the required heat input rate $\dot{Q}_{\text{PC,in}}$ at the calculated $\dot{m}_w$;
4. If $\dot{Q}_{\text{PC,in}} > \min(\dot{Q}_{f,\text{HTF}}, \dot{Q}_{\text{PC,in,des}})$, then $\dot{Q}_{\text{PC,in}} = \min(\dot{Q}_{f,\text{HTF}}, \dot{Q}_{\text{PC,in,des}})$ and $\dot{m}_w$ is reduced to meet this constraint. The reduced $\dot{W}_t$ is calculated;
5. If $\dot{Q}_{\text{PC,in}} < \dot{Q}_{\text{PC,in,des}}$, then a quantity of thermal energy (if available) is drawn from storage to supply the deficit $\dot{Q}_{\text{PC,in,des}} - \dot{Q}_{\text{PC,in}}$;
6. If Criterion B.2.25 is met, then power cycle startup is accounted for;
7. The net available heat transfer rate in the power cycle $\dot{Q}_{\text{PC,net,avail}}$ is calculated by Equation B.2.9;
8. If $\dot{Q}_{\text{PC,in}} = 0$ instead (i.e. all the thermal sources have been exhausted), the power cycle ceases production altogether and enters shutdown mode until a thermal source is re-established;
9. With $\dot{Q}_{\text{PC,in}}$ finalised, the required HTF mass flow rate is calculated from Equation 4.2.9. If $\dot{m}_{\text{HTF,PC}} > \dot{m}_{\text{HTF,PC,des}}$, then $\dot{m}_{\text{HTF,PC}} = \dot{m}_{\text{HTF,PC,des}}$. For instances of $f \to$ PC only (when $\dot{m}_{\text{HTF},f\to\text{TES}} = 0 = \dot{m}_{\text{HTF,TES}\to\text{PC}}$) then $\dot{m}_{\text{HTF,PC}} = \dot{m}_{f,o}$. Should $\dot{m}_{\text{HTF,TES}\to\text{PC}} > 0$, then $\dot{m}_{\text{HTF,PC}} = \dot{m}_{f,o} + \dot{m}_{\text{HTF,TES}\to\text{PC}}$;
10. The power cycle HTF outlet temperature ($T_{\text{HTF,PC},o}$) is calculated and iterated at the given $\dot{m}_{\text{HTF,PC}}$ and $\dot{Q}_{\text{PC,in}}$;
11. Off-design corrections are performed if necessary, after which the cycle's net mechanical power and thermal efficiency is calculated;
12. The new heat rejection load is fed to the condenser model, which calculates an updated P_{cond}. The updated P_{cond} is fed to the power cycle model;

13. Via steps 2-12, the condenser and power cycle models are iterated consecutively until the turbine's mechanical power converges. Once converged, the cycle's final net mechanical power, gross electrical power, required HTF heat input and mass flow rates, as well as outlet temperature are known;
14. All power cycle parasitics are finalised;
15. The plant's total parasitics are deducted from the power cycle's gross electrical output to find the net electricity generated.

Table B.3: Summary of SAM benchmark model inputs (power cycle).

Parameter	**Value**	**Unit**
$\dot{W}_{t,\text{gross,des}}$	111	MW
$\eta_{\text{th,des}}$	0.34	-
$T_{\text{ITD,des}}$	16	°C
ΔT_{out}	3	°C
$P_{\text{cond,min}}$	6.773	kPa
$r_{p,\text{cond}}$	1.0028	-
$p_{\text{PC,HTF}}$	0.55	kJ/kg
$\dot{Q}_{\text{PC,in,des}}$	326	MWt
$\dot{m}_{\text{HTF,PC,des}}$	1328.2	kg/s
f_{su}	0.2	-
f_{bd}	0.02	-
$T_{\text{HTF,PC},i,\text{des}}$	393	°C
$T_{\text{HTF,PC},o,\text{des}}$	293	°C
$p_{\text{PC,fixed}}$	0.6105	MW/h

B.3 Thermal Energy Storage

B.3.1 Governing Assumptions

The following assumptions govern the analysis for the two-tank system in Figure 4.6: each tank is capable of storing all the HSF inventory. Both tanks are assumed to contain fully mixed HSF at an average lumped temperature. Therefore, stratification or thermal gradients during storage or charge-discharge cycles are not considered. Tank geometries are assumed similar. Both the hot and cold tanks are based on the same technical model. Heat loss only occurs to the ambient surroundings.

B.3.2 Volumetric Thermal Expansion

The hot tank is slightly oversized, because instances of $\overline{T}_h > 0.5(T_{h,\mathrm{des}} + T_{c,\mathrm{des}})$ occur, whereas $\overline{T}_c < 0.5(T_{h,\mathrm{des}} + T_{c,\mathrm{des}})$ holds true as hot HSF is always discharged to $T_{c,\mathrm{des}}$. This is especially relevant when hot HSF is supercharged via electric heaters to a higher average temperature. Regardless, hot HSF undergoes volumetric thermal expansion in excess of its design storage volume V_{TES}, whereas the cold HSF volume does not exceed V_{TES}. The hot tank needs to be slightly oversized (Pan, 2020) to accommodate the hot HSF expansion at higher $\overline{T}_h$'s.

An oversize multiplier for the hot tank is expressed as:

$$\delta_{\mathrm{TES},h} = 1 + dV_{\mathrm{TES},h}/V_{\mathrm{TES}} = 1 + (1/V_{\mathrm{TES}}) \cdot (dv_{\mathrm{HSF}}/d\overline{T}_h) \cdot \Delta\overline{T}_h \cdot m_{\max} \quad \text{(B.3.1)}$$

where V_{TES} is the original design volume of the tank and $m_{\max}$ is the designed maximum HSF inventory to be contained by a tank. Furthermore:

$$\Delta\overline{T}_h = \max[T_{h,\mathrm{des}}, \min(T_{\mathrm{set}}, 565\ ^\circ\mathrm{C})] - 0.5(T_{h,\mathrm{des}} + T_{c,\mathrm{des}}) \quad \text{(B.3.2)}$$

and from Appendix D.2 for molten salt as HSF:

$$\frac{dv_{\mathrm{HSF}}}{d\overline{T}_h} = \frac{d(1/\rho_{\mathrm{HSF}})}{d\overline{T}_h} = \frac{0.636}{(2090 - 0.636\overline{T}_h)^2} \quad \text{(B.3.3)}$$

with:

$$\overline{T}_h = \max[T_{h,\mathrm{des}}, \min(T_{\mathrm{set}}, 565)] \quad (^\circ\mathrm{C}) \quad \text{(B.3.4)}$$

The oversize is calculated to accommodate the extreme case in terms of $\overline{T}_h$ and $\Delta\overline{T}_h$. If there are no electric heaters, the maximum possible $\overline{T}_h$ is $T_{h,\mathrm{des}}$ and $\Delta\overline{T}_h = 45$ °C. The hot tank volume is adjusted to:

$$V'_{\mathrm{TES},h} = \delta_{\mathrm{TES},h} \cdot V_{\mathrm{TES}} \quad \text{(B.3.5)}$$

The hot (at $V'_{\mathrm{TES},h}$) and cold (at V_{TES}) tank diameters are calculated from:

$$D_{\mathrm{tank}} = 2\sqrt{V_{\mathrm{TES}}/(\pi H_{\max})} \quad \text{(B.3.6)}$$

It is noted that that the oversized hot tank does not create additional storage capacity, since the maximum HSF inventory (kg) remains constant at its design value based on V_{TES} (Appendix B.3.3). It also exerts no influence on the standard TES charge-discharge cycles. However, the oversized hot tank is assumed to elevate thermal losses, as its surface area increases (Appendix B.3.6). All TES design parameters are listed in Table B.4.

B.3.3 Initialisation

At time 0, the cold tank is assumed fully filled with HSF up to $H_{\max}$. The hot tank is assumed depleted, with HSF at $H_{\min}$. The mass of HSF in each tank is initialised at the arithmetic mean of the tank design temperatures:

$$m_c^{t=0} = \overline{\rho}_{\text{HSF}} \cdot V_{\text{TES}} = m_{\max} \tag{B.3.7}$$

$$m_h^{t=0} = \overline{\rho}_{\text{HSF}} \cdot V_{\text{TES}}(H_{\min}/H_{\max}) = m_{\min} \tag{B.3.8}$$

$$\overline{\rho}_{\text{HSF}} = \rho_{\text{HSF}} \left(\frac{T_{h,\text{des}} + T_{c,\text{des}}}{2} \right) \tag{B.3.9}$$

with ρ_{HSF} the molten salt density (Appendix D.2). The predetermined variables $m_{\max}$ and $m_{\min}$ are implemented as upper and lower design limits on the mass of HSF in each tank during subsequent cycles.

B.3.4 HTF/HSF TES Heat Exchanger Model

B.3.4.1 Solar Thermal Charge Cycles

The HSF charge mass flow rate required to meet $T_h = T_{h,\text{des}}$ is calculated as:

$$\dot{m}_{\text{HSF,chg}} = \dot{Q}_{f\to\text{TES}}/[\overline{c}_{p,\text{HSF}} \cdot (T_{h,\text{des}} - T_c)] \tag{B.3.10}$$

where $T_c = \overline{T}_c$, $\dot{Q}_{f\to\text{TES}}$ is the surplus field thermal energy sent to TES and $\overline{c}_{p,\text{HSF}}$ is the average HSF specific heat between the indicated temperatures. Similarly, the TES HX HTF outlet temperature is calculated as:

$$T_{\text{HTF,TES},o} = T_{\text{HTF,TES},i} - \dot{Q}_{f\to\text{TES}}/(\dot{m}_{\text{HTF},f\to\text{TES}} \cdot \overline{c}_{p,\text{HTF}}) \tag{B.3.11}$$

where $T_{\text{HTF,TES},i} = T_{f,o}$, the field HTF outlet temperature. All relevant temperatures are illustrated and labelled in Figure B.12.

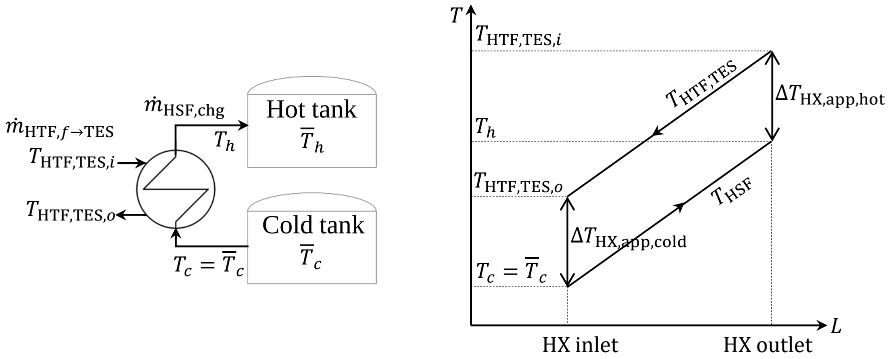

Figure B.12: TES HX charge cycle temperatures.

The second law of Thermodynamics requires a temperature difference on either sides of the HX between hot and cold streams (Figure B.12), of a nature:

$$T_{\text{HTF,TES}} - T_{\text{HSF}} > 0 \quad \forall L \in [\text{HX inlet}, \text{HX outlet}] \tag{B.3.12}$$

for heat transfer from HTF to HSF during charge cycles (and HSF to HTF during discharge cycles). The difference, modelled as an approach temperature, is the driving potential for heat transfer between the hot and cold streams. The hot and cold side HX approach temperatures are defined as:

$$\Delta T_{\text{HX,app,hot}} = T_{\text{HTF,TES},i} - T_h \tag{B.3.13}$$

$$\Delta T_{\text{HX,app,cold}} = T_{\text{HTF,TES},o} - T_c \tag{B.3.14}$$

Equations B.3.13 and B.3.14 introduce a caveat. Should $T_h > T_{\text{HTF,TES},i} - \Delta T_{\text{HX,app,hot}}$ during a charge cycle, it would contradict the requirements for heat transfer from the hot to the cold stream. This indicates that for the given $\dot{Q}_{f\rightarrow\text{TES}}$, $\dot{m}_{\text{HSF,chg}}$ should be increased according to:

$$\dot{m}_{\text{HSF,chg}} = \dot{Q}_{f\rightarrow\text{TES}}/\{\bar{c}_{p,\text{HSF}} \cdot [(T_{\text{HTF,TES},i} - \Delta T_{\text{HX,app,hot}}) - T_c)]\} \tag{B.3.15}$$

Similarly, should Equation B.3.11 yield $T_{\text{HTF,TES},o} < T_c + \Delta T_{\text{HX,app,cold}}$, then $\dot{m}_{\text{HTF},f\rightarrow\text{TES}}$ should be slightly increased at the given $\dot{Q}_{f\rightarrow\text{TES}}$ according to:

$$\dot{m}_{\text{HTF},f\rightarrow\text{TES}} = \dot{Q}_{f\rightarrow\text{TES}}/\{\bar{c}_{p,\text{HTF}} \cdot [T_{\text{HTF,TES},i} - (T_c + \Delta T_{\text{HX,app,cold}})]\} \tag{B.3.16}$$

As a final sanity check, the maximum HSF charge mass flow rate is always limited to:

$$\dot{m}_{\text{HSF,chg,max}} = (m_c - m_{\text{min}})/\Delta t \tag{B.3.17}$$

which ensures that the HSF inventory levels never drop below or rise above the minimum or maximum design quantities at the end of a time step Δt. A concomitant check for TES charging is also the requirement that $\dot{m}_{\text{HSF,chg,max}} > 0$. Should $\dot{m}_{\text{HSF,chg}} > \dot{m}_{\text{HSF,chg,max}}$, then $\dot{m}_{\text{HSF,chg}} = \dot{m}_{\text{HSF,chg,max}}$ and Equation B.3.18 iterates a new T_h:

$$T_h = T_c + \dot{Q}_{f\rightarrow\text{TES}}/(\dot{m}_{\text{HSF,chg}} \cdot \bar{c}_{p,\text{HSF}}) \tag{B.3.18}$$

with the subsequent approach temperature checks and steps repeated thereafter. With the TES HX model solved, the average HSF temperature in each tank is updated according to Equation 4.2.32.

Should a tank reach its inventory capacity, the TES charge cycle ceases. Since the power cycle already receives its design thermal input, all surplus solar thermal energy produced by the field beyond this point is discarded by defocusing the solar field. Therefore, $\dot{Q}_{f\rightarrow\text{TES}} = 0$. This allows the fraction of focused SCA's to be determined as:

$$f_{\text{focused SCA's}} = 1 - \dot{Q}_{f,\text{disc}}/\dot{Q}_{f,\text{HTF}} \tag{B.3.19}$$

where $\dot{Q}_{f,\text{disc}} = \dot{Q}_{f,\text{HTF}} - \dot{Q}_{\text{PC,in}}$.

The HTF temperature returning to the solar field inlet can be approximated as the weighted average of the fluid temperatures leaving from TES and the power cycle respectively:

$$T_{f,i} = (\dot{m}_{\mathrm{HTF},f\to\mathrm{TES}} \cdot T_{\mathrm{HTF,TES},o} + \dot{m}_{\mathrm{HTF,PC}} \cdot T_{\mathrm{HTF,PC},o})/(\dot{m}_{\mathrm{HTF},f\to\mathrm{TES}} + \dot{m}_{\mathrm{HTF,PC}}) \tag{B.3.20}$$

To avoid lengthy iterations during a time step, $T_{f,i} \approx T_{f,i,\mathrm{des}}$ is implemented instead. Finally, all HSF and HTF fluid properties are evaluated at their average temperatures with the thermophysical relations given in Appendix D. Where applicable, fluid properties are iterated until they converge.

B.3.4.2 Discharge Cycles

During discharge, the HTF outlet temperature is first determined as:

$$T_{\mathrm{HTF,TES},o} = \min[T_{\mathrm{HTF,TES},i} + \dot{Q}_{\mathrm{TES}\to\mathrm{PC}}/(\dot{m}_{\mathrm{HTF,TES}\to\mathrm{PC}} \cdot \bar{c}_{p,\mathrm{HTF}}), T_{\mathrm{HTF,max}}] \tag{B.3.21}$$

where $T_{\mathrm{HTF,TES},i} = T_{\mathrm{HTF,PC},o}$ and $T_{\mathrm{HTF,max}}$ is the practical maximum bulk HTF temperature, given by Heller (2013) as 393 °C. Figure B.13 illustrates a necessary requirement for heat transfer from HSF to HTF during discharge. This is the presence of an approach temperature difference on the hot and cold sides of the TES HX, such that:

$$T_{\mathrm{HSF}} - T_{\mathrm{HTF,TES}} > 0 \quad \forall L \in [\mathrm{HX\ inlet}, \mathrm{HX\ outlet}] \tag{B.3.22}$$

holds true. Thus, the same HX approach temperatures now define:

$$\Delta T_{\mathrm{HX,app,hot}} = T_h - T_{\mathrm{HTF,TES},o} \tag{B.3.23}$$

$$\Delta T_{\mathrm{HX,app,cold}} = T_c - T_{\mathrm{HTF,TES},i} \tag{B.3.24}$$

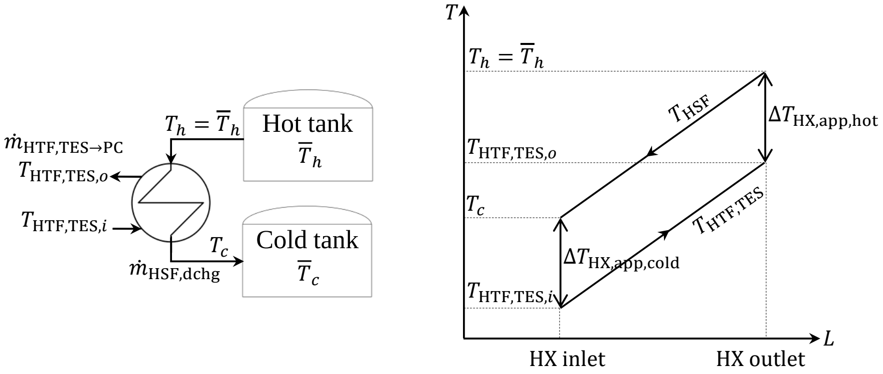

Figure B.13: TES HX discharge cycle temperatures.

Should Equation B.3.21 yield $T_{\mathrm{HTF,TES},o} > T_h - \Delta T_{\mathrm{HX,app,hot}}$, where $T_h = \bar{T}_h$, it would contradict the requirements for heat transfer from hot HSF to cold

HTF. Maintaining $\dot{m}_{\text{HTF,TES}\rightarrow\text{PC}}$ fixed at its preferred value (Equation 4.2.28), $\dot{Q}_{\text{TES}\rightarrow\text{PC}}$ is reduced to:

$$\dot{Q}_{\text{TES}\rightarrow\text{PC}} = \dot{m}_{\text{HTF,TES}\rightarrow\text{PC}} \cdot \bar{c}_{p,\text{HSF}} \cdot [(T_h - \Delta T_{\text{HX,app,hot}}) - T_{\text{HTF,TES},i}] \quad \text{(B.3.25)}$$

The power cycle HTF inlet temperature is estimated as:

$$T_{\text{HTF,PC},i} = (\dot{m}_{f,o} \cdot T_{f,o} + \dot{m}_{\text{HTF,TES}\rightarrow\text{PC}} \cdot T_{\text{HTF,TES},o})/\dot{m}_{\text{HTF,PC}} \quad \text{(B.3.26)}$$

where $\dot{m}_{\text{HTF,PC}} = \dot{m}_{f,o} + \dot{m}_{\text{HTF,TES}\rightarrow\text{PC}}$. The HSF discharge mass flow rate is calculated as:

$$\dot{m}_{\text{HSF,dchg}} = \dot{Q}_{\text{TES}\rightarrow\text{PC}}/[\bar{c}_{p,\text{HSF}} \cdot (T_h - T_{c,\text{des}})] \quad \text{(B.3.27)}$$

such that T_c discharges to $T_{c,\text{des}}$. Again, a sanity check requires that $\dot{m}_{\text{HSF,dchg}} \leqslant \dot{m}_{\text{HSF,dchg,max}}$, where:

$$\dot{m}_{\text{HSF,dchg,max}} = (m_h - m_{\min})/\Delta t \quad \text{(B.3.28)}$$

with m_h the current mass of HSF in the hot tank. This check ensures that the hot tank does not discharge below its minimum inventory level. Should $\dot{m}_{\text{HSF,dchg}} > \dot{m}_{\text{HSF,dchg,max}}$, then $\dot{m}_{\text{HSF,dchg}} = \dot{m}_{\text{HSF,dchg,max}}$ and T_c changes to accommodate this constraint:

$$T_c = T_h - \dot{Q}_{\text{TES}\rightarrow\text{PC}}/(\dot{m}_{\text{HSF,dchg}} \cdot \bar{c}_{p,\text{HSF}}) \quad \text{(B.3.29)}$$

with all relevant approach temperature checks and steps repeated thereafter. As noted, a concomitant check for TES discharging is also the requirement that $\dot{m}_{\text{HSF,dchg,max}} > 0$. If $\dot{m}_{\text{HSF,dchg,max}} = 0$, discharge ceases. With the TES HX model solved, the average HSF temperature in each tank is updated according to Equation 4.2.32. Lastly, all HSF and HTF fluid properties are evaluated at their average temperatures with the thermophysical relations given in Appendix D. Where applicable, fluid properties are iterated until they converge.

B.3.5 Unsteady-flow Mass and Energy Analysis

Figure B.14 shows a generic CV of a TES tank with an arbitrary amount of flow energies crossing the system boundary, together with possible heat transfer and shaft power.

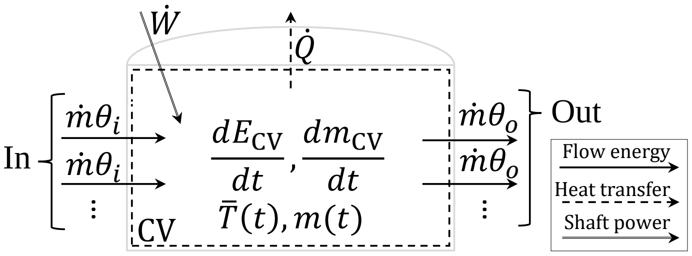

Figure B.14: General TES control volume.

A steady-flow process experiences no changes with time within a CV. However, the processes within the TES system involve definite time-dependent changes. This is characteristic of an unsteady-flow or transient process. The goal is to find a relation for $\overline{T}(t)$, the average HSF temperature inside the hot or cold tank as a function of time. A mass balance of the CV shows that:

$$\frac{dm_{\text{CV}}}{dt} = \frac{dm}{dt} = \sum_{\text{in}} \dot{m} - \sum_{\text{out}} \dot{m} \tag{B.3.30}$$

from which:

$$m = m(t + \Delta t) = \int_{t}^{t+\Delta t} \left(\sum_{\text{in}} \dot{m} - \sum_{\text{out}} \dot{m} \right) dt + m(t) \tag{B.3.31}$$

With time, there are definite inventory changes within the CV such that $dm_{\text{CV}}/dt \neq 0$. Next, consider an energy balance of the CV:

$$\sum_{\text{in}} \dot{E} - \sum_{\text{out}} \dot{E} = dE_{\text{CV}}/dt \tag{B.3.32}$$

$$\sum_{\text{in}} \left(\dot{Q} + \dot{W} + \dot{m}\theta \right) - \sum_{\text{out}} \left(\dot{Q} + \dot{W} + \dot{m}\theta \right) = dE_{\text{CV}}/dt \tag{B.3.33}$$

where $\theta = h + V^2/2 + gz$. Neglecting any kinetic and potential energy changes within the flow, $\Delta\theta \approx \Delta h$, where h is the HSF enthalpy. No shaft power is considered, therefore $\dot{W} \approx 0$. A heat transfer of $\dot{Q} = \dot{Q}_{\text{loss}}$ does occur out of the CV. No boundary work is present, since the system's CV boundaries are fixed. Furthermore, $dE_{\text{CV}}/dt = dU/dt$, where U is the system's internal energy. Therefore, changes in the CV's kinetic and potential energies are regarded negligible. Equation B.3.33 then becomes:

$$\sum_{\text{in}} (\dot{m}h) - \sum_{\text{out}} (\dot{m}h) - \dot{Q}_{\text{loss}} = dU/dt = \frac{d(mu)}{dt} = u\frac{dm}{dt} + m\frac{du}{dt} \tag{B.3.34}$$

where $u = u(t)$ and $m = m(t)$ are differentiable with time. For the purpose of the energy analysis, liquids (such as molten salt) can be approximated as incompressible substances with little sacrifice in accuracy. This infers that energy related with changes in volume is negligible when compared to other forms of energy involved (Çengel and Boles, 2015). For an incompressible substance with $dP \approx dv \approx 0$, it follows that $dh \approx du$ and $c_p \approx c_v = c$. Therefore:

$$du = c_v d\overline{T} = c d\overline{T} = c_p d\overline{T} = dh \implies \frac{du}{dt} = c\frac{d\overline{T}}{dt} = \frac{dh}{dt} \tag{B.3.35}$$

Substituting Equations B.3.35 and B.3.30 into Equation B.3.34 gives:

$$\sum_{\text{in}} (\dot{m}h) - \sum_{\text{out}} (\dot{m}h) - \dot{Q}_{\text{loss}} = u \cdot \left(\sum_{\text{in}} \dot{m} - \sum_{\text{out}} \dot{m} \right) + mc\frac{d\overline{T}}{dt} \tag{B.3.36}$$

Equation B.3.36 can be rearranged and integrated from t to $t + \Delta t$ to give:

$$\overline{T}(t + \Delta t) = \frac{\Delta t}{mc} \cdot \left[\sum_{\text{in}} (\dot{m}h) - \sum_{\text{out}} (\dot{m}h) - \dot{Q}_{\text{loss}} + u \cdot \left(\sum_{\text{out}} \dot{m} - \sum_{\text{in}} \dot{m} \right) \right] + \overline{T}(t) \tag{B.3.37}$$

where $\overline{T}(t)$ is the system's initial temperature at time t (the temperature at the end of the previous time step). By integration of the differential relations for u and h in Equation B.3.35, the internal energy and enthalpy per unit mass at a given state located by $\overline{T}$, is:

$$h(\overline{T}) = h_0 + \int_{T_0}^{\overline{T}} c(T)dT \tag{B.3.38}$$

$$u(\overline{T}) = u_0 + \int_{T_0}^{\overline{T}} c(T)dT \tag{B.3.39}$$

where $h_0 = h(T_0)$ and $u_0 = u(T_0)$ are the constant enthalpy and internal energy respectively at a reference state T_0. A reference state of $u(T_0 = 298.15\,\text{K}) = 0\,\text{kJ/kg} = h(T_0 = 298.15\,\text{K})$ is chosen. The choice of reference state is arbitrary, subject to it being implemented consistently (Çengel and Boles, 2015). Equations B.3.38 and B.3.39 are substituted into Equation B.3.37 and the expression is simplified to:

$$\begin{aligned}\overline{T}(t + \Delta t) = \frac{\Delta t}{mc} \cdot \Bigg\{ &\sum_{\text{in}} \dot{m} \cdot \left[h_0 + \int_{T_0}^{T_{\text{in}}} c(T)dT \right]_{\text{in}} - \sum_{\text{out}} \dot{m} \cdot \left[h_0 + \int_{T_0}^{\overline{T}(t+\Delta t)} c(T)dT \right]_{\text{out}} \\ &-\dot{Q}_{\text{loss}} + \left(\sum_{\text{out}} \dot{m} - \sum_{\text{in}} \dot{m} \right) \cdot \left[u_0 + \int_{T_0}^{\overline{T}(t+\Delta t)} c(T)dT \right] \Bigg\} + \overline{T}(t)\end{aligned} \tag{B.3.40}$$

It is evident that Equation B.3.40 should be iterated until $\overline{T}(t+\Delta t)$ converges. Equation B.3.40 is applied to both hot and cold TES tanks to determine their average HSF temperatures $\overline{T}$ at the end of a time step $t + \Delta t$.

B.3.6 Thermal Losses

Thermal losses are calculated per tank as a function of average HSF and ambient dry-bulb temperatures, as well as a heat loss coefficient:

$$\dot{Q}_{\text{loss},h} = UA_h \cdot (\overline{T}_h - T_{\text{amb,db}}) \tag{B.3.41}$$

$$\dot{Q}_{\text{loss},c} = UA_c \cdot (\overline{T}_c - T_{\text{amb,db}}) \tag{B.3.42}$$

$UA_{h/c}$ is a heat loss coefficient accounting for both surface area-specific heat transfer effects and the total surface area of a hot or cold tank (Wagner and

Gilman, 2011):

$$UA_h = \kappa \cdot \left(\frac{V'_{\text{TES},h}}{H_{\max} \cdot \tau} + \pi D_{\text{tank}} H_{\max} \right) \cdot \tau \tag{B.3.43}$$

$$UA_c = \kappa \cdot \left(\frac{V_{\text{TES}}}{H_{\max} \cdot \tau} + \pi D_{\text{tank}} H_{\max} \right) \cdot \tau \tag{B.3.44}$$

with τ denoting the number of parallel tank pairs (being one for this thesis) and κ a wetted loss coefficient. Total thermal losses from TES are:

$$\dot{Q}_{\text{loss}} = \dot{Q}_{\text{loss},h} + \dot{Q}_{\text{loss},c} \tag{B.3.45}$$

B.3.7 Parasitics

The TES HTF pumps consume power according to:

$$\dot{P}_{\text{TES,HTF}} = (\dot{m}_{\text{HTF},f\rightarrow\text{TES}} + \dot{m}_{\text{HTF,TES}\rightarrow\text{PC}}) \cdot p_{\text{TES,HTF}} \tag{B.3.46}$$

with $p_{\text{TES,HTF}}$ representing a TES HTF pumping power parameter.

A similar value for the HSF pumping power parameter is not evident in the SAM benchmark model. Therefore, its value is subject to an educated guess. Since the molten salt density and viscosity are higher than that of the thermal oil (Heller, 2013), it is assumed the HSF introduces greater pressure losses to be overcome by increased pumping power. Therefore, $p_{\text{TES,HSF}} > p_{\text{TES,HTF}}$ is one requirement. Through trial and error, a value of $p_{\text{TES,HSF}} = 0.173$ kJ/kg is selected. It produces a reasonable fit between the total HTF and HSF pumping parasitic in the SAM benchmark and performance models. Therefore:

$$\dot{P}_{\text{TES,HSF}} = (\dot{m}_{\text{HSF,chg}} + \dot{m}_{\text{HSF,dchg}}) \cdot p_{\text{TES,HSF}} \tag{B.3.47}$$

B.4 Economic Model

This appendix summarises the relevant economic parameters introduced in Sections 4.2.6 and 4.2.8.2.

B.4.1 Plant Costs

A breakdown of plant costs, given as default parameters in the SAM benchmark model, is presented here. These costs are representative of state-of-the-art CSP parabolic trough plants in the USA (NREL, 2020*b*) and suffices for the high-level analysis of this thesis.

Table B.4: Summary of SAM benchmark model inputs (TES).

Parameter	**Value**	**Unit**
$T_{\mathrm{MS,max}}$	593	°C
$T_{\mathrm{MS,min}}$	238	°C
$H_{\max}$	12	m
$H_{\min}$	1	m
$\Delta T_{\mathrm{HX,app,cold}}$	5	°C
$\Delta T_{\mathrm{HX,app,hot}}$	5	°C
$T_{h,\mathrm{des}}$	388	°C
$T_{c,\mathrm{des}}$	298	°C
$p_{\mathrm{TES,HTF}}$	0.15	kJ/kg
τ	1	-
κ	0.4	$\mathrm{W/m^2K}$

B.4.1.1 Direct Capital Costs

Direct capital costs are expenses related to a piece of equipment or service, incurred during year zero of the project's cash flow (NREL, 2020*b*). The plant's direct capital cost breakdown is given in Table B.5. The cost breakdown for a single representative electric process heater for high temperature applications is given in Table B.6.

Table B.5: Breakdown of direct capital costs.

Cost parameter, *C*	**Value**	**Unit**
Site improvements	25	$\$/\mathrm{m}^2$
Solar field	150	$\$/\mathrm{m}^2$
HTF system	60	$\$/\mathrm{m}^2$
TES	62	$/kWht
Power plant	910	$/kWe
Balance of plant [27]	90	$/kWe
Contingency [28]	7	% of subtotal

The intensive cost-delta between a carbon steel and stainless steel hot tank (ΔC_{TES} in Section 4.2.8.2) is calculated. The 62 $/kWht in Table B.5 is for a conventional parabolic trough plant with indirect TES and both tanks of carbon steel ($T_{\mathrm{set}} < 400$ °C). However, with $T_{\mathrm{set}} \geqslant 400$ °C, the hot tank material necessitates stainless steel. ΔC_{TES} is added to C_{TES} to account for the difference in material cost, per unit of design indirect TES capacity.

---

[27] Accounts for typical additional power block costs (NREL, 2020*b*).

[28] Accounts for anticipated uncertainties in direct capital cost (NREL, 2020*b*).

Data from Glatzmaier (2011) suggests a 3.9 \$/kWht material cost difference between a carbon steel and stainless steel tank in a direct TES system. This is scaled upwards to reconcile direct with indirect TES charge capacities:

$$\frac{\Delta C_{\text{TES,indirect}}}{E_{\text{TES,indirect}}} = \frac{\Delta C_{\text{TES,direct}}}{E_{\text{TES,direct}}} \cdot \frac{E_{\text{TES,direct}}}{E_{\text{TES,indirect}}} \tag{B.4.1}$$

For the same HSF inventory, the rightmost scaling ratio is estimated as:

$$\frac{E_{\text{TES,direct}}}{E_{\text{TES,indirect}}} = \int_{T_{c,\text{des}}=290\ ^{\circ}\text{C}}^{T_{h,\text{des}}=565\ ^{\circ}\text{C}} c_{p,\text{HSF}}(T)dT\bigg|_{\text{direct}} \bigg/ \int_{T_{c,\text{des}}=298\ ^{\circ}\text{C}}^{T_{h,\text{des}}=388\ ^{\circ}\text{C}} c_{p,\text{HSF}}(T)dT\bigg|_{\text{indirect}} \tag{B.4.2}$$

equating to ≈ 3.1. Therefore, $\Delta C_{\text{TES,indirect}} = 3.9 \cdot 3.1 = 12.09$ \$/kWht. A crude sanity check is performed on the obtained scaling ratio (3.1). For a given HSF inventory, what is the intensive TES cost for a direct system if it is 62 \$/kWht for an indirect system? This corresponds to:

$$(62/E_{\text{TES,indirect}}) \cdot (E_{\text{TES,indirect}}/E_{\text{TES,direct}} = 1/3.1) + 3.9 = 62/3.1 + 3.9 = 23.9\ \$/\text{kWht} \tag{B.4.3}$$

where 3.9 \$/kWht accounts for the additional cost difference between carbon steel and stainless steel. With no prior knowledge of SAM's direct TES cost, the scaling ratio yields an answer reasonably close to it: 22 \$/kWht (NREL, 2020*b*). Thus the calculated scaling ratio and ΔC_{TES} are deemed reasonable.

Table B.6: Electric heater cost breakdown (obtained from EXHEAT, 2020).

Cost	**Price (\$)** [29]
Electric molten salt heater	348901.46
Thyristor control panel	129982.90
Power transformer	225759.77
Packing	6841.20
Documentation	6157.08
Sun shade	684.12
Heater hydrodynamic test	957.77
Control panel test	957.77
Subtotal	720242.07
VAT [30] (20 %)	144048.41
Customs value	864290.48
VAT on imported goods [31]	142607.93
Total	**1006898.41**

---

[29] GBP to USD exchange rate as of 4 January 2021.

[30] Standard rate of VAT (value added tax) in the United Kingdom (product origin), as of 4 January 2021 (GOV.UK, 2021).

[31] *VAT on goods imported into SA* $\approx$ (1.1 $\cdot$ *Customs value*) $\cdot$ 0.15. Standard South African (SA) VAT rate of 15 %, as of 4 January 2021 (SARS, 2021).

B.4.1.2 Indirect Capital Costs

Indirect capital costs, broken down in Table B.7, are not directly linked to a specific piece of equipment or service (NREL, 2020*b*).

Table B.7: Breakdown of indirect capital costs.

Parameter	Value	Unit
EPC & owner costs [32]	11	% of TDCC
Total land cost	10000	\$/acre
Sales tax rate	5	%
Sales tax basis [33]	80	%

Equation 4.2.44's total land cost is based on the total land area at the SM. Furthermore in Equation 4.2.44:

$$Sales\ tax = Sales\ tax\ rate \cdot Sales\ tax\ basis \cdot TDCC \tag{B.4.4}$$

B.4.1.3 Operational and Maintenance Costs

O&M costs are equipment and service expenses incurred once the plant becomes operational (NREL, 2020*b*). O&M costs can be split into fixed (FOC) and variable (VOC) costs. The data in Table B.8 is used.

Table B.8: Breakdown of O&M costs.

Parameter	Value	Unit
Fixed costs, C_{FOC}	66	\$/kWh-yr (by capacity)
Variable costs, C_{VOC}	4	\$/MWh (by generation)

B.4.2 Fixed Charge Rate LCOE Model

Fixed charge rate LCOE model parameters (Section 4.2.6.1) are: $CRF^{34} = 0.056$, $PFF^{35} = 1.066$ and $CFF^{36} = 1.024$.

---

[32] Engineer-procure-construct and owner costs are linked to project design and construction (NREL, 2020*b*).

[33] A percentage of the TDCC used to determine the sales tax cost (NREL, 2020*b*).

[34] Fraction of TIC, used to entirely repay a loan (+ interest) over the loan term (Short *et al.*, 1995; NREL, 2020*b*).

[35] Factors in project financing costs (NREL, 2020*b*).

[36] Factors in construction financing costs (NREL, 2020*b*).

Appendix C

Performance Model Validation

Additional performance model validation results are shown. The model is validated at design (Section 4.2.7) before applying it as a Carnot battery (Section 4.2.8). In Appendix C.1, C.2 and C.3, only the parabolic trough (PT) plant is validated. In Appendix C.4, the Carnot battery plant is validated.

C.1 PT Plant: Energy and Mass Conservation

The extent of energy and mass conservation within the performance model provides an indication of its validity. The validation results are carried out for a high and low-level energy and mass balance of the parabolic trough plant at design. A high-level balance considers the flow of mass and energy between CV's encapsulating the field, TES and power block respectively. A low-level balance considers each CV in more detail. That is, the conservation laws should not only hold between CV's, but also within each CV. In order to make the validation results more intuitive, the high-level balances are split into charge and discharge mode balances respectively (illustrated in Figures C.1 and C.2).

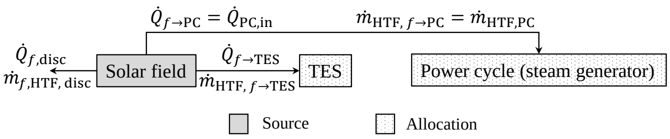

Figure C.1: Charge mode: high-level energy and mass balance.

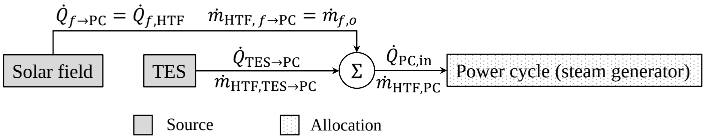

Figure C.2: Discharge mode: high-level energy and mass balance.

A charge mode balance is initiated whenever $\dot{Q}_{\text{PC,in}} > \dot{Q}_{\text{PC,in,des}}$, and a discharge mode balance whenever $\dot{Q}_{\text{PC,in}} \leqslant \dot{Q}_{\text{PC,in,des}}$. This isolates a source of energy and tracks the allocation thereof. The energy balance demands that the sum of the allocated energies do not exceed the sum of the sources' collected energies, on an annual basis. The results are depicted in Figures C.3a-C.3b.

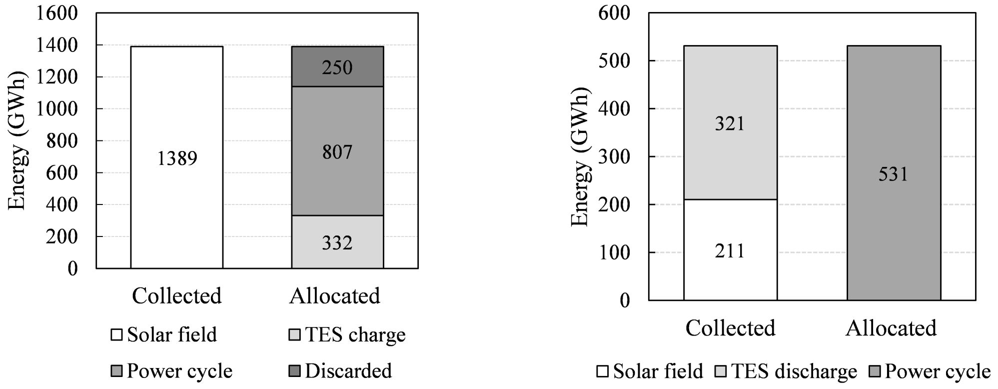

(a) Charge mode.

(b) Discharge mode.

Figure C.3: High-level energy balance validation.

In either mode, it can be seen that the cumulative energy allocated does not exceed the cumulative source of energy collected (evident from equal left and right-hand column heights).

An additional analysis calculates the high-level energy and mass balance relative errors per hour of the simulated year. Relative errors are measured between the "source" and "allocation" of mass and energy at that hour, according to Equation C.2.1. The energy and mass balance results are depicted in Figure C.4. All errors are virtually zero.

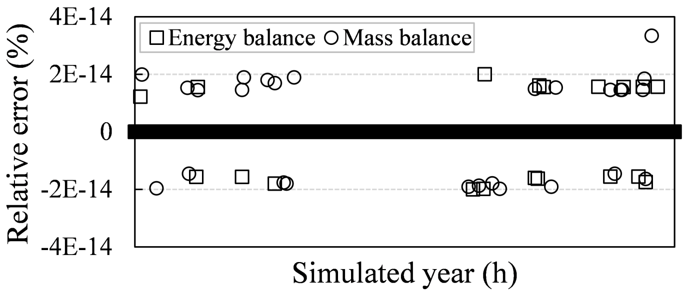

Figure C.4: High-level energy and mass balance: hourly relative errors.

A low-level TES energy balance is given in Figure C.5a. In addition to thermal losses, the minimum inventory requirement and approach temperature limitations also restrict the discharged thermal energy (a similar observation is made in SAM). A cumulative TES energy balance error of 0.9 % is present, which is comparable to the value found in SAM: 0.5 %. Accuracy is observed in the TES mass balance (Figure C.5b), where the total HSF inventory remains constant within decimal-point accuracy.

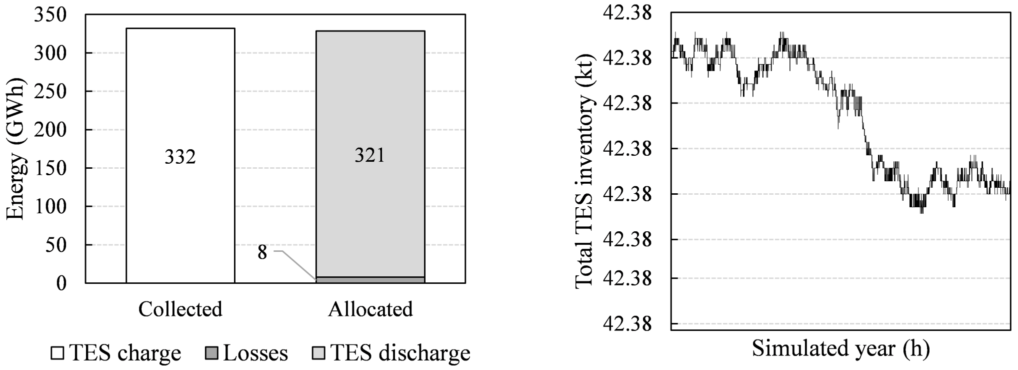

(a) Energy balance.

(b) Mass balance.

Figure C.5: TES energy and mass balance.

A low-level energy balance of the power cycle heats is given in Figure C.6. Figure C.6a depicts the energies consistent with Figure B.4. The left-hand column indicates the gross heat supplied to the steam generator. The right-hand column (energy allocation) shows the startup and blowdown heat deductions, as well as the remaining net available heat and waste heat. The net available heat is, by definition, equal to the net mechanical work produced by the cycle. This equivalence can be observed in Figure C.6b. The net electric energy is equal to the net mechanical work less the total plant parasitic energy consumption.

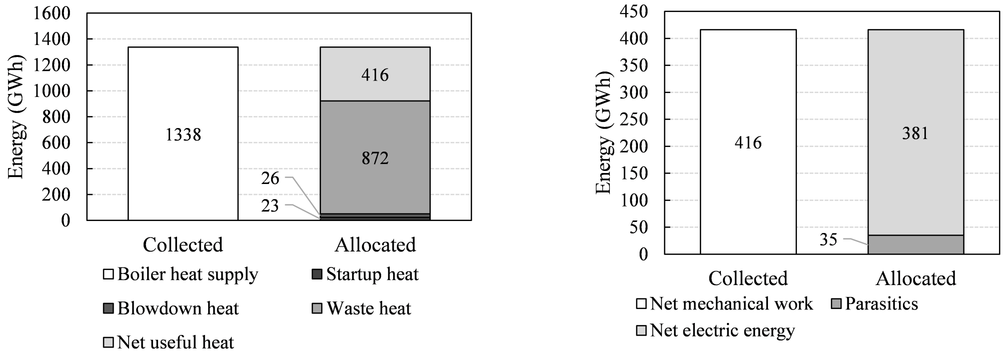

(a) Heat balance.

(b) Gross-to-net energy balance.

Figure C.6: Power cycle heat balance.

The balance of the plant's parasitics is detailed in Figure C.7. On the whole, a reasonable agreement is observed in the power cycle's energy balances.

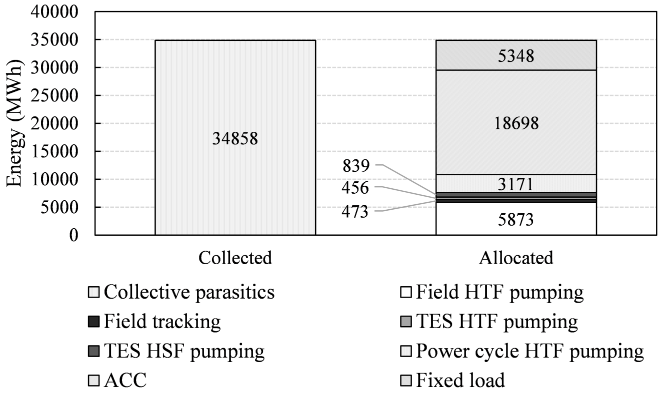

Figure C.7: Energy balance of plant parasitics.

C.2 PT Plant: Performance Model against SAM Benchmark Model

The performance model is also compared to the SAM benchmark model in evaluating its validity. An annual simulation of both models is performed at design. Some desired output parameters are not directly given as simulation results in SAM, thereby requiring post-processing of the SAM output data.

Figure C.8 compares the annual energies of the performance model to the SAM benchmark model.

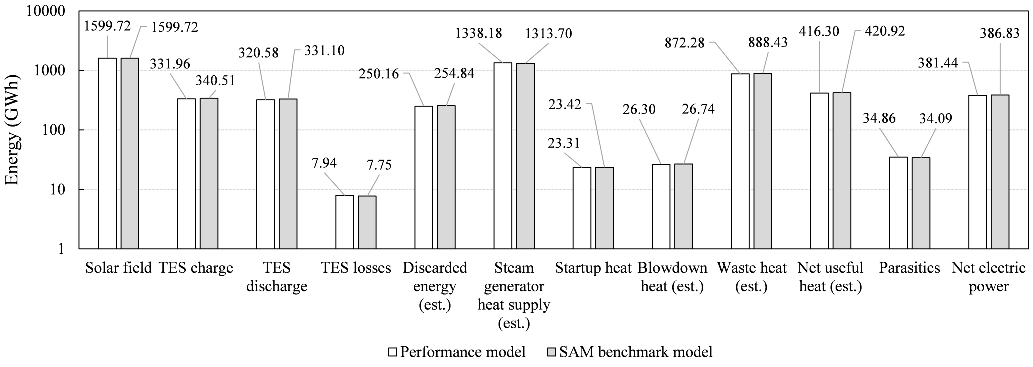

Figure C.8: Performance model vs. SAM benchmark model: energies.[37]

In Figure C.9, the results of Figure C.8 are converted to relative errors according to:

$$Relative\ error = \frac{Performance\ model - SAM\ benchmark\ model}{SAM\ benchmark\ model} \cdot 100\ \% \tag{C.2.1}$$

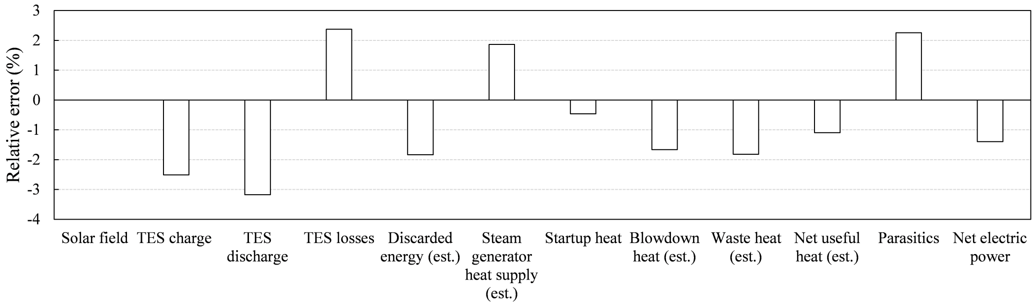

Figure C.9: Relative errors in Figure C.8.

The largest absolute error occurs in the total thermal losses from TES. There is no error in the annual solar field energy. This is because the performance model relies on the field thermal power (an output of the SAM benchmark model) as an input.

Figure C.10a compares the annual energy consumed by plant parasitics, as predicted by the performance model, to that of the SAM benchmark at design. When comparing the two results, a suitable agreement can be observed. Figure C.10b converts the results of Figure C.10a into relative error bars (via Equation C.2.1), where the highest absolute relative error occurs in the ACC energy consumption.

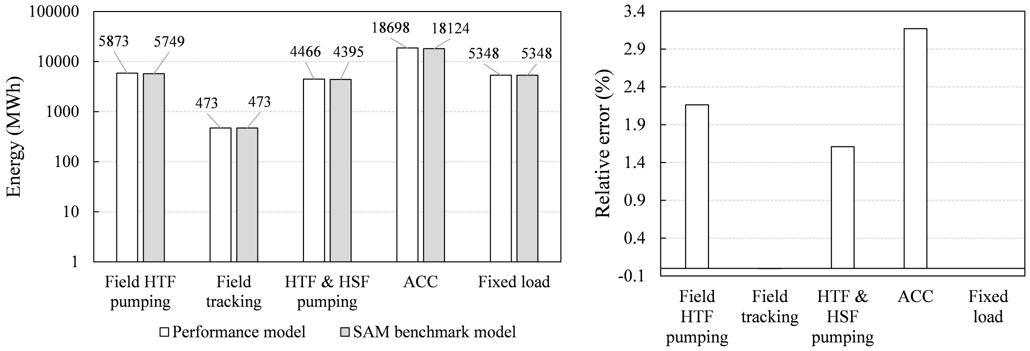

(a) Energies.

(b) Relative errors.

Figure C.10: Performance model vs. SAM benchmark model: plant parasitics.

---

[37] Parameters given with "(est.)" are not directly reported as outputs in SAM. These quantities are post-calculated from the given SAM outputs and only serve as estimates of magnitude in comparison to the performance model.

It is deduced from Figures C.9 and C.10b that all errors occur between −3.176 % to 3.168 %. Based on this observation, it can be argued that the parabolic trough performance model is within reasonable agreement to the SAM benchmark model. Errors are expected, as the performance model's formulation differs from SAM. Therefore, these deviations are not truly "errors", but rather highlight the fact that different modelling approaches will produce somewhat different, yet comparable, results.

C.3 PT Plant: Off-design Performance Metric Validation

Performance metrics from the performance and SAM benchmark models are compared at off-design inputs. The results are displayed in a validation test matrix in Tables C.1 and C.2. For all off-design SM's and TES hours tested, a reasonable agreement between the models is observed. As emphasised in Section 4.2.7, the largest differences occur in the LCOS. Metrics with superscript † are not directly reported as outputs in SAM and are post-processed from SAM simulation results.

Table C.1: Off-design validation test matrix.

TES hours	**Perf. model**			**SAM**			**Rel. err. (%)**		
	SM								
	2	**3**	**4**	**2**	**3**	**4**	**2**	**3**	**4**
CF (%)									
6	38.11	49.48	54.8	39.17	49	53.31	−2.71	0.98	2.79
9	38.79	54.02	61.84	40.1	54.05	61.24	−3.27	−0.06	0.98
12	38.65	57.27	67	39.99	57.7	67.15	−3.35	−0.75	−0.22
UF (%) †									
6	97.96	82.13	68.07	97.98	80.26	65.22	−0.02	2.3	4.4
9	100	89.61	76.69	100	88.41	74.66	0	1.4	2.7
12	100	94.64	82.65	100	94.19	81.5	0	0.5	1.4
Gross-to-net conversion (%)									
6	91.08	92.23	92.16	89.1	89.8	90	2.22	2.71	2.4
9	91	92.13	91.96	89.1	89.7	89.9	2.13	2.71	2.29
12	90.98	92.06	91.88	89.1	89.5	89.7	2.11	2.86	2.43

Table C.2: Continuation of Table C.1.

TES hours	**Perf. model**			**SAM**			**Rel. err. (%)**		
	SM								
	2	**3**	**4**	**2**	**3**	**4**	**2**	**3**	**4**
TES discharge-to-charge ratio (%) †									
6	95.27	96.97	97.39	96.1	97.4	97.7	−0.9	−0.4	−0.3
9	94.48	96.98	97.51	95.2	97.1	97.6	−0.8	−0.1	−0.09
12	93.32	96.9	97.46	94.2	97	97.5	−0.9	−0.1	−0.04
Installed cost per nameplate capacity ($/MWh)									
6	5.35	6.59	7.82	5.35	6.59	7.82	0	0	0
9	6.10	7.33	8.57	6.10	7.33	8.57	0	0	0
12	6.84	8.08	9.32	6.84	8.08	9.32	0	0	0
LCOE (¢/kWh)									
6	11.22	10.35	10.83	11.00	10.48	11.14	2	−1.24	−2.78
9	12.26	10.4	10.42	11.94	10.42	10.53	2.68	−0.19	−1.04
12	13.54	10.67	10.37	13.16	10.61	10.34	2.89	0.57	0.29
Bid price (¢/kWh)									
6	11.83	10.91	11.42	11.59	11.05	11.75	2.07	−1.27	−2.81
9	12.93	10.96	10.99	12.59	10.98	11.10	2.7	−0.18	−0.99
12	14.27	11.25	10.93	13.88	11.18	10.91	2.81	0.63	0.18
LCOS (¢/kWh) †									
6	52.49	28.02	23.04	52.52	28.63	24.64	−0.06	−2.13	−6.49
9	59.1	26.23	20.27	56.34	25.09	19.78	4.9	4.54	2.48
12	71.24	26.89	20.14	66.91	24.76	18.79	6.47	8.6	7.18

C.4 Carnot Battery Performance Model Validation

The high-level annual energy balance is carried out for the benchmark performance model applied as a Carnot battery with a 165 MW heater capacity. RE is charged from solar PV, $T_{\text{set}} = 586$ °C, $t_{\text{TES}} = 4.5$ hours and the SM is that of the benchmark solar field at design.

The resulting Carnot battery's high-level energy balance is shown in Figure C.11. In either mode, it can be seen that the sum of the energy allocations are well within range to the total sources from which the energy is collected (i.e. the two columns are level). Since no augmentations are made to the power cycle or solar field blocks, low-level energy balances are not considered for these. Furthermore, no augmentation has been made to the TES→PC flow channels. Therefore, an additional high-level mass and energy balance analysis of the plant gives results comparable to Figure C.4.

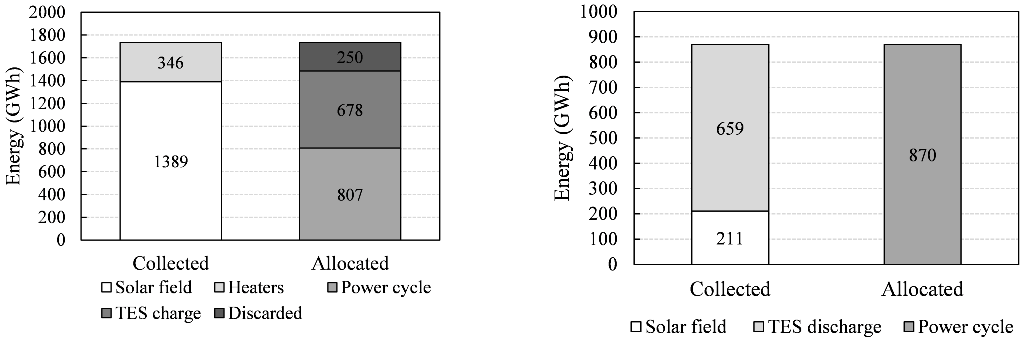

(a) Charge mode.

(b) Discharge mode.

Figure C.11: High-level energy balance validation.

A low-level energy balance for the Carnot battery-applied TES system is considered. Given in Figure C.12, a cumulative TES energy balance error of 1.4 % is present. This remains within range of that found in the performance model without a Carnot battery application, as well as the value found in the SAM benchmark model (Section C.1).

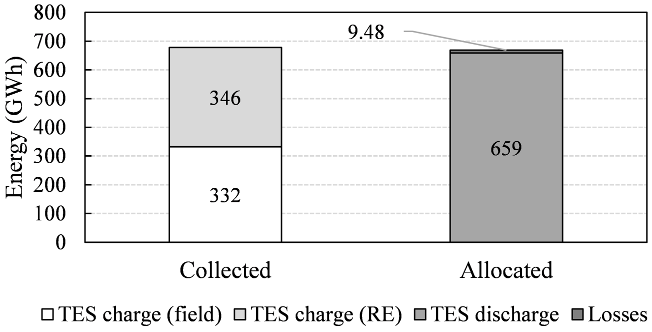

Figure C.12: TES energy balance.

Due to the relatively simple circulation strategy implemented between the TES hot tank and heater block, the TES mass balance confirms a similar result as noted in Figure C.5b. It is concluded that the overall internal validation results for the Carnot battery are deemed satisfactory.

Appendix D

Thermophysical Properties

This appendix provides the thermophysical property relations for the fluids encountered in the thesis. The HTF and HSF are treated as incompressible liquids. Therefore, their fluid property relations are implemented as $f \approx f(T)$.

D.1 Therminol VP-1 (HTF)

Solutia (2020) provides c_p (kJ/kgK) and ρ (kg/m^3) as:

$$c_p(^\circ\text{C}) = 1.498 + 0.002414T + 5.9591 \times 10^{-6}T^2 - 2.9879 \times 10^{-8}T^3 + 4.4172 \times 10^{-11}T^4 \tag{D.1.1}$$

$$\rho(^\circ\text{C}) = 1083.25 - 0.90797T + 0.00078116T^2 - 2.367 \times 10^{-6}T^3 \tag{D.1.2}$$

D.2 Hitec Solar Salt (HSF)

Heller (2013) provides c_p (kJ/kgK), whereas ρ (kg/m^3) is deduced from NREL (2020*b*); Pan (2020):

$$c_p(^\circ\text{C}) = 1.443 + 0.000172T \tag{D.2.1}$$

$$\rho(^\circ\text{C}) = 2090 - 0.636T \tag{D.2.2}$$

D.3 Dry Air

Kröger (1998) provides the following relation for c_p (J/kgK, 101.325 kPa, 220 K to 380 K):

$$c_{p,a}(\text{K}) = 1.045356\times10^{3}-3.161783\times10^{-1}T+7.083814\times10^{-4}T^2-2.705209\times10^{-7}T^3 \tag{D.3.1}$$

Çengel and Boles (2015) provide the following approximation for enthalpy (kJ/kg):

$$h_a(^\circ\text{C}) = 1.005T \tag{D.3.2}$$